University of West Bohemia

Faculty of Mechanical Engineering

DISSERTATION

High temperature mechanical behavior of functionally graded material SS316L/IN718 fabricated by directed energy deposition

Ing. Ying Li **Pilsen, 2024**

FACULTY OF MECHANICAL
ENGINEERING
UNIVERSITY OF WEST BOHEMIA

Dissertation

In support of a candidature for the academic title of PhD
in the study programme

P0715D270027 – Manfacturing and materials

Ing. Ying Li

High temperature mechanical behavior of functionally graded material SS316L/IN718 fabricated by directed energy deposition

Supervisor: Prof. Ing. Jan Džugan, Ph.D.

FAKULTA STROJNÍ
ZÁPADOČESKÉ UNIVERZITY
V PLZNI

SUMMARY OF DISSERTATION WORK

FAKULTY OF MECHANICAL ENGINEERING
UNIVERSITY OF WEST BOHEMIA

Submitted: 2024

Author	*Surname (including of Degrees)* Ing. Li	*Name* Ying
Study Programes	Materials Engineering and Engineering Metallurgy	
Supervisor	Prof. Ing. Džugan, Ph.D.	Jan
Institution / Department	ZČU - FST – KMM	
Title of the Work	High temperature mechanical behavior of functionally graded materials SS316L/IN718 fabricated by directed energy deposition	

Number of pages

Total	126		**Part of Text**	97		**Attachment**	29

Brief Description of the Theme, Findings and Benefits	This research investigates the high-temperature mechanical behavior of FGMs SS316L/IN718 fabricated by LDED, addressing a critical gap in understanding their post-deposition properties. The results show that process parameters, heat treatment and sample orientation significantly influence the mechanical characteristics of both individual materials and the composite FGMs. The study demonstrates that SS316L/IN718 through LDED has considerable promise for high-temperature uses, offering enhanced performance and a broader range of applications.
Key Words	Directed Energy Deposition; Functionally graded materials; IN718; SS316L; Tensile properties; Anisotropy; Heat treatment; Laser power; laser beam; Creep; Microsrtuctrue

FACULTY OF MECHANICAL
ENGINEERING
UNIVERSITY OF WEST BOHEMIA

ANOTACE DISERTAČNÍ PRÁCE

Fakulta strojní Západočeské univerzity v Plzni ak.rok odevzdání: 2024

AUTOR	*Příjmení (včetně titulů)* Ing. Li	*Jméno* Ying
STUDIJNÍ PROGRAM	Materials Engineering and Engineering Metallurgy	
VEDOUCÍ PRÁCE	*Příjmení (včetně titulů)* Prof. Ing. Džugan, Ph.D.	*Jméno* Jan
PRACOVIŠTĚ VEDOUCÍHO	ZČU - FST – KMM	
NÁZEV PRÁCE	Vysokoteplotní mechanické chování funkčně gradovaného materiálu SS316L/IN718 vyrobeného Přímou energetickou depozicí	

Počet stránek (A4 a ekvivalentů A4)

Celkem	126		**Textová část**	97		**Grafická část (přílohy)**	29

STRUČNÝ POPIS ZAMĚŘENÍ, TÉMA, CÍL POZNATKY A PŘÍNOSY	Tento výzkum zkoumá mechanické chování při vysokých teplotách FGM SS316L/IN718 vyrobených pomocí LDED, čímž řeší klíčovou mezeru ve znalostech o jejich vlastnostech po depozici. Výsledky ukazují, že parametry procesu, tepelné zpracování a orientace vzorku významně ovlivňují mechanické vlastnosti jak jednotlivých materiálů, tak kompozitních FGM. Studie demonstruje, že SS316L/IN718 přes LDED má značný potenciál pro použití při vysokých teplotách, nabízí zlepšený výkon a širší rozsah aplikací.
KLÍČOVÁ SLOVA	Přímá energetická depozice; Funkčně gradované materiály; IN718; SS316L; Trakční vlastnosti; Anizotropie; Tepelné zpracování; Výkon laseru; Laserový paprsek; Tečení; Mikrostruktura.

Statement

I declare that I have prepared my dissertation independently and have used the sources I cite and list in the reference list. In the submitted scientific work, the usual scientific procedures are used.

In Pilsen date:........................... ....

Signature

Ackonwlegenment

First and foremost, I am deeply thankful to my supervisor, Prof. Džugan, for affording me the opportunity to undertake this challenging research. His unwavering support, continuous guidance, and invaluable insights have been instrumental in the progression of my PhD journey. My sincere thanks also go to everyone who contributed directly and indirectly to this project.

Special thanks goes to my colleagues: Michal Sádlo, whose assistance with the creep tests was invaluable; Jaromír Dlouhý, Martina Koukolíková, and Pavel Podaný for their expertise in microstructure analysis and their invaluable advice on materials characterization; Jaroslav Vavřík and Michal Brázda for their assistance with sample preparation; and Tomáš Krajňák and Jozef Veselý for their valuable guidance on TEM preparation and analysis. Further appreciation goes to Martin Rund, Václav Brunát, Sylwia Rzepa, Daniel Melzer, and others who made my life abroad more manageable. I wish them all the best in their future pursuits.

My deepest thanks to my dearest friends, Lan-Ying Guo, Zhe-Jing Cai, Maryam Jahanbakhshi, Lin Ma and Li-Ping Liao, for their constant encouragement and understanding throughtout my PhD journey. Their companionship has been a source of strength, helping me navigate the unqiue challenges of doctoral study.

I am forever grateful to my family for their unconditional love, trust, and support. Their unwavering faith in me has always been a beacon, guiding me through challenging times.

Furthermore, I acknowledge my own resilience and determination. Facing and overcoming challenges has made me stronger, and I am pround of the progress I have made. At this point in my journey, I have seen many friends achieve their PhD goals and move on to exciting new chapters; I look forward to the day I join them. It is important to remember that this experience, regardless of positive or negative, is invaluable for the future.

"I dedicate this work to the days and nights I have devoted, to everyone who has been a part of it, and most importantly, to myself ."

Declaration of the project leader

I declare that the project GRAMATECH, within which this dissertation was prepared, has achieved the results presented. The student’s participation in these results comprised 50 % of the project.

Abstract

This dissertation systematically explores the high-temperature mechanical properties of Functionally Graded Materials (FGMs) SS316L/IN718 fabricated through Laser Directed Energy Deposition (LDED). It focuses on post-deposition characteristics and performance under high-temperature conditions, addressing a significant knowledge gap in the field.

The study first analyzes the impact of process parameters on the high-temperature properties of SS316L and IN718. A direct correlation between laser processing conditions and the resultant microstructure was established. Smaller laser beam diameters, coupled with higher laser power, yielded LDED materials with reduced porosity and enhanced high-temperature mechanical properties. The research also identifies sample orientation relative to deposition direction as a key factor in mechanical behavior. Using a larger laser beam with lower laser power tends to promote a uniform microstructure, which diminishes the impact of sample orientation on mechanical properties.

Heat treatment effects on IN718 and SS316L fabricated by LDED were investigated. IN718 demonstrated improved creep resistance, especially after double aging heat treatment. The presence of precipitation phases and irregular columnar grains separated by grain boundary networks can help hinder the dislocation movement during creep, enhancing its high-temperature properties. In contrast, high-temperature behavior of LDED-SS316L is adversely affected by heat treatments above 600 °C, primarily due to dislocation structures and elemental micro-segregations.

Further investigation into LDED manufactured FGMs revealed the significant impact of interface orientation and heat treatment on mechanical properties. Heat treatment promotes elemental diffusion, smoothing the transition at deposition interfaces. The orientation of these interfaces relative to the loading direction critically influences mechanical properties. Interfaces parallel to the loading direction in gradient samples show superior creep resistance, while perpendicular interfaces exhibit behaviors similar to the weaker material, SS316L.

The dissertation concludes by discussing the high-temperature applications of LDED FGMs SS316L/IN718. The findings offer valuable insights for optimizing these materials in demanding environments, providing a roadmap for industry professionals to fully exploit the capabilities of FGMs in diverse applications.

Keywords

Directed Energy Deposition; Functionally graded materials; IN718; SS316L; High temperature mechanical behavior; Anisotropy; Heat treatment; Creep; Laser power; laser beam; Microstructure

Abstrakt

Tato disertační práce systematicky zkoumá vysokoteplotní mechanické vlastnosti funkčně gradovaných materiálů (FGM) SS316L/IN718 vyrobených pomocí laserové přímé energetické depozice (LDED). Zaměřuje se na materiálové vlastnosti po depozici za vysokoteplotních podmínek, čímž řeší významnou mezeru ve znalostech v této oblasti.

Studie nejprve analyzuje vliv procesních parametrů na vysokoteplotní vlastnosti SS316L a IN718. Byla zjištěna přímá korelace mezi podmínkami laserového zpracování a výslednou mikrostrukturou. Menší průměry laserového paprsku společně s vyšším výkonem laseru vedly k materiálům LDED s nižší porozitou a vylepšenými vysokoteplotními mechanickými vlastnostmi. Výzkum také identifikuje orientaci vzorku vzhledem ke směru depozice jako klíčový faktor mechanického chování. Použití většího laserového paprsku s nižším výkonem laseru má tendenci podporovat uniformní mikrostrukturu, která snižuje vliv orientace vzorku na mechanické vlastnosti.

Byly zkoumány účinky tepelného zpracování na IN718 a SS316L vyrobené technologií LDED. IN718 prokázal zlepšenou odolnost proti plížení, zejména po dvojitém stárnutí tepelného zpracování. Přítomnost fází vysrážení a nepravidelných sloupcovitých zrn oddělených sítěmi zrnových hranic může pomoci bránit pohybu dislokací během tečení, čímž se zlepšují jeho vysokoteplotní vlastnosti. Naopak vysokoteplotní chování LDED-SS316L je nepříznivě ovlivněno tepelnými zpracováními nad 600 °C, primárně kvůli strukturám dislokací a elementárním mikrosegregacím.

V případě kombinace těchto materiálů byl odhalen významný vliv orientace materiálového rozhraní a tepelného zpracování na mechanické vlastnosti. Tepelné zpracování podporuje difúzi prvků napříč materiálovým rozhraním dvou kovů a vyhlazuje původně ostrý charakter přechodu. Orientace těchto rozhraní vzhledem ke směru zatížení kriticky ovlivňuje mechanické vlastnosti. Rozhraní rovnoběžná se směrem zatížení u gradientních vzorků vykazují vyšší odolnost proti tečení, zatímco kolmá rozhraní vykazují chování podobné méně odolné SS316L.

V závěru disertační práce jsou diskutovány vysokoteplotní aplikace LDED FGM SS316L/IN718. Zjištění nabízejí cenné poznatky pro optimalizaci těchto materiálů v náročných prostředích a poskytují odborníkům v průmyslu plán, jak plně využít schopnosti FGM v různých aplikacích.

Klíčová slova

Přímá energetická depozice; Funkčně gradované materiály; IN718; SS316L; Vysokoteplotní aplikace; Tečení; Tepelné zpracování

Contents

List of Abbriviation and symbols used

Symbol	Unit	Description
AM		Additive Maunfacturing
FGMs		Fuctionally Graded Materials
LDED		Laser based Directed Energy Deposition
LPBF		Laser based powder Bed Fusion
IN718		Inconel 718
SS316L		Stainless Steel 316L
OM		Optical Microscopy
SEM		Scanning Electron Microscopy
EDSD		Electron Backscatter Diffraction
TEM		Transmission Electron Microscopy
IPF		Inverse Pole Figure
KAM		Kernel Average Misorientation
SAED		Selected Area Electron Diffraction
GROD		Grain Orientaiton Deformation
AD		As Deposited state
SA		Solution treatment + double aging
DA		Double Aging
HSA		Homogenization treatment + Solution treatment + Double aging
OYS	MPa	Offset Yield Strength
UTS	MPa	Ultimate Tensile Strength
UE	%	Uniform Elongation
EL	%	Elongation at Fracture
t_r	h	Creep rupture time
$\dot{\varepsilon}_s$	1/s	Steady creep rate
ε_f	%	Creep strain at fracture
CET		Columnar-equiaxed grain transition
G	K/m	Thermal gradient
R		Grain growth velocity

1 Introduction

Functionally Graded Materials (FGMs) represent a significant breakthrough in material science, offering tailored properties and functionalities that are increasingly in demand in various industrial applications. Characterized by a gradual variation in composition and properties across their volume, FGMs are engineered to meet specific performance requirements, particularly in environments where conventional materials may compromise. This innovation is especially crucial in industries such as aerospace and automotive, where materials are often subjected to extreme conditions, including high temperatures and stresses.

Within the field of advanced manufacturing, the development and fabrication of FGMs have been greatly enhanced by the advent of Additive Manufacturing (AM). AM, commonly known as 3D printing, encompasses a set of technologies that construct objects layer by layer from digital models. This method of manufacturing stands apart for its ability to create complex geometries and custom-designed materials, which were not possible with traditional manufacturing techniques. Its flexibility and precision have opened new approach for designing and producing materials with customized characteristics and performance.

Among the various AM techniques, Directed Energy Deposition (DED) emerges as particularly instrumental in fabricating high-performance FGMs. DED is a process where material, usually in powder or wire form, is fed into a melt pool created by a focused energy source like a laser or electron beam. This method allows for precise control over material deposition, enabling the creation of components with gradient compositions, such as the FGMs comprising SS316L (a stainless steel alloy) and IN718 (a nickel-based superalloy). The ability to fabricate these materials through DED has sparked considerable interest due to their potential for superior performance in high-temperature environments.

Despite the advancements in FGMs and their fabrication through AM and DED, there remain significant challenges and knowledge gaps, particularly concerning the high-temperature behavior and optimal fabrication processes of FGMs like SS316L/IN718. The lack of comprehensive data on the high-temperature mechanical properties of these materials is a notable obstacle, limiting their broader application in industry. Additionally, most existing research has concentrated on the properties of these FGMs in their as-deposited state, leaving questions about their long-term performance and suitability for specific applications.

Furthermore, the exploration of anisotropic mechanical properties, a characteristic inherent to AM materials, has been limited in the context of FGMs. This gap is particularly pronounced in studies focusing on DED-produced materials, which often overlook the impact of anisotropy on the overall functionality and performance of FGMs.

This dissertation aims to address these gaps by employing a comprehensive approach. The initial phase will focus on understanding the high-temperature behavior of the individual materials, IN718 and SS316L, under various processing conditions and heat treatments. The subsequent phase will leverage this knowledge to fabricate a FGM SS316L/IN718 component using DED, optimized for high-temperature applications. This research will extend beyond the traditional constraints of anisotropic behavior in AM materials, considering a wider range of sample orientations to provide a comprehensive understanding of the mechanical properties and potential of FGMs.

Through this methodical approach, the study intends to not only bridge the existing knowledge gaps but also to pioneer the successful production of high-quality FGM components suitable for high-temperature environments. This research aims to expand the current boundaries of material science and engineering, unlocking the full potential of FGMs fabricated through DED in demanding industrial applications.

2 Analysis of the current state of knowledge

2.1 Functionally graded materials (FGMs)

FGMs are advanced engineering materials designed to offer spatially varying properties within a single component. This concept is illustrated in Figure 2-1. This attribute is achieved through gradual transitions in composition, structure, or function across the material, enabling specific local properties unattainable with homogeneous materials. FGMs originated in Japan during the 1980s as a part of a space-plane project, aimed at creating thermal barrier materials capable of withstanding significant temperature gradients [1]. Since then, their applications have expanded significantly, including industries such as aerospace, biomedical, automotive, and energy [2, 3].

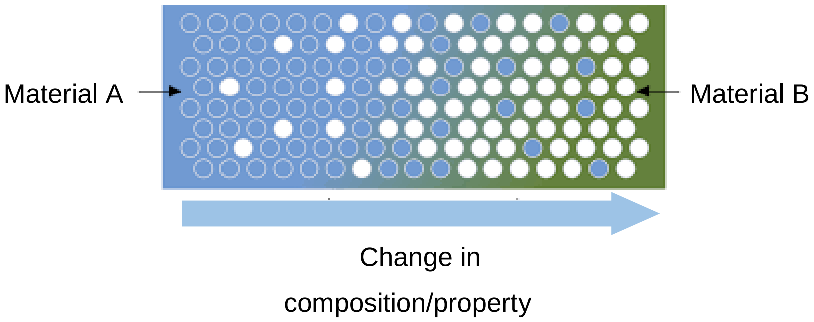

Figure 2-1 Concept of Functionally graded materials.

In aerospace, FGMs are used in turbine blades and rocket nozzle linings to withstand extreme temperature gradients and mechanical stresses [4]. In the biomedical sector, FGMs are revolutionizing implant technology, offering enhanced biocompatibility and improved bonding with bone tissue [5]. In the automotive industry, FGMs contribute to the development of brake rotors and engine components with improved wear resistance and heat dissipation properties [6]. In the energy sector, FGMs are utilized in nuclear reactors for enhanced radiation shielding and in solar panels for optimal thermal management [7]. These diverse applications underline the adaptability and utility of FGMs, highlighting their potential to meet specialized industrial needs and open new avenues in material science and engineering. Figure 2-2 shows practical examples in engineering applications where gradient structures from FGMs are essential.

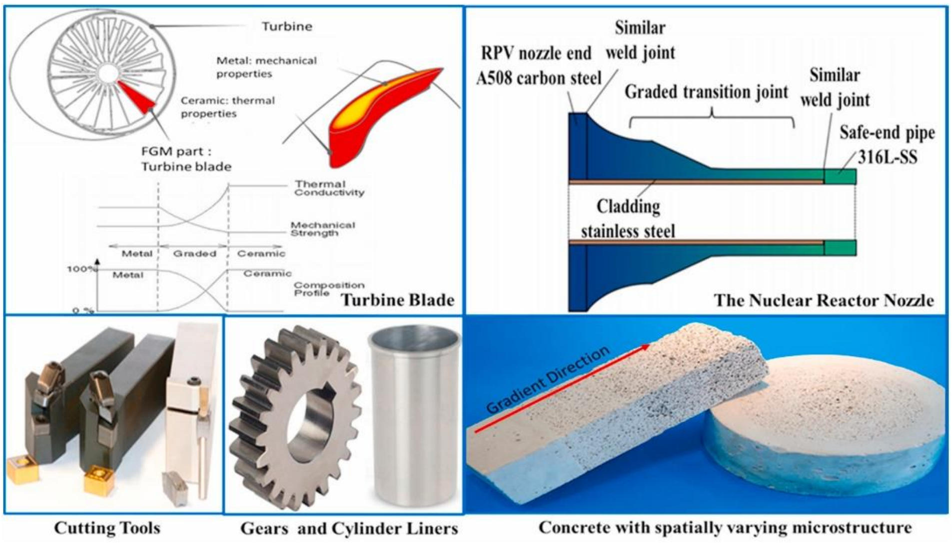

Figure 2-2 Some examples of FGMs requring structues with graded properties [8].

The classification of FGMs can be approached from multiple perspectives, reflecting their diverse nature [9]. Based on the type of gradient, FGMs can be categorized into two primary types: continuous and discrete. Continuous FGMs feature a smooth and gradual transition in properties and composition, often achieved through a progressive change in material composition or structure. This gradual transition is crucial in applications requiring a seamless variation in properties. In contrast, discrete FGMs consist of distinct layers, each with a sharp change in properties at the interface, making them suitable for applications that benefit from clear demarcations between different material characteristics.

Additionally, FGMs are classified based on their material systems, including metal-metal, ceramic-ceramic, metal-ceramic, and polymer-based systems. Metal-metal FGMs are utilized for their unique combinations of mechanical properties, while ceramic-ceramic FGMs are favored for their thermal and wear resistance, particularly in high-temperature environments. Metal-ceramic FGMs offer a blend of the toughness of metals with the high-temperature resilience of ceramics, making them ideal for challenging aerospace and automotive applications. Lastly, polymer-based FGMs are emerging as a versatile choice in biomedical applications due to their adaptability and biocompatibility.

Various fabrication methods are employed to create FGMs, each with its advantages and challenges [10]. Traditional methods include powder metallurgy, layer-wise slurry deposition, and centrifugal casting. The advent of AM technologies, especially DED and Powder Bed Fusion (PBF), has introduced new dimensions in FGM fabrication. These AM techniques enable controlled, layer-by-layer material deposition, allowing for complex geometries and precise placement of different materials.

Recent developments in FGMs have been propelled by advancements in AM technologies and computational modeling. These innovations facilitate the fabrication of FGMs with complex geometries and meticulously tailored property gradients, further broadening the scope of their applications.

2.2 Laser directed energy deposition (LDED)

AM represents a transformative approach in modern manufacturing, constructing components in a layer-by-layer fashion, which affords exceptional design versatility and efficient material application [11, 12]. Within the AM spectrum, DED is distinguished by its dynamic processing capabilities and versatility [13, 14]. DED utilizes a concentrated energy source — such as a laser, electron beam, or plasma arc — to fuse material, fed in powder or wire form, directly onto a substrate, building parts sequentially, layer by layer. Unique advantages of DED, when contrasted with other AM techniques like PBF, include processing an expansive array of materials — even those with high-strength and high-temperature resistance — and constructing larger parts with minimal material waste. Unrestricted by a powder bed, DED can fabricate on substrates of various dimensions, enhancing its utility in repair and maintenance operations.

Among those approaches for the fabrication of FGMs, AM, particularly the DED technique, exhibits unique potential for FGM components. DED offer several advantages such as the ease of introducing different powders into the melt pool, unlimited design freedom, and cost-effectiveness for complex 3D parts. This technique is essentially a solid freeform fabrication process and has garnered substantial attention for its capability in producing near net-shaped components, surface coatings, part repairs, and, notably, functionally graded materials [13, 14].

The DED process involves focusing a high-energy laser beam onto a substrate or a pre-deposited layer, creating a melt pool. Metal powders are then concurrently introduced into this melt pool via a specialized coaxial nozzle. As the laser beam moves in synchronization with a computer numerical controlled (CNC) table, a 3D component emerges layer by layer, faithfully translating computer-aided design (CAD) files into physical forms without the need for costly tooling. A typical DED machine encompasses a deposition head, energy source, material delivery nozzle, and a motion control system. The configuration often includes multi-axial movement capabilities, enabling the creation of intricate geometries within a single manufacturing cycle. A typical laser-based directed energy deposited process (LDED) is illustrated in Figure 2-3. One distinct advantage of LDED is the rapid cooling rate, resulting in a unique non-equilibrium microstructure that yields fine-grained materials with mechanical properties superior to those fabricated by conventional means. This fusion of design flexibility and unique microstructural benefits has derived the adoption of LDED in crafting commercial alloys for sectors including biomedical, automotive, and aerospace [17, 18]. Noteworthy materials processed via this method encompass stainless steel [16, 19, 20], nickel-based alloys [21–23], and the prominent Ti6Al4V [15, 24].

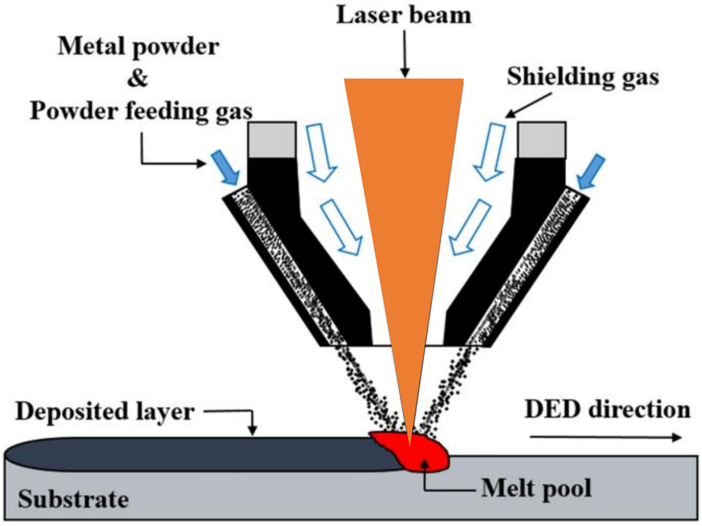

Figure 2-3 Diagram of laser power direct energy deposition [25].

Tracing its roots back to the growing stages of AM, DED has undergone considerable evolution, achieving greater precision, enhanced deposition rates, and superior material characteristics. Contemporary DED machines incorporate advanced monitoring and control systems, ensuring improved surface finishes and mechanical properties of the manufactured items [26]. Current advancements in DED technology are marked by strides towards greater automation, real-time quality monitoring, and the adoption of artificial intelligence to refine the manufacturing process [27, 28]. These developments not only highlight the maturation of DED as a critical AM technique but also its expanding significance in contemporary manufacturing frameworks, ranging from rapid prototyping to comprehensive production solutions.

2.3 Current state of FGMs SS316L/IN718 via LDED

Among numerous metallic systems in LDED-FGMs, gradients from iron-based to nickel-based alloys, such as FGMs SS316L/IN718, have garnered significant attention. This interest is due to their promising high-temperature mechanical properties, compatibility, and potential for applications that demand high strength, creep, and corrosion resistance, such as nuclear power generation and oil refineries [29–33].

2.3.1 Stainless steel 316L (SS316L)

Stainless Steel 316L (SS316L) is a low-carbon, austenitic stainless steel alloy notable for its balanced composition. It contains substantial chromium (16-18%), nickel (10-14%), and molybdenum (2-3%), alongside minor quantities of manganese, silicon, phosphorus, sulfur, and nitrogen. The combination of these elements gives SS316L with a face-centered cubic structure stabilized by nickel, maintaining the austenitic phase and providing excellent mechanical properties. Its reduced carbon content minimizes the risk of carbide precipitation, enhancing its weldability and resistance to intergranular corrosion. Mechanically, SS316L offers an optimal balance of strength and ductility, which can be further enhanced through cold working. The alloy's toughness is notable, even in cryogenic conditions, and it stands out from other stainless steels by its exceptional corrosion resistance. SS316L's versatility is evidenced by its widespread use in marine environments, chemical processing, food production, and medical implants, due to its reliability and resistance to a wide range of corrosive environments.

2.3.2 Inconel 718 (IN718)

Inconel 718 (IN718) is a nickel-chromium superalloy that stands out for its high strength and excellent corrosion resistance, particularly in extreme environments. The alloy's composition is predominantly nickel (50-55%), with significant contributions from chromium (17-21%) and supplemented by elements such as niobium, tantalum, molybdenum, titanium, and aluminum. The strength of IN718 stems from its mix of precipitation hardening and solid solution strengthening. Its distinct properties come from the phases present in it. Various phases commonly observed in IN718 alloy can be summarized in Table 2-1. To simplify, matrix: γ (gamma) phase has a face-centered cubic austenitic structure; Primary strengthening phase: γ'' phase, composed of Ni_3Nb, increases yield strength and hardness due to its resistance to dislocation movement; Strengthening Phase: γ' phase, primarily made of Ni_3 (Al, Ti), further aids strength. Additionally, minor phases, such as δ-phase (delta phase), manifest during long exposures to intermediate temperatures (650 °C to 1000 °C) and impact toughness. Laves phase, an often undesired brittle phase, can appear during solidification or prolonged temperature exposure. Carbides and carbonatites, mainly of MC type structures, form from reactions with elements like Ti and Nb. They assist in strengthening grain boundaries and controlling grain growth. The diverse applications of IN718 alloy range from aircraft engine components to space vehicles, underlining its adaptability to high-stress, high-temperature scenarios. However, the alloy must be carefully processed and heat-treated to achieve its peak mechanical properties and capitalize on the beneficial effects of its various strengthening phases.

Table 2-1 Phases commonly observed in IN718

Phase	**Classification**	**Crystal structure**	**Chemical formula**	**Appearance**
γ	Matrix	disordered FCC	Ni	Background
γ'	GCP	FCC (ordered $L1_2$)	$Ni_3(Al,Ti)$	cubes, round cubes, spheres, or platelets
γ''	GCP	BCT (ordered $D0_{22}$)	Ni_3Nb	very small disks
δ	TCP	Orthorhombic (ordered $D0_a$)	Ni_3Nb	acicular (needle-like), plate-like
MC	Carbide	Cubic (B_1)	(Nb,Ti) C	string-like clumps, string of pearls
Laves	TCP	Hexagonal (C_{14})	$(Ni,Fe,Cr)_2$ (Nb,Mo,Ti)	coarse widmanstatten platelets

The selection of the SS316L/IN718 combination for FGMs is justified by their similar structural and thermophysical properties, which allow for a seamless gradient in an FGM context. The alloys' compatibility is further evidenced by their ability to form good metallurgical bonds and maintain crack-free interfaces, crucial for the structural integrity of FGMs. IN718 can effectively serve as a transition layer to other materials like copper [34] and TiAlV [35], expanding the functional range of SS316L-based FGMs. The union of SS316L and IN718 in an FGM configuration is particularly well-suited to environments requiring high-temperature strength and corrosion resistance. Ultimately, the choice to focus on SS316L/IN718 within this study is informed by the need to explore their synergistic potential further and to optimize heat treatment processes to fully harness their combined properties for advanced FGM applications.

2.3.3 State of art of FGMs SS316L/IN718

Despite the solid compatibility of SS316L and IN718, the structural integrity and mechanical properties of the resultant materials still strongly depend on process parameters and the building strategy, including the laser power and sequence of materials deposition [36]. Due to the diversity of FGMs, advancements in LDED-FGMs SS316L/IN718 will be reviewed based on interface type: a gradual or an abrupt transition. Significant advancements have been made in comprehending the influence of process parameters and building strategies on the microstructure and mechanical properties of LDED-FGMs with an abrupt interface.

Melzer et al. [30] and Dzugan et al. [37] studied the mechanical response upon directly depositing IN718 on top of SS316L (type I-interface) and vice versa (type II-interface). Subsequent studies by Koukolikova et al. [38] and Halmešová et al. [39] investigated the effect of laser power on both interfacial characteristics and thermal properties of these interfaces, respectively. Light micrograph observation of type I and II interfaces are depicted in Figure 2-4. Results suggest that the type I interface is more favourable due to superior mechanical properties and fewer defects. A straight fusion line with successful crack-free deposition was formed in the type I interface regardless of the different laser power or consistent process parameters applied on the new-deposited top layers. The type II interface, on the other hand, revealed a higher mixture and within several melt pools and a wider transition zone with increased laser power and thermal conductivity. However, this led to an increase in solidification cracks and defects [38, 40, 41], most cracks disrupted the structural integrity and consequently, the mechanical properties of FGMs, but these could be alleviated with optimized process parameters. The favourable fabrication sequence of SS316L on the IN718 or IN625 was also reported when alternating deposition sequence of SS316L and IN625/IN718 [42, 43] at the consistent laser power regardless to the materials type being deposited.

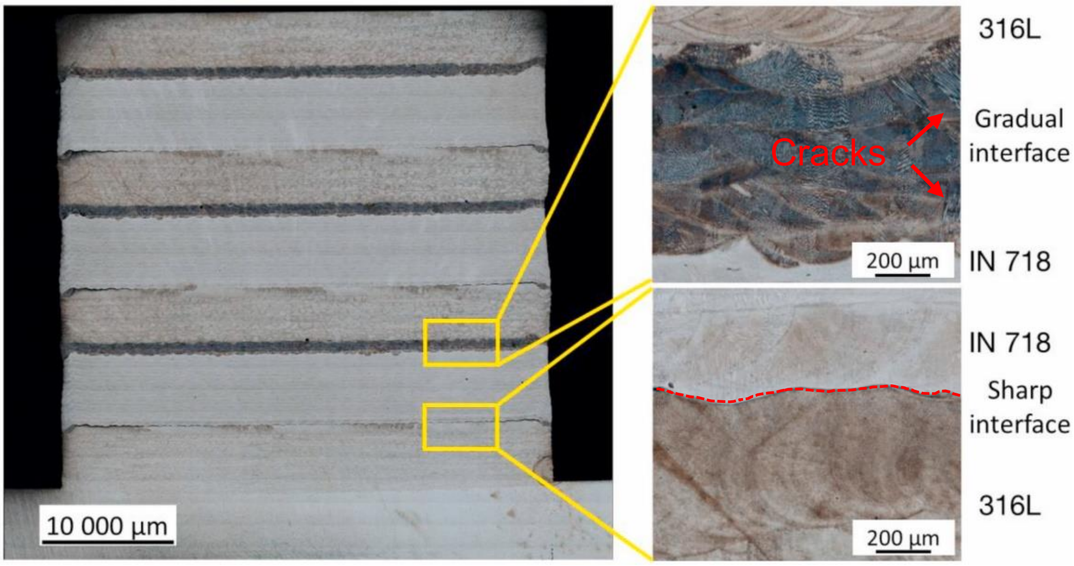

Figure 2-4 Light microscopy observation of the type I and II interfaces [30].

In addition to direct interfaces, researchers have devoted significant efforts to exploring the gradual interface of FGMs SS316L/IN718, aiming to minimize thermal stress caused by the combination of two dissimilar materials. This interface type, due to the gradual change in chemical composition, presents intriguing diffusion behaviour. Shal et al.[29] examined the influence of process parameters (laser power and powder flow rate) on the gradual fabrication of a SS316L to IN718 using LDED. The results shows an absence of cracks induced by thermal stress, regardless of the parameters used. Su et al. [44] studied the impact of gradation steps (5%, 10%, and 20%) in laser additive manufacturing FGMs SS316L/IN718 on microstructure and mechanical properties. They found that a 10% chemical increment yield the best tensile properties, with a tensile strength of 527 MPa and 26.21% elongation. Ghanavati et al. [45] analysed solidification behaviour by varying the graduation step (0%, 20%, 50%) in the laser additive manufactured of thin-walled SS316L/IN718 graded materials. They successfully fabricated FGMs of various chemical composition without visible cracks. However, Kim et al. [41] observed critical defects in regions of 30 wt% IN718/70 wt% SS316L and 20 wt% IN718/80 wt% SS316L during the fabrication of FGMs via LDED with a chemical gradient step of 10%. The formation of defects was induced by the presence of ceramic oxides Al_2O_3 generated via oxidation during the high-energy laser irradiation process. The defective compositional regions at which the hot cracking was likely to occur were deliberately and strategically exclude while the rest of the graded compositional range and structural integrity was retained. The selective discrete compositional range processing of IN718 and SS316L demonstrate a successful approach for the AM-FGMs to join dissimilar materials and improve the final mechanical performance.

Most existing microstructural and mechanical studies on FGMs SS316L/IN718 with direct and gradual interfaces have been conducted in as-deposited conditions. As previous research [46, 47] revealed that precipitation processes are hampered by high cooling rates in AM, post-processing heat treatments are crucial for enhancing the mechanical properties of LDED FGMs [48–50]. This is due to that IN718 does not readily form the strengthening precipitates γ'/γ'' during LDED process [46]. Thus, to this end, some efforts has been conducted to evaluate the impact of heat treatment on microstructural gradients, precipitation transformations, and mechanical properties in FGMs. Li et al. [33] and Ji et al. [51] examined the evolution of element composition, aging precipitation behaviors, microstructure and hardness upon heat treatment by using the experimental-computational analysis. Their results clearly indicate that homogenization heat treatment smooth the each gradient region and the hardness measurement at both each gradient region and the interfaces. The following aging precipitation process significantly improves the hardness of FGMs near the IN718 due to the dissolution of Laves phase and the precipitation of primary phases γ'/γ''. Lu et al. [52] and Wen et al. [53], using LDED and LPBF techniques respectively, reported an improvement in tensile properties of FGMs SS316L/IN718 by application of heat treatment. In addition to mechanical enhancements, Xu et al. [54] reported improved corrosion behaviour as a result of heat treatment. It effectively enhances overall hot corrosion resistance by promoting finer grains and granular Laves phases, which provide additional diffusion channels for Cr and Ni, leading to the formation of a mixed oxide layer of Cr_2O_3 and NiO.

Previous research typically focuses on FGMs SS316L/IN718 components deposited in the Z-building direction with a horizontal interface perpendicular to the build direction. However, complex geometries can demand deviations from this ideal horizontal plane. The most critical locations are typically corner zones where interface orientation abruptly shifts from horizontal to vertical orientation. In response, the impact of varying interface orientations (15°, 30°, 45°, 60° and 90°) and surface treatment was examined on the structural integrity and mechanical properties of FGMs SS316L-IN718 [55, 56]. Results revealed that the interface orientation has significant influence on the amount and distribution of formed defects at the interfaces, and the surface treatment significantly reduced the amount of solidification cracks at the interfaces. This research offers valuable guidance for both the production of functionally graded materials production and component repair scenarios.

The extensive research has significantly contributed to the advancement of FGMs SS316L/IN718 through LDED. However, despite the critical importance for high-temperature applications, there is a lack of data on high temperature mechanical properties. Furthermore, existing studies on these FGMs predominately focus on the as-deposited state, which might not satisfy the final mechanical property requirements for specific applications. Additionally, though anisotropic mechanical properties are a typical characteristic of AM materials, information about them in FGMs is scarce. Previous investigations into the mechanical properties of LDED FGMs have primarily examined samples with a single orientation, where the interface is perpendicular to the building direction.

2.4 High tempertaure properties of AM deposited SS316L and IN718

2.4.1 Introduction to high temperature mechanical behavior

The mechanical integrity of materials at elevated temperatures is a cornerstone of engineering applications where components are exposed to thermal stress. For advanced manufacturing techniques, particularly AM, understanding how materials like SS316L and IN718 behave under such conditions is of great importance. While tensile properties provide a snapshot of material strength and ductility, creep — the time-dependent deformation under constant stress — becomes a dominant factor in long-term service reliability.

Materials produced via AM techniques exhibit unique microstructures that differ significantly from those of their traditionally manufactured counterparts [17, 19, 24]. These differences can lead to distinct responses under thermal and mechanical loading. For instance, the fine grain structures often observed in AM materials can enhance mechanical properties at room temperature but may respond differently when subjected to high-temperature conditions.

Despite the growing use of AM in producing components for high-performance applications, there is a notable knowledge gap regarding the high-temperature mechanical properties of AM materials. This gap is particularly evident for AM-produced SS316L and IN718, which are widely used in industries where high-temperature performance is critical, such as aerospace and power generation. The literature reveals that while some properties, such as yield strength and fatigue behavior, are well-characterized at room temperature, their high-temperature behavior, especially creep, is less understood.

This lack of comprehensive understanding hinders the full exploitation of AM's potential in high-temperature applications. Therefore, studying the high-temperature mechanical properties of AM SS316L and IN718, especially those fabricated using LDED, is essential. Exploring the combination of these materials within a single FGM component promises to exploit their respective strengths — the excellent corrosion resistance of SS316L and the exceptional creep resistance of IN718 — thereby creating components that can reliably withstand the rigorous demands of high-temperature environments.

2.4.2 Theory of creep

Creep, the progressive deformation of a material under constant stress over time, is a critical consideration for components designed for high-temperature applications. The rate of creep is not only a function of the applied stress and temperature but is also profoundly influenced by the microstructure of materials. The creep behavior of metals and alloys can generally be categorized into three distinct stages: primary, secondary, and tertiary creep, with each stage dominated by different microstructural mechanisms [57].

For IN718 and SS316L, the microstructural features such as grain boundaries, precipitate phases, and dislocation density play significant roles in their creep response. The creep behavior of IN718 is highly reliant on its precipitate phases, such as γ'' (Ni_3Nb) and γ' ($Ni_3(Al, Ti)$), which provide the alloy with high-temperature strength through precipitation hardening. These precipitates act as obstacles to dislocation motion, thus enhancing the creep resistance. However, at elevated temperatures, these precipitates can dissolve or coarsen, leading to a decrease in creep resistance over time. In SS316L, the creep mechanism is primarily influenced by the movement of dislocations within the austenitic grain structure. Grain size can significantly influence creep resistance; finer grains can offer better creep strength at lower temperatures due to grain boundary hardening, but at high temperatures, larger grains may be more beneficial due to the lower boundary area reducing the rate of grain boundary sliding.

The alloying elements in both SS316L and IN718 also contribute to their high-temperature performance. In SS316L, elements like chromium and molybdenum promote the formation of passive films that protect against high-temperature oxidation, thereby maintaining the material's integrity under thermal exposure. For IN718, the presence of niobium, in combination with nickel, forms the γ" phase, which is crucial for high-temperature strength. Meanwhile, aluminum and titanium contribute to the formation of the γ' phase, further enhancing the creep resistance.

Understanding these microstructural factors is critical for predicting the performance of SS316L and IN718 when subjected to the high temperatures and stresses characteristic of service conditions in aerospace and energy applications. This theoretical foundation provides the basis for exploring how the unique microstructures developed through AM processes, and particularly LDED, influence the high-temperature tensile and creep properties of these materials.

2.4.3 Creep behavior of AM-IN718

As of this writing, no data on the high-temperature mechanical properties of FGMs SS316L/IN718 are available. There exist limited reports detailing the high-temperature mechanical characteristics, specifically creep properties, of individual materials like AM-SS316L and AM-IN718.

Table 2-2 provides a comprehensive review of existing studies on the creep performance of AM-IN718, emphasizing the parameters investigated and their principal findings [58, 59, 68, 69, 60–67]. From the data, main findings can be concluded:

- Creep behavior is predominantly documented for LPBF IN718.
- Parameters such as heat treatment and sample build orientation have been primarily investigated in the context of creep performance of AM-IN718, comparing them to conventionally produced counterparts.
- Recent studies have also explored the influence of scanning strategies and surface integrity on creep properties [70, 71].
- The findings suggest that, despite LPBF IN718 exhibiting tensile properties similar or even superior to traditionally manufactured counterparts, its creep behavior is often found inferior under tensile creep conditions [58, 60–65, 67, 68].

Table 2-2 Summary of the available literature for creep performance of AM-IN718 materials

Process	Parameters studied	Creep conditions	Main findings	Ref.
L-PBF	Heat treatment	650 °C/650 MPa	Creep life: hot rolled (200 h) > HSA (90 h) >AD (55 h) >HIP (20 h) Fracture strain: Hot rolled (0.2) > HIP (0.13) > As-built (0.1) > HIP (0.05)	[68]
	PBF-AP vs cast and forged	650 °C/600 N small punch	Creep life: forged (2.29 h) > PBF-AP (1.28 h) > cast (1.18 h)	[60]
	Heat treatment and build orientation	650 °C/400 N small punch	Creep life: HA-X (705.64 h) > HSA-X (363.84 h) > SA-X (305.71 h) > HA-Z (104.51 h) > HSA-Z (48.33 h) > SA-Z (32.10 h)	[72]
	Heat treatment and build orientation	650 °C/550 MPa	Creep life: C&W (>1000 h) > HIP + DA (677 h) > DA (600h) >STA (1180 °C/1h/462h) > AD (270h) > STA (980 °C/1h/135h).	[59, 65]
	Surface integrity and heat treatment	650 °C/750 MPa	Creep life: Wrought (150 h) > HTMix (48.27 h) > ABMix (12 h) >HTCNC (6.4 h) +ABCNC (6.73h)	[61]
	Heat treatment and build orientation	Compressive creep 630 °C/900-1100 MPa	Creep rate: SHT 1000 < DA < SHT 930 < C&W	[66]
	Scan strategy and build orientation	650 °C/600 MPa	Creep life: 90° Multi (416 ± 19 h) > Wrought (409 ± 8 h) > 90° Single (320 ± 4 h) > 45° Multi (189 ± 8 h) > 45° single(188 ± 5 h) > 0° Single (131 ± 16 h) Elongation at fracture: Wrought (29.3 ± 0.1 %)> 90° Multi (7.0 ± 0.4 %) > 90° single (6.9 ± 0.3 %)	[71]
	Scan strategy and build orientation	650 °C/600 MPa	Creep life: 90° Meander HT (507 ± 13 h) > Wrought (409 ± 8 h) > 90° Stripe HT (320 ± 4 h) > 45° Stripe HT (188 ± 5 h) > 0° Stripe HT (131 ± 16 h) Elongation at fracture: Wrought (29.3 ± 0.1 %)> 90° Meander HT (7.5 ± 0.5 %) > 90° Stripe HT (6.9 ± 0.3 %)	[73]
	N/A	700 °C/560 MPa	Creep life: Forged (64 h) > SLM-as built (24 h)	[74]
L-DED	Heat treatment and build orientation	650 °C/750 MPa	Creep life: L-DED DA-YX (67 ± 11 h) > wrought (38 ± 3 h) > DA-Z (26 ± 12 h) Elongation at fracture: L-DED DA-YX (3.3 ± 1.9 %) > wrought (2.8 ± 0.7 %) > DA-Z (2.9 ± 1.6 h)	[46, 75]

Heat treatment is a determinant factor in the creep performance of AM-IN718. Studies have consistently shown that AM materials typically display creep properties that are less favorable when compared to those produced by traditional manufacturing methods [58, 60–65, 67, 68]. This discrepancy is often attributed to the finer grain structure of AM components, which results from the rapid cooling rates inherent to the process. Since the weakening of grain boundaries is a predominant mechanism of failure during high-temperature creep, a microstructure with a higher volume of grain boundaries can escalate the likelihood and initiation of cracks, thereby degrading creep resistance. Consequently, AM-produced metals with a coarser grain structure are considered advantageous for enhanced creep performance, attributable to a reduced frequency of grain boundaries and associated damage sites.

In addition to grain size, the presence of δ-phase precipitates and the formation of subgrain boundaries, due to a high density of dislocations, are also known to adversely affect the creep strength [65]. Contrasting this trend, IN718 parts manufactured by LPBF and subjected to subsequent heat treatment exhibit superior creep behavior relative to their conventionally cast and wrought counterparts [66]. This enhancement is linked to an increased volume of finely distributed γ'' and γ' precipitates and the development of fine subgrains measuring 0.5-0.65 μm within the AM microstructure. Such precipitates act to inhibit the formation of the δ phase, which otherwise impairs creep properties.

Sample orientation in the AM process has also been shown to impact creep behavior, presenting a complex pattern of anisotropy [58, 62, 64–67, 72]. To date, research has not reached a consent on the anisotropic creep behavior of AM metals, characterized typically by less favorable creep life and ductility in specimens oriented horizontally and perpendicular to the build direction, as opposed to vertically aligned specimens that are parallel to the build direction. Various hypotheses have been proposed to explain these disparities, ranging from the arrangement of interdendritic δ phase [65], variations in Young's modulus and material texture [67], to grain size discrepancies [76], and the presence or absence of carbides and Σ3 type boundaries [64]. Additionally, reports suggest that applying higher temperatures during solution heat treatment can mitigate both microstructural and creep anisotropy by diminishing texture and refining columnar grain structures in LPBF variants [64].

Conversely, other studies indicate a markedly higher creep resistance in specimens oriented along the scanning direction compared to those along the building direction, as determined by small punch creep tests [72] and nanoindentation techniques [69]. Despite these variations, some research shows no significant anisotropic effect [66], with samples in both orientations demonstrating superior creep strength relative to cast and wrought materials.

These disparate findings on high-temperature creep behavior are likely tied to the unique microstructures formed by the diverse AM techniques, processing parameters, and post-processing conditions employed across studies. Besides heat treatment and sample orientation, other factors that have been observed to impact the creep properties of AM samples include the heterogeneity of microstructures developed during AM [59, 66, 72, 77], specific process parameters such as hatch spacing, beam velocity, layer thickness, and powder quality [76], as well as process-induced defects like porosity and surface irregularities [61, 78].

The existing research offers a wealth of information regarding the influence of microstructure on the creep performance of AM-IN718, yet these studies predominantly examine materials produced via the LPBF technique. The rapid scanning speeds of LPBF result in significantly higher cooling rates, leading to the development of a refined microstructure characterized by finer grains and a high density of dislocation subgrain boundaries. This finer granularity is often cited as a contributing factor to the observed inferior creep properties when benchmarked against conventionally manufactured materials.

In contrast, LDED typically achieves a coarser microstructure due to relatively lower cooling rates. This distinction in grain structure suggests that LDED-IN718 may exhibit creep properties that differ markedly from those of LPBF-produced materials. The coarser grain features inherent to LDED are theorized to potentially enhance creep resistance. Consequently, there is a compelling rationale to further explore the creep behavior and fracture mechanisms of LDED-IN718, particularly in comparison with its conventionally manufactured counterparts, to ascertain whether this coarser microstructural characteristic indeed translates into improved high-temperature performance.

2.4.4 Creep behavior of AM-SS316L

Regarding the AM-SS316L, its high-temperature properties have also gained notable attention due to the excellent resistence to corroison at elevated temperature.

Table 2-3 provides a comprehensive review of existing studies on the creep performance of AM-SS316L, emphasizing the parameters investigated and their primay findings [74-85]. The collective research on the creep behavior of AM-SS316L offers valuable insights, particularly in the areas of build orientation, process parameters, heat treatment effects, and comparisons with conventionally manufactured materials.

Table 2-3 Summary of the available literature for creep performance of AM-SS316L materials

Process	Parameters studied	Creep conditions	Main findings	Ref.
LPBF	Sample orientation	650 °C/149-226 MPa	The vertical direction specimen showed better creep resistance.	[79]
	Scanning speed	650 °C/ (320-550N) SP test	A scanning speed range of 416 to 572 mm/s is recommended to increase creep resistence.	[80]
	Process parameter (laser power, scanning speed, and energy density)	650 °C/ (270-550N) SP test	The vertical specimen demonstrated a longer creep life and higher creep resis- tance than the horizontal specimen.	[81]
	Sample orientation	650 °C and 700 °C SP test	Vertical sample exhibit longer rupture time compred to hirozontal specimen due to the large grain size, larger grain boudaru areas and faster diffusion rate.	[82]
	Sample orientation	650 °C/270-550N	Creep life and the creep resistance of the vertical specimen were significantly higher than those of the horizontal specimen.	[83]
	N/A	550-650 °C/175-300 MPa	additively-manufactured 316 L stainless steel had a higher stress dependence of the minimum creep rate than conventionally-made type 316 SS.	[84]
	Heat treatment	550 °C/275 MPa	Creep behavior is strongly affected by heat treatment.	[85]
	N/A	650 °C and 700 °C/ 175-275 MPa	The creep stress exponents of the LPBF material are smaller than that of the conventional variant.	[86]
	Process parameter (laser power, scanning speed, and energy density)	650 °C/ (320-550N) SP test	Creep behavior is closely linked to the process parameters, such as scanning speed and laser power.	[87]
	Sample orientaton	650 °C/97-150 MPa uniaxial and multiaxial creep tests	Horizontal specimen exhibits 8 times faster minimum creep rates than vertical sample and significantly shorter rupture lives.	[88]
LDED	Heat treatment	650 °C/225 MPa	Heat treatment tempertaure over 600 °C result in a significant decrease in creep resistance.	[89]
	Process parameter and sample orientation	650 °C/225 MPa	Creep behavior is closely linked to the process parameters, such as scanning speed and laser power. Horizontal sample show a better creep resitance than vertical sample.	[90]

Studies [79, 81, 83, 88] have consistently shown that the sample build orientation in LPBF significantly influences creep resistance. Vertically oriented specimens in these studies demonstrated enhanced performance, a phenomenon attributed to the alignment of grain structures. This anisotropic behavior was further echoed in the findings of Williams et al. [88], who noted faster creep rates and shorter rupture lives in horizontally oriented samples compared to vertically oriented ones in LPBF-manufactured SS316L.

Focusing on the intricacies of LPBF processing parameters, investigations revealed a delicate balance between scanning speed and laser power. Yu et al. [87] noted a balance between productivity and creep resistance within specific scanning speed ranges, while Dao et al. [83] observed that increased laser power could mitigate the negative effects of higher scanning speeds, enhancing overall creep resistance. Comparative analyses with conventional counterparts, undertaken by Hermanová et al. [82] and Calderón et al. [86], revealed that LPBF SS316L shares similar mechanical properties but with some reductions in ductility and greater creep damage. Li et al. [84], in their LPBF study, observed a higher stress dependence on the minimum creep rate in additively manufactured steel, attributed to differences in dislocation cell structures.

The role of heat treatment in modifying creep behavior was explored in depth in both LPBF [85] and LDED [89] studies. These studies found that different heat treatment temperatures significantly impact the microstructure and, consequently, the creep resistance of SS316L. Particularly in LDED-manufactured SS316L, varying heat treatment temperatures altered the microstructure, affecting creep resistance and emphasizing the importance of chemical micro-segregation in stabilizing dislocation cell structures. Among various microstructural characteristics, the dislocation cell substructure inherent in AM materials has been a focal point of research due to its unique combination of strength and ductility, which sets it apart from conventionally-processed SS316L [19, 91, 92]. As discussed in the study by Li et al. [85], LPBF SS316L samples annealed between 650-1050 °C revealed that as the dislocation cell size increased or the cell wall thinned, the creep rates correspondingly rose. The correlation between dislocation cell structure and creep rate can be seen in Figure 2-5.

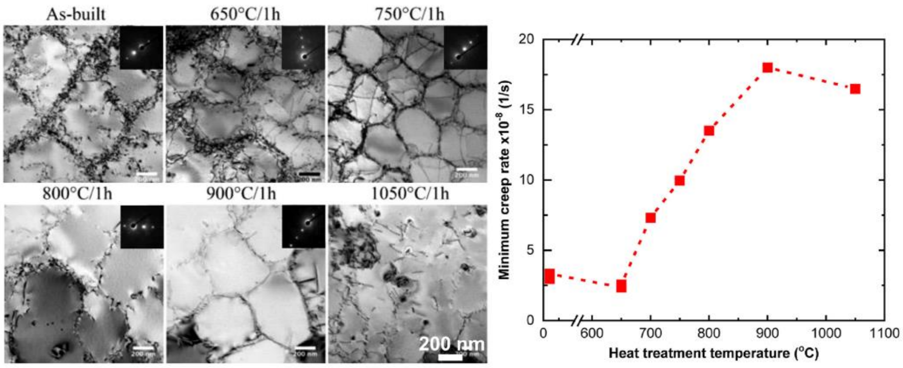

(a) (b)

Figure 2-5 Correlation of dislocation cell structure evolution with creep property for LPBF-SS316L [85].

While there is a comprehensive understanding of the mechanical properties at room temperature of AM-SS316L, considering factors like crystallography, dislocations, precipitates, and chemical micro-segregations [93, 94], the high-temperature performance of AM-SS316L remains a research frontier, especially for samples produced via the LDED method. Notably, the cooling rate in LDED is markedly lower than in LPBF processes, suggesting that it might influence the dislocation cell structure differently and, by extension, the material's mechanical properties at elevated temperatures. Furthermore, given the mechanical demands of precipitation-strengthened IN718, post-processing heat treatments have been identified as vital, especially for LDED-produced FGMs SS316L/IN718 [48–50]. Such treatments could introduce potential challenges, like thermal instability, which might adversely affect the mechanical properties of AM-SS316L. Therefore, exploring the heat treatment's effects on the microstructure and subsequent high-temperature creep properties of AM-SS316L emerges as a key research avenue.

For a compresensive understanding of the FGMs SS316L-IN718 via LDED, it becomes essential to explore the high-temperature behavior of LDED-IN718 and LDED-SS316L. Recognizing the gaps in current research, there is a pressing need to conduct comprehensive studies on LDED-IN718 and LDED-SS316L. Such endeavors would not only provide insights into the standalone properties of LDED-individual materials but also offer critical context for optimizing and comprehending the performance characteristics of FGM SS316L-IN718 under high-temperature scenarios.

2.4.5 Synergistic Considerations for FGMs

The creation of FGMs that synergistically blend SS316L and IN718 presents a unique opportunity to engineer components with optimized high-temperature mechanical behavior, especially in terms of creep resistance. The design of such FGMs necessitates a thorough understanding of how the intrinsic properties of each material contribute to the overall performance of the gradient structure under thermal stress.

For FGMs, the transition from the corrosion-resistant SS316L to the creep-resistant IN718 can be tailored to exploit the favorable attributes of each alloy. The challenge lies in achieving a gradient that maintains the structural integrity of SS316L while leveraging the superior high-temperature creep properties of IN718. Given that the microstructure significantly influences creep behavior, the design process involves strategic planning around the AM process parameters and also the heat treatment to control grain size and the distribution of precipitates across the gradient.

Studies have highlighted that the fine grains prevalent in LPBF-processed IN718 may lead to reduced creep resistance, whereas the coarser grains typically formed in LDED processes are believed to enhance it. In the context of FGMs, this suggests that LDED could be a more suitable AM technique for producing gradients with improved high-temperature properties. By carefully controlling the thermal gradients and cooling rates during the LDED process and the post-processing heat treatment, it may be possible to engineer a gradient that not only bridges the material properties of SS316L and IN718 but also induces a favorable microstructure for high-temperature applications.

Furthermore, the relationship between the AM-induced microstructure and the resulting mechanical properties requires careful consideration. The orientation of the gradient in relation to the build direction, the potential anisotropy in mechanical properties, and the presence of defects must be meticulously evaluated to ensure that the FGM can withstand the demands of high-temperature environments. This includes understanding the role of heat treatment in homogenizing the microstructure and reducing anisotropy, which could be crucial for the performance of FGM components.

In summary, the design of FGMs that incorporate SS316L and IN718 must take into account the distinct creep behaviors and high-temperature tensile properties of both materials. The objective is to harness the high-temperature resilience of IN718 and the reliable performance of SS316L to fabricate FGMs that meet the rigorous demands of industries operating at elevated temperatures. The insights from AM research on individual materials provide a foundation for developing FGMs with superior and predictable performance, driving advancements in materials engineering for high-temperature applicpations.

3 Objectives of the dissertation

The primary objective of this dissertation is to advance the understanding of the high-temperature mechanical properties and to develop a high-quality functionally graded component comprised of SS316L/IN718 through LDED. The following specific objectives have been set to guide this research endeavor:

- Perform a detailed investigation into how LDED process parameters affect the microstructure and high-temperature mechanical properties of IN718 and SS316L. This will enable the determination of optimal deposition conditions that yield the best material performance. (Chapter 4)
- Assess the impact of various heat treatment protocols on the microstructure evolution and high-temperature mechanical properties of IN718 and SS316L. The goal is to identify the most beneficial post-processing treatments for each material, which will also contribute valuable information for the creation of their combined FGM. (Chapter 5 and 6)
- Utilize the insights acquired from the analysis of individual material's characteristics to refine the LDED fabrication process for FGMs, concentrating specifically on corroborating their mechanical performance at elevated temperatures following heat treatment. This will involve a rigorous assessment of their resilience under thermal stress, a critical attribute for their deployment in real-world applications. (Chapter 7)
- Examine the anisotropic mechanical properties that are characteristic of AM-fabricated materials by evaluating FGMs across different sample orientations. This objective aims to broaden the understanding of anisotropy in FGMs, moving beyond the scope of traditional material studies. (Chapter 7)
- Develop practical guidelines for the manufacturing and deployment of FGMs SS316L/IN718 in environments that experience high temperatures. The intention is to bridge current research gaps and promote wider adoption in industrial sectors where high-temperature performance is crucial. (Chapter 8)

By achieving these objectives, this dissertation will contribute significantly to the field of materials science, particularly in the area of AM and FGMs, and could potentially pave the way for innovative applications in demanding high-temperature settings.

4 Effect of process parameter on SS316L fabricated by LDED

4.1 Introduction

The impact of process parameters on the microstructure and high-temperature mechanical properties was investigated in their as-deposited states. This chapter aims to offer insights into the relationship between process parameters, microstructure, and mechanical attributes of the materials fabricated, and determine the optimal process parameters for FGMs parts. Early trials showed that LDED process parameters have similar effects on both IN718 and SS316L. Therefore, this chapter will focus on SS316L to illustrate the impact of process parameters on materials fabricated by LDED, providing a focused analysis that is broadly applicable.

4.2 Materials and methods

4.2.1 LDED fabrication

Commercial SS316L powder, with a particle size ranging from 45 to 150 μm (Sandvik, United Kingdom), was used. The chemical composition of the SS316L powder used is shown in Table 4-1. A powder-blown DED apparatus with a laser energy resource (LDED, InssTek MX-600, Daejeon, South Korea) was utilized to fabricate various SS316L parts [30, 95]. It is noteworthy that this LDED machine was also employed in the fabrication of individual IN718 and their FGMs. As illustrated in Figure 4-1, the LDED setup comprises a 2 kW Ytterbium fibre laser with selectable spot sizes of 0.8 mm and 1.6 mm, a 3-axis laser coaxial nozzle, a 2-axis numerically-controlled working table, and a multi-hopper powder feeder system (with a maximum of 6 hoppers). Direct metal tooling (DMT) technology, a subset of DED techniques, was incorporated. This approach utilizes two vision cameras to analyze and regulate the melt pool height in real-time, ensuring consistent layer thickness throughout the deposition process. Within the laser's co-axial nozzle, both the powder and a gas stream are concurrently fed. The feeding mechanism is gravity-driven, regulated by gas pressure and facilitated by a spinning wheel. To combat oxidation, argon gas was dual-purposed as both the shielding and powder carrier gas.

Table 4-1 Nominal chemical composition (in wt. %) of the 316L SS powder used to manufacture the specimens

Element	C	Mn	P	S	Si	Cr	Mo	Ni	Al	Fe
SS316L	0.016	1.27	0.024	0.012	0.75	17.03	2.4	10.89	0.003	Bal.

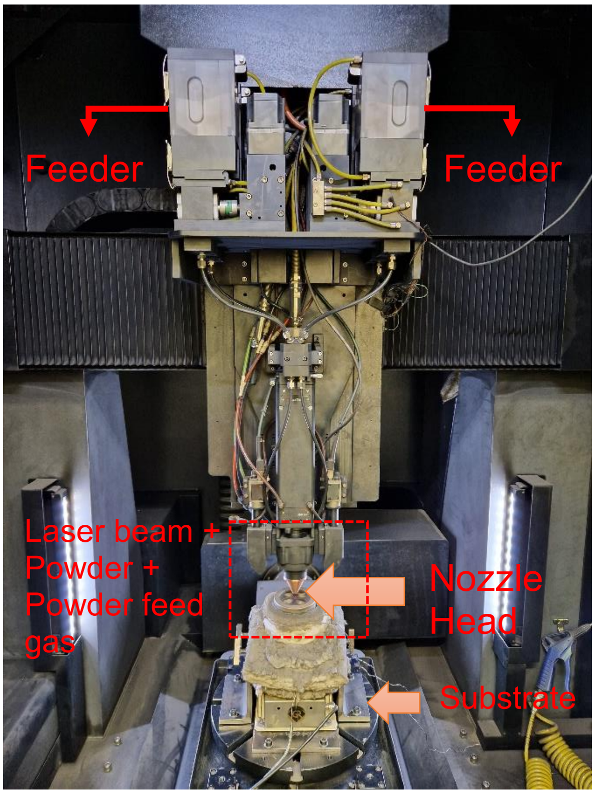

Figure 4-1 InssTek MX-600 powder metallic deposition system.

Two different modules, SDM800 and SDM1600, were chosen within the DMT mode to produce SS316L parts, as shown in Figure 4-2(a). Specifically, the numbers 800 and 1600 indicate the diameters (in micrometers) of the laser beam utilized in the LDED process. To maintain constant energy density, the SDM1600 deposition process, which uses a larger beam diameter, compensated with higher laser power, hatch distance, layer thickness, and powder feed rate compared to the SDM800 process. The optimal process parameters for each module, developed by the manufactures, are listed in Table 4-2. To produce parts of identical dimensions, the deposition time for the SDM800 process, as simulated by the built-in software, is 7.67 hours. In contrast, for the SDM1600 process, it is significantly reduced to 1.7 hours. This implies that employing a larger beam diameter with optimized process parameters can substantially enhance the build rate by 78%, while concurrently reducing the amount of powder consumed per print by 58%. Consequently, this leads to a 132% increase in the efficiency of powder consumed per print. A zigzag scanning strategy with a 90° rotation between successive layers was adopted to produce parts with dimensions of 36 x 36 x 36 mm^3 on annealed SS316L substrates of 100 × 100 × 20 mm^3 [96]. Note that this scanning strategy was also applied in the deposition processes for other materials, including IN718 and FGMs.

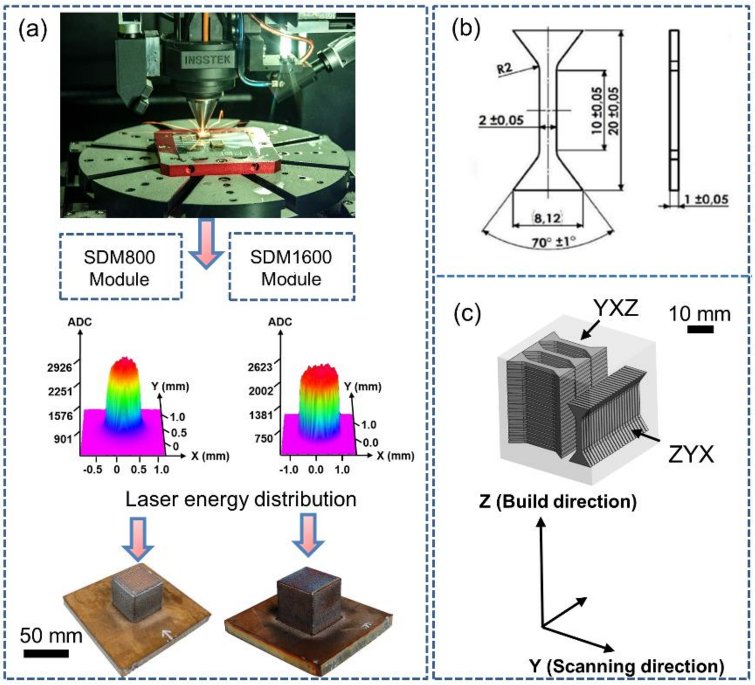

Figure 4-2 Schematic of LDED fabrication process under various process parameters.

Table 4-2 Process parameters utilized to deposit SS316L blocks

Module	**SS316L (SDM800)**	**SS316L (SDM1600)**
Energy area density [J/mm^2][52]	44	42
Laser power [W]	450-550	900-1000
Scanning speed [mm/min]	849	849
Laser beam diameter [mm]	0.8	1.6
Hatch distance [mm]	0.5	1.1
Layer thickness [mm]	0.25	0.6
Powder feed rate [g/min]	2.66	5.6
Scanning strategy	ZigZag CFC+CF	

4.2.2 Mechanical testing

To evaluate mechanical properties, especially elevated temperature mechanical properties, tensile test at room temperature and elevated temperature, creep testing will be carried out to reveal the correlations of various conditions and the mechanical behavior of LDED materials.

4.2.2.1 Tensile properties at ambient and elevated temperature

Tensile and creep specimens, shaped as flat dog-bones, were precisely machined using electro-discharge machining for each investigated condition. The specimen geometry for both tensile and creep tests are delineated in Figure 4-2(b). To examine the potential anisotropy in microstructure and mechanical behaviors of LDED material, two orientations were devised: the ZYX sample was oriented such that its building direction aligned with the loading axis, whereas the building direction of YZX specimen was set perpendicular to this axis, as detailed in Figure 4-2(c). Adhering to ISO/ASTM 52909, the specimens were labeled, emphasizing the orientation and location-dependent mechanical properties typical for metal additive manufacturing.

Tensile properties at both ambient and elevated temperatures, A ZWICK/ROELL-Z250 electromechanical tester equipped with a 25 KN load cell was chosen for this purpose. The setup for elevate temperature tensile testing system including a furnace, grips and contactless video extensometer can be seen in Figure 4-3. The testing is performed in accordance with ASTM E8/E8M [97] and E21 [98]. For ambient conditions, strain rates of 0.00025 s^{-1} (pre-yield point) and 0.0067 s^{-1} (post-yield until failure) were employed. For the elevated temperature tests, these rates were 0.00007 s^{-1} and 0.0014 s^{-1}, respectively. The deformation of the specimen was record using a contactless video extensometer based on DIC with a single camera mounted to the testing machine's frame. Prior to testing, the specimens were uniformly coated with a contrasting black and white pattern, ensuring optimal contrast during both ambient and high-temperature tests. For room-temperature characterization, a 4 MPix camera acted as the extensometer, capturing the elongation of specimen. For high-temperature scenarios, a more advanced 12 MPix camera from the ZwickRoell suite was chosen. Throughout the testing, images were captured at a consistent frame rate of 1 Hz, facilitating a subsequent, in-depth strain field analysis on the MTT specimens via the Aramis GOM Correlate software. The analysis utilized facets and step sizes of 20 and 15 pixels, respectively, to determine the strain distribution over the sample during tensile loading.

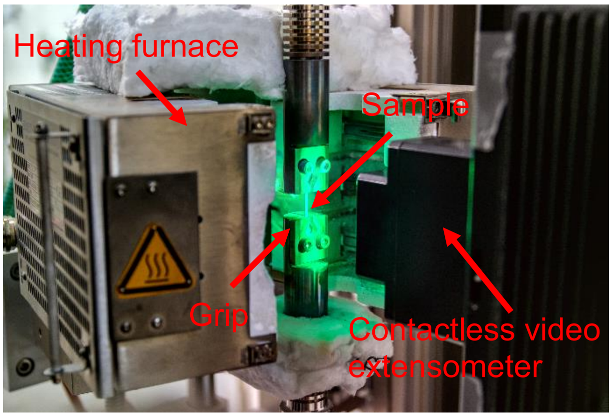

Figure 4-3 Elevated temperature Zwick/ROELL-Z250 electromechanical testing machine including the furnace, grip and contactless video extensometer.

4.2.2.2 Creep testing

Tensile creep tests for all investigated conditions were performed at 650 °C. The stress level chosen for creep testing balanced the considerations of test duration and material properties. Specifically, the optimal stress was selected to ensure that creep testing was both time-efficient and below the material's yield strength, minimizing the impact of non-creep induced plastic deformation [61, 68]. Based on the tensile results, the optimal stress for creep tests was set 225 MPa for LDED-SS316L. These tests were executed using a lever-arm creep machine, boasting a 30 KN load capacity, as illustrated in Figure 4-4. Throughout the tests, creep strain was diligently captured using an HBM WA/20 mm displacement transducer, carefully positioned on the centerline of rod connected to the specimen. A three-zone furnace, complemented by two Pt-Rh/Pt thermocouples attached to the test specimen's upper and lower gauge lengths, ensured the specimen's temperature remained consistent within ± 2 K. Once the 650 °C target temperature was attained, specimens were stabilized at this temperature for an hour before commencing the tests. For each condition, three to four specimens were assessed to guarantee consistency and reproducibility of the results.

Figure 4-4 Stand lever arm creep machine.

4.2.3 Materials characterization

LDED specimen at various heat-treated states were subjected to microstructure and fractography analysis. Samples preparation methods for microstructure characterization consist of mechanical grinding, polishing and ultra-polishing with op-s colloidal silica, as shown in Figure 4-5(a). To reveal the columnar-dendritic microstructure produced by LDED, the polished sample were etched for a few seconds using a Glyceregia etchant (15 ml HCl, 10 ml glycerol and 5 ml HNO_3).

Various microscopy methods were used to characterize the microstructure and fracture mechanism after mechanical testing. Optical microscopy (OM; Nikon Eclipse MA200, Tokyo, Japan), shown in Figure 4-5(b) was used in the present study to revel the overview of microstructural characterization of sample at lower magnification, such as melt pool, porosity and solidification cracks. Phase, texture, and grain orientation information was revealed using scanning electron microscopy (SEM; JEOL IT 500 HR, JEOL Ltd., Tokyo, Japan), as shown in Figure 4-5(c). SEM is also fitted with an energy-dispersive spectroscopy system (EDAX, Octane Elite Super, EDAX LLC, Mahwah, NJ, USA) and an electron backscatter diffraction system (EBSD; EDAX Hikari Super camera, EDAX LLC, Mahwah, NJ, USA). Acquisition of EBSD data was done at an accelerating voltage of 20 KV and a step size of 3 µm. All EBSD maps are defined such that the <001> is aligned with the build direction. The collected diffraction patterns were indexed by spherical indexing using the TEAM 4.5 software package and Hough indexing within OIM Analysis™ v8 software. Detailed microstructure and dislocation analysis were carried out using a JOEL JEM-2100 transmission electron microscope (TEM) equipped with EDAX energy-dispersive X-ray spectroscopy (EDS) detector.

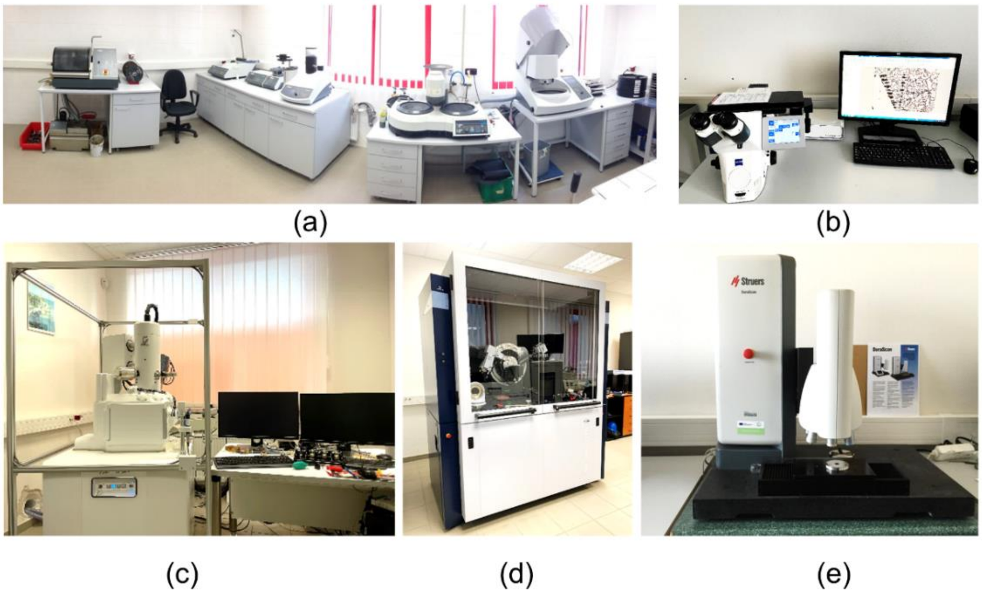

Figure 4-5 (a) Standard metallography preparation-Struers, Tegramin grinder, etc, (b) Nikon MA200 optical microscopy with NIS elements software, (c) JEOL IT 500 HR equipped with EBSD and EDX scanning electron microscopy, (d) Bruker D8 Discover X-Ray diffraction and (e) Vickers hardness tester with load of 0.1-10 Kg.

For TEM analysis, thin foils were prepared, first by thinning down mechanically to a thickness of about 0.1 mm, and then five small disks with a diameter of 3 mm were prepared from the thin foils by using electro-discharging machining. These disks were then electro-polished using a dual-jet polishing system, Struers TENUPOL-5 operated at − 30 °C and 15 V in an electrolyte solution of 83% methanol and 17% perchloric acid. To qualitatively evaluate the phase and porosity of samples at various conditions, min10 micrographs with the area of 18 x 18 mm^2 were taken from each disk and the area fraction (%) and size of phase and pores were determined by using NIS elements AR version 5.02 analysis software.

To identify the phase constituent at various conditions, X-ray diffraction (XRD) analysis was performed on polished surfaces of samples on Bruker D8 Discover diffractometer (Bruker AXS GmbH, Karlsruhe, Germany) with a copper anode (λ Kα1 = 0.15406 nm) at 40 kV and 40 mA in Bragg-Brentano geometry. The increment was set to 0.025° in the range of 2ɵ from 30° to 100°, as shown in Figure 4-5(d). The density was measured by the gravimetric method, according to Archimedes principle.

Hardness profiles HV/10 (load 10 kg) were measured using a laboratory hardness tester, the Struers DuraScan 50 (EMCO-TEST Prüfmaschinen GmbH, Kuchl, Austria), equipped with ecos WorkflowTM software (EMCO-TEST Prüfmaschinen GmbH, Kuchl, Austria). The struers hardness tester is shown in Figure 4-5(e). The hardness measurement was carried out in accordance with ISO 6507-11: Vickers hardness measurement.

4.3 Results

4.3.1 Microstructure

Figure 4-6 shows the XRD analysis results of all LDED specimens. The face-centred cubic austenite phase (γ) was detected in all as-built specimens. In addition to the primary γ phase, each specimen also exhibited the presence of body-centred cubic (BCC) ferrite phase (δ). The weak peaks around 44.46°, near the strongest peak of the γ phase in all specimen, indicate the existence of a minor amount of δ ferrite phases. The results are consistent with previous studies on LDED microstructure [99–103], but differ from some reports of a monophase γ austenite phase in specimens [104–106]. The various process parameters used in those studies of LDED result in different heating and cooling rates, which is believed to contribute to the unique solidification process and hence, the solidification microstructure in those studies.

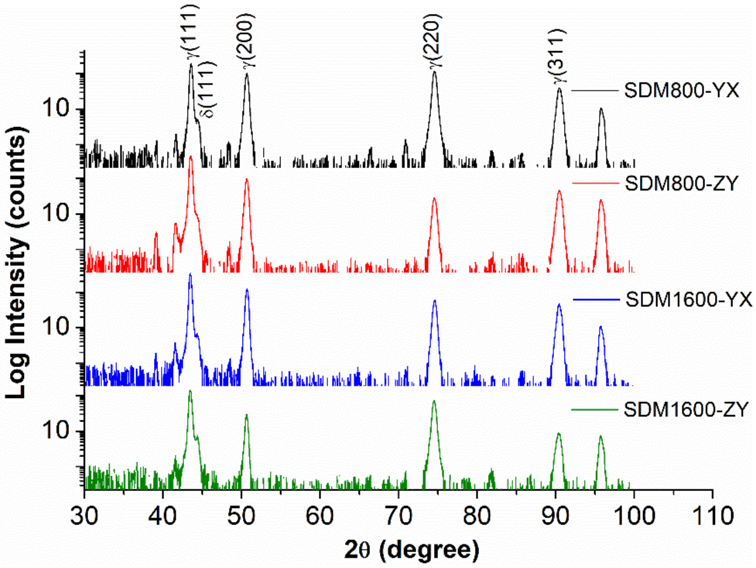

Figure 4-6 XRD patterns of the as-deposited LDED-SS316L samples.

Figure 4-7 presents optical micrographs of the XY- and ZY cross-sections of SDM800 and SDM1600 samples, revealing clear differences in porosity, melt pools and grain structure.

Table 4-3 summarizes the porosity and melt pool dimensions. An increase in laser beam size from 800 to 1600 μm leads to porosity rising from 0.001% to 0.2% in the XY-cross section and from 0.01% to 0.2% in the ZY-cross section, indicating lower porosity with smaller laser beam sizes. Despite these differences, both printing modules achieve near-full densities above 99.8%. In addition, another typical solidification microstructure of LDED, overlapping melt pools within distinct grain structures, is visible in the samples. The 'fish scale' pattern of melt pools, typical in the LDED microstructure [38, 99, 101, 107], suggests radial heat extraction and grain growth. This pattern is evident in Figure 4-7(b) and (e), leading to a diverse grain orientation distribution (Figure 4-7c and f). The SDM1600 samples show larger melt pools, with average widths (*w*) increasing from 800 μm to 1200 μm and depths (*h*) from 375 μm to 700 μm compared to SDM800. The finer, columnar grains in SDM800, aligned along the heat flow as indicated by arrows in Figure 4-7(c), contrast with the more random, coarse columnar and equiaxed grain mixture illustrated in Figure 4-7(f).

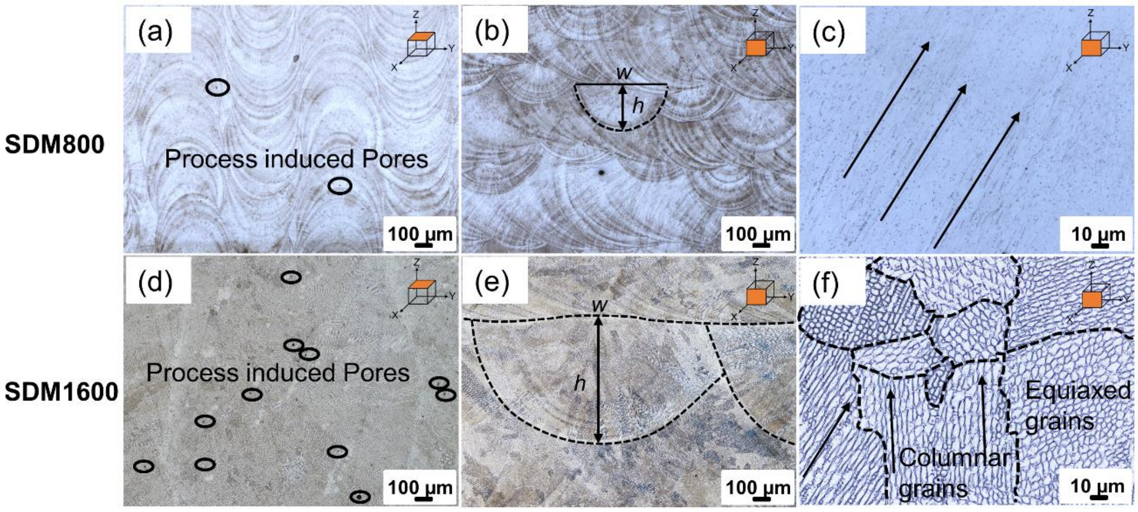

Figure 4-7 Optical micrographs of SDM800 (a-c) and SDM1600 (d-f) samples showing differences in porosity (a, d), melt pool dimensions (b, e) and grain structures (c, f), respectively.

Table 4-3 Statistics of porosity, average grain diameter, secondary delta phase, and Taylor factor for various LDED samples.

	SDM800-XY	**SDM800-ZY**	**SDM1600-XY**	**SDM1600-ZY**
Porosity/%	0.00	0.01	0.20	0.20
Dxy /μm	41 ± 34	48 ± 39	162 ± 125	279 ± 223
Delta phase/%	1.20 ± 0.38	1.22 ± 0.42	3.05 ± 0.94	3.45 ± 1.07
Taylor factor	3.08	3.1	3.01	2.91

SEM analysis highlights a transition from columnar to equiaxed grains near the fusion boundaries in the as-built samples, as shown in Figure 4-8. This transition is attributed to variations in temperature gradient and cooling rate along the maximum heat flow direction within melt pools. High temperature gradients and cooling rates near melt pool boundaries favor columnar-dendritic grain formation, while lower gradients and rates result in equiaxed grains near the melt pool cores. Compared to LPBF, LDED exhibits more pronounced columnar-equiaxed transitions due to a lower thermal gradient (G) to grain growth velocity (R) ratio, resulting in a higher fraction of equiaxed grains, whereas LPBF typically produces finer columnar dendrites due to high dilution effects [108]. Additionally, in both SDM800 and SDM1600 samples, a cellular sub-grain microstructure is observed in Figure 4-8(b) and (e), with SDM800 (~ 2.9 μm) having slightly smaller cells than SDM1600 (~ 3.2 μm), indicating a lower cooling rate in SDM1600.

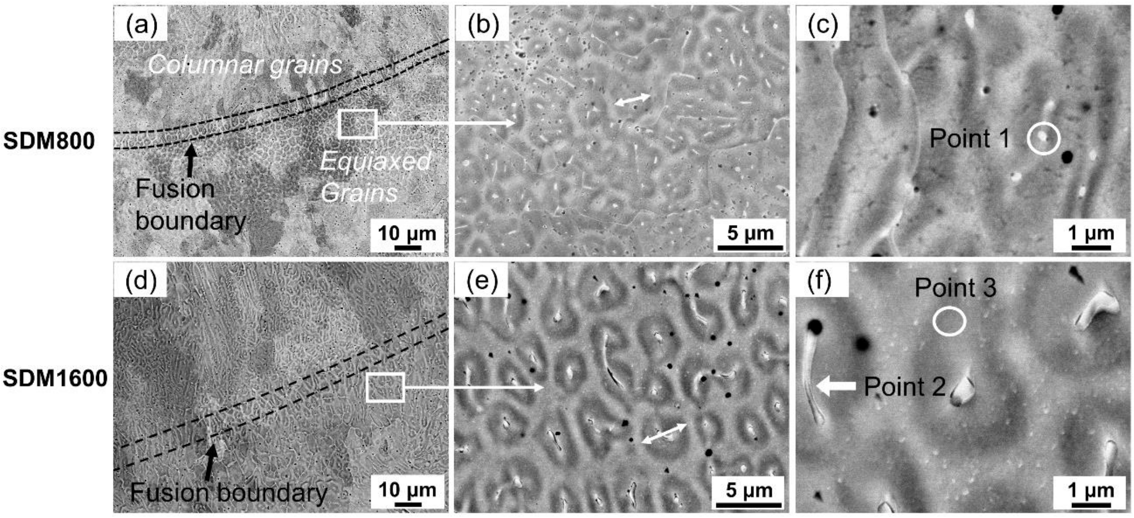

Figure 4-8 SEM micrographs of the ZY-cross section of as-built SDM800 sample (a-c) and SDM1600 sample (d-f).

Furthermore, white particles, visible in the microstructures in Figure 4-8(b) and (e), are positioned within the austenitic dendrite matrix and along grain boundaries. Those particles were identified as delta ferrite through a combination of XRD and EDS analyses, as detailed in Table 4-4. This identification is further supported by the consistency of these features with the morphology described in the literature [99–103]. As discussed in previous study [109], the formation of delta phase in LDED was linked to the Cr_{eq}/Ni_{eq} ratio, with a higher ratio favouring ferrite formation. In the present study, the Cr_{eq}/Ni_{eq} ratio is 1.56, falling within this range (1.38-1.60) where austenite forms primarily, followed by ferrite at grain boundaries due to segregation [100–102]. In addition, the SDM1600 sample exhibits more delta phase than SDM800 sample, as evidenced by the data in Table 4-4 and illustrated in Figure 4-8(c) and (f). According to Guo et al., [102], a higher cooling rate tends to result in a fully austenitic microstructure by inhibiting solute redistribution. Consequently, the comparatively slower cooling rate experienced by the SDM1600 sample promotes the formation of a more substantial amount of delta phase.

Table 4-4 EDS results of possible phases in the SDM800 and SDM1600 DED sample (wt. %).

Point	Phase	Cr	Ni	Mo	Si	Al	Mn	Fe
1	Spherical	19.6	5.8	2.7	1	0.4	1.3	62.1
2	Long rod	19	6.2	2.5	1.1	0.5	1.2	62.7
3	Matrix	17.6	7.4	1.6	0.8	0.1	1.3	62.7

Figure 4-9 presents EBSD orientation maps for SDM800 and SDM1600 samples, highlighting differences in grain size, shape and distribution across ZY- and XY-cross sections. Grain size measurements from EBSD analysis are summarized in Table 4-3. The XY-plane of the SDM800 sample exhibits the smallest average grain diameter, while the ZY-plane of the SDM1600 sample has the largest grains. Notably, the large error in the measurement of grain diameter reflects the heterogeneous microstructure typical of DED under these process parameters. Moreover, within the melt pool outlined in Figure 4-9(a), columnar grains grow perpendicular to the melt pool boundaries along the maximum heat flow direction. Far from the melt pool boundaries, columnar grains transform into equiaxed grains, which are observed in the core of the melt pool. This transformation is more pronounced in the melt pools of single track in LDED process [107]. To estimate the texture, the distribution of the Taylor factor is computed on the ZY- and XY-cross sections for both cases, based on the raw EBSD data. The Taylor factor accounts for averaging the grain orientations over all grains in the sample and thus can be used to evaluate the texture in the sample. Regardless of cross sections or printing conditions, the value of the Taylor factor is approximately 3, indicating a random texture and no overall significant preferred lattice orientation in the as-built SS316L sample. The orientation of columnar cells is determined by the solidification direction, which varies according to localized temperature gradient, melt flow, and solidification rate within the melt pool [11, 13].

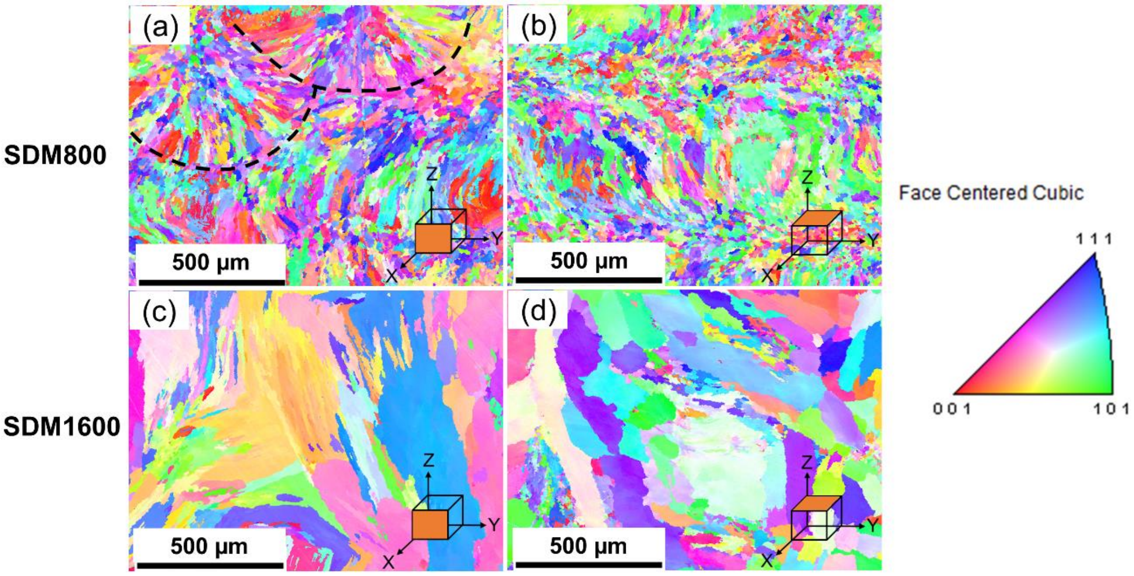

Figure 4-9 EBSD-IPF for SDM800 (a-b) and SDM1600 (c-d) samples.

4.3.2 Tensile properties at ambient and elevated temperature

Figure 4-10(a) displays representative engineering stress-strain curves for all investigated samples at RT and 650 °C. Detailed tensile properties with comparison to existing literature are presented in Figure 4-10(b). A summary of the offset yield strength (OYS), ultimate tensile strength (UTS), uniform elongation (UE) and elongation at fracture (EL) is provided in Table 4-5. The results indicate that OYS, UTS, and ε_f for the currently studied samples at RT are generally higher than those reported for other DED SS316L samples [38, 103, 114, 104–106, 108, 110–113], and notably higher than wrought SS316L [114, 115]. High-temperature tensile properties also show better performance compared to conventional SS316L [86]. These findings demonstrate that LDED with optimized process parameters is capable of manufacturing superior tensile strength and ductility compared to the conventional counterparts. Specifically, the SDM800-YXZ samples exhibit the highest OYS, UTS, and the lowest uniform elongation at RT and 650 °C. In addition, regarding mechanical anisotropy, the SDM800 samples in the YXZ orientation demonstrate higher OYS and UTS but lower UE at both RT and 650 °C compared to the ZYX orientation. However, the SDM1600 samples show no measureable difference in mechanical properties between the ZYX and YXZ orientations within experimental error.

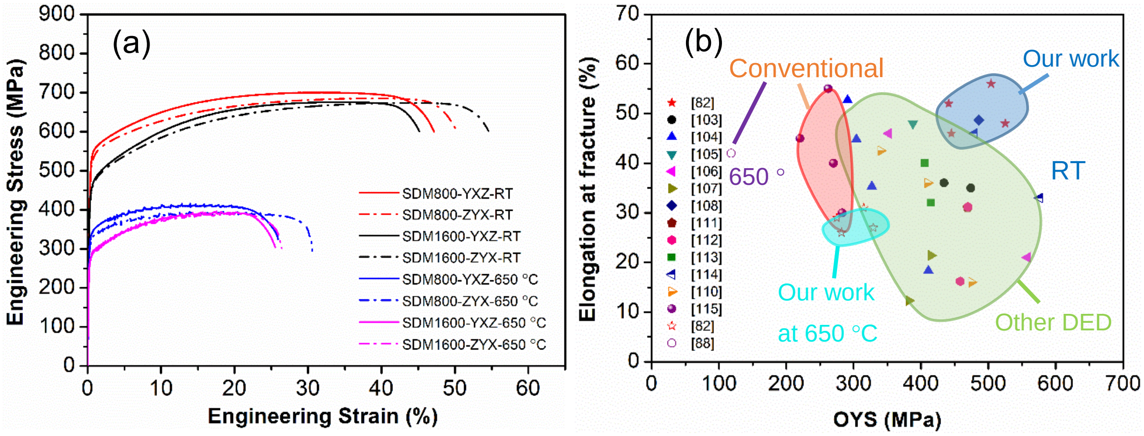

Figure 4-10 (a) Engineering stress-strain curves of all samples at different orientations; (b) Comparison of current results with literature.

Table 4-5 Summary of tensile properties of LDED specimens processed at different conditions.

Condition		OYS (MPa)	UTS (MPa)	UE (%)	EL (%)
SDM800-YXZ	RT	525 ± 4	702 ± 2	32 ± 1	48 ± 2
	650 °C	329 ± 5	415 ± 3	13 ± 1	27 ± 1
SDM800-ZYX	RT	504 ± 5	686 ± 1	41 ± 1	56 ± 3
	650 °C	315 ± 5	396 ± 1	16 ± 1	31 ± 2
SDM1600-YXZ	RT	445 ± 36	674 ± 13	34 ± 2	46 ± 6
	650 °C	282 ± 13	397 ± 1	17 ± 1	26 ± 1
SDM1600-ZYX	RT	441 ± 4	670 ± 3	40 ± 4	52 ± 7
	650 °C	275 ± 1	392 ± 1	20 ± 1	29 ± 1

4.3.3 Creep properties

Figure 4-11(a) depicts creep strain-rupture time curves for specimens tested at 650 °C and 225 MPa. The SDM800-YXZ samples exhibit distinctive creep curves with a significant improvement in the secondary creep stage, compared to the others. The remaining samples show a pattern of accelerated creep, lacking a clear secondary creep stage, consistent with the creep behaviour of PBF SS316L studied by Li et al. [84, 116]. Figure 4-11(b) details the primary and partial secondary creep stages. It is observed that both the duration of primary creep stage and the strains at the onset of secondary creep stage, particularly the strains at the onset of the secondary creep stage, increase as the laser beam size increase. The duration of primary creep and the strain at the onset of secondary creep stage has been reported to be related with the level of dislocation density produced in AM-materials [86, 88]. A previous study [89] examing the effects of heat treatment on the creep behavior of LDED SS316L has demonstrated that high-temperature heat treatment effectively facilitates the annihilation of LDED-induced dislocations, resulting in a prolonged duration of primary creep and increased strain at the end of the primary creep stage. Thereby, the differences observed in the duration of primary creep and the stain at the onset of secondary within various samples suggest variations in the degree of dislocation density generated under different conditions, i.e., a higher dislocation density in the SDM800 than in the SDM1600 sample.

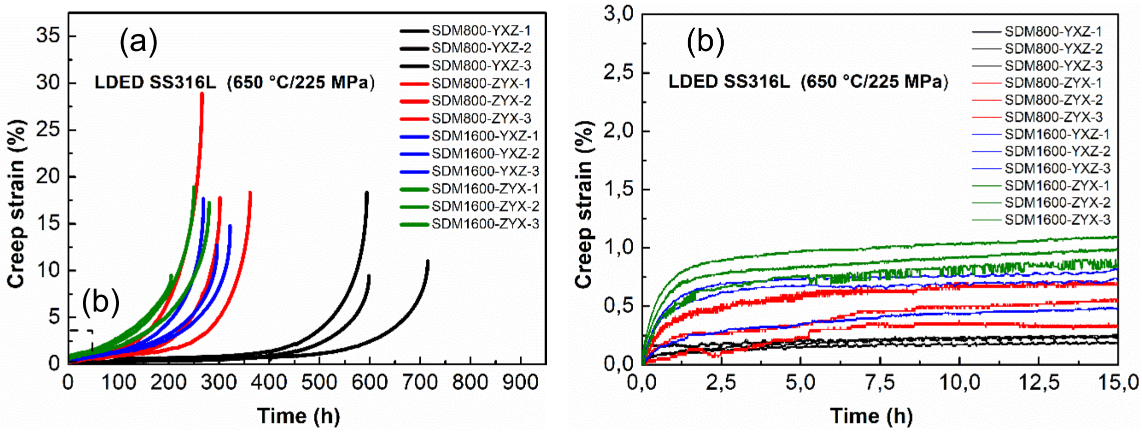

Figure 4-11 (a) Creep strain-time curves and (b) Details of primary creep stage for all samples tested at 650 °C and 225 MPa.

A summary of the creep rupture time (t_r), steady creep rate ($\dot{\varepsilon}_s$), and creep strain at fracture (ε_f) is shown in Figure 4-12. The details are provided in Table 4-6 and compared to other available creep data of AM-SS316L tested under identical conditions (650 °C and 225 MPa). The results show that all LDED samples outperform both LPBF SS316L and their conventional counterparts in creep resistance. Further comparisons between LDED and LPBF SS316L creep properties are discussed in previous work [14]. Among the LDED specimens, the SDM800-YXZ samples exhibit the longest t_r and lowest $\dot{\varepsilon}_s$ while the SDM1600-ZYX samples show the shortest t_r and highest $\dot{\varepsilon}_s$. Similar to the observed anisotropy in tensile properties, the YXZ orientation samples show superior creep properties compared to the ZYX orientation. However, this difference is more pronounced in the SDM800 samples, with the SDM800-YXZ orientation showing about a 50% increase in t_r and an 87% decrease in $\dot{\varepsilon}_s$ compared to the SDM800-ZYX orientation. In contrast, for the SDM1600 samples, the difference in creep behaviour between the ZYX and YZX orientations is minimal within experimental error.

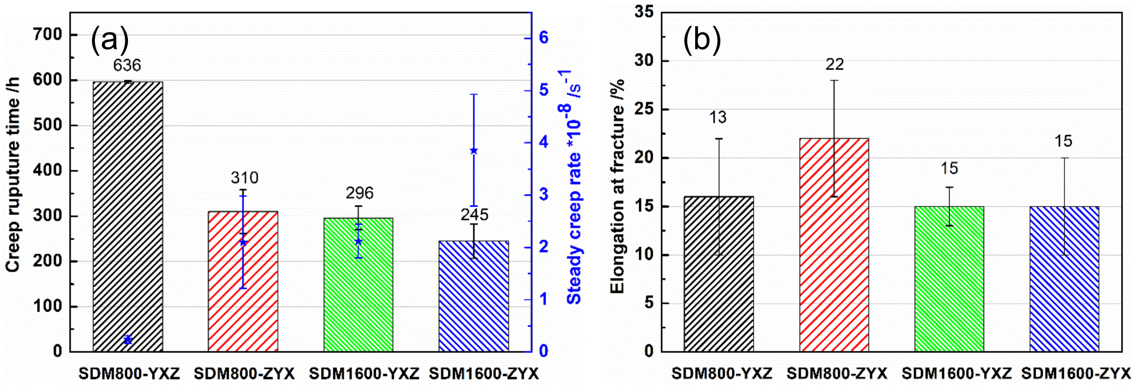

Figure 4-12 (a) Summary of creep rupture time and steady creep rate x 10^{-8} s^{-1} and (b) Creep elongation at fracture of all investigated SS316L samples tested at 650 °C and 225 MPa.

Table 4-6 Summary table of the creep rupture time (t_r), steady creep rate ($\dot{\varepsilon}_s$), and creep elongation at fracture (ε_f) for all of the tested cases at 650 °C and 225 MPa.

Condition	**t_r/h**	**$\dot{\varepsilon}_s$ x 10^{-8} s^{-1}**	**ε_f /%**	**Ref.**
SDM800-YXZ	636 ± 69	0.2 ± 0.1	13 ± 5	Current work
SDM800-ZYX	310 ± 48	2.1 ± 0.9	22 ± 6	
SDM1600-YXZ	296 ± 26	2.1 ± 0.3	15 ± 2	
SDM1600-ZYX	245 ± 38	3.9 ± 1.1	15 ± 5	
LPBF-Z	~12	~30	47	[72]
LPBF-XY	19.6	4200	~9	[75]
LPBF-Z	17.2	5000	10	[75]
LPBF-XY(heat-treated)	16.4	19	4.9	[70]
HR (Hot Rolled)	33.9	100	19.9	[70]

Figure 4-13 presents representative SEM images, EBSD-IPF maps and Kernel Average Misorientation (KAM) maps from cross-section of the ruptured creep samples to elucidate the damage mechanisms in samples with various process parameters. All post-creep specimens exhibit a final ductile fracture mode, characterized by evident necking near the fracture surface in Figure 4-13(a) and (c) and elongated melt pools in Figure 4-13(b) and (d). A typical creep failure mechanism involving micro-void coalescence and material separation perpendicular to the loading direction appears to occur in all specimens. EBSD and KAM analysis further reveals a predominant intergranular creep damage in all samples. However, the SDM800-YXZ samples show a unique creep damage pattern, including intergranular creep damage characterized by cavity-induced coalescence and propagation along regular grain boundaries (Figure 4-13a- a′), and significant plastic deformation at grain boundaries (Figure 4-13b″). In contrast, intergranular cracks in other samples are found in the regions transitioning between columnar grains and equiaxed grains (Figure 4-13b′-d′), with stress concentration near these transition areas (Figure 4-13b″-d″). Equiaxed grains with smaller grain sizes in LDED samples exhibit increased crack resistance during creep deformation, as evidenced by the observed variations in creep damage behavior.

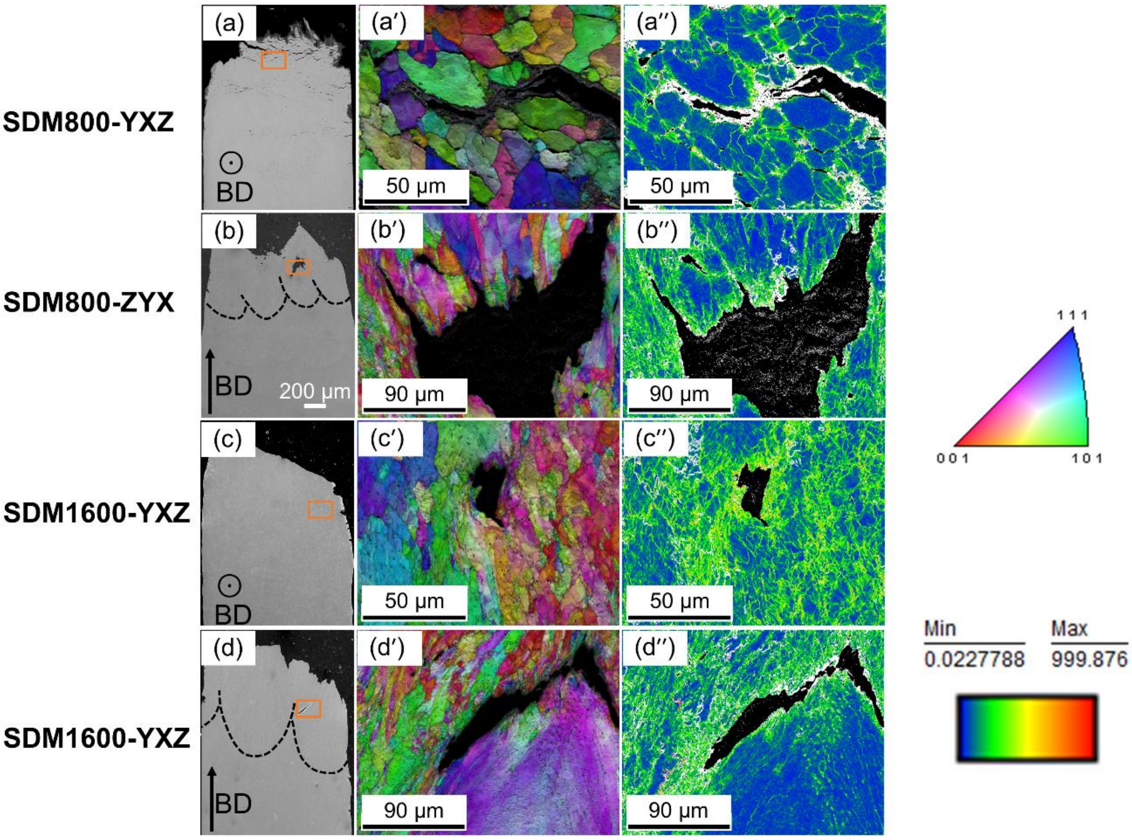

Figure 4-13 Comparison of damage mechanisms for all LDED samples. (a-d) SEM micrographs showing cross-section of creep-ruptured specimen. (a′-d′) EBSD IPF maps focusing on secondary cracks away from the fracture surface. (a″-d″) KAM maps illustrating stress distribution near cracks corresponding to EBSD maps in (a′-d′).

4.4 Discussion

By utilizing a laser beam that is twice as large, along with optimized process parameters, the build rate can be improved by 78%. This improvement results in a 58% reduction in powder consumption per print, therby increasing the efficiency of powder usage per print by 132%. Through in-depth analysis of microstructure, mechanical testing and fracture mechanism, the superior high-temperature tensile properties and creep performance of the LDED sample with an increased build rate can be explained. Furthermore, the observed variations in creep performance among the examined samples are also elucidated.

The low level of porosity produced in the LDED process contributes significantly to its superior high-temperature tensile and creep properties. AM-induced pores have been found to significantly impact creep behaviour, particularly affecting creep ductility [88]. The samples produced with a small laser beam exhibit a low porosity level (below 0.01%), which is expected to enhance creep performance. Conversely, the slightly higher porosity level in the SDM1600 sample may lead to reduced creep strength and creep ductility, breaking the typical strength-ductility trade-off. However, it is noteworthy that the LDED sample produced with a large laser beam still qualifies as nearly fully dense with porosity below 0.2%. Compared to conventional processed counterparts, LDED offers potential for achieving superior high-temperature tensile and creep properties with an improved build rate. Moreover, the role of grain boundaries precipitates in intergranular creep damage, as discussed in previous literature [46, 75], should also be considered. The relatively higher amount of delta ferrite at grain boundaries in the SDM1600 sample could account for its shorter creep life and inferior creep ductility, as delta ferrite at grain boundaries can initiate and accelerate the intergranular damage.

Additionally, the small grain size enhances high-tempertaure tensile and creep performance. Fracture damage analysis reveals that the superior creep properties of the SDM800-YXZ sample are due to the presence of small, regular, and uniformly distributed equiaxed grains on the XY-plane. Similar to the dislocation strengthening mechanism, small grains, featuring a higher density of grain boundaries per unit volume, enhances resistance to crack propagation during creep deformation. Furthermore, the dislocations generated by the LDED process have been shown to improve creep performance by effectively hindering dislocation movement during creep deformation. At the current testing temperature and stress level, creep deformantion is predominately governed by the dislocation power-law deformation mechanism. The relatively higher dislocation density in the SDM800 sample contributes to its superior creep properties, in contrats to the SDM1600 sample, which experiences a lower cooling rate.

Regarding anisotropy in high-temperature mechanical properties, especially in creep behaviour, the YXZ orientation (perpendicular to the build direction) in the LDED sample, produced using a small laser beam, demonstrates superior performance compared to the ZYX orientation (parallel to the build direction). Microstructural factors such as texture, directionally orientated columnar grain structure, and grain size variations are considered primary factors determining anisotropy in creep behavior [65, 76, 87, 117]. However, the absence of texture in the microstructure of the LDED sample and only slight differences in grain size are insufficient to fully account for the observed significant variations in creep performance. Therefore, the primary microstructural factor influencing anisotropy in creep behaviour is likely the variation in grain morphology between orientations. The predominant columnar grains in the ZY plane and more equiaxed grains in the XY plane contributes to the notable differences in creep performance, attributable to varying deformation mechanisms. Conversely, the SDM1600 sample, produced with a large laser beam and exhibiting less variation in grain morphology between orientations, does not show visible anisotropy in creep behaviour.

4.5 Summary

This chapter investigates the impact of process parameters on the high-temperature mechanical properties of LDED SS316L. The key findings are summarized as follows: Laser beam size is a critical factor affecting build rate, with larger beams significantly increasing it. Although both laser beam sizes maintain low porosity, smaller beams achieve exceptionally low porosity levels, below 0.1%, while larger beams also maintain commendable low porosity. Notably, microstructural differences arise from the laser beam size used. Smaller laser beams yield an anisotropic microstructure, with ZYX-oriented sample displaying predominantly columnar grains and YXZ-oriented samples showing smaller equiaxed grains. This leads to significant variations in tensile strength and creep behavior based on the sample orientation. In contrast, larger laser beams produce a uniform microstructure, eliminating these variations. Smaller laser beams demonstrate superior tensile strength and creep performance compared to larger laser beams.

Based on these findings, future research will focus on employing smaller laser beams, specifically the SDM800, along with optimized process parameters.

5 Effect of heat treatment on SS316L fabricated by LDED

5.1 Introduction

The aim of this chapter is to study the effect of post-processing heat treatment on the microstructure and high-temperature mechanical properties of SS316L fabricated by LDED. The investigation focuses on the microstructural changes induced by heat treatment and their corresponding impacts on the creep behaviour of the specimens.

5.2 Materials and methods

SS316L blocks deposited using the SDM800 parameters (refer to Table 4-2) were selected for heat treatment studies. These LDED-deposited SS316L blocks were annealed at various temperatures, specifically 300 °C, 600 °C, 800 °C, 1000 °C, and 1200 °C, each for a duration of one hour, as detailed in Figure 5-1. The annealing process was executed in a controlled environment within a furnace under a flowing argon atmosphere, heating at a rate of 20 °C/min. Following the annealing procedure, the samples were allowed to naturally cool down to room temperature within the furnace.

Samples for mechanical testing were cut and prepared with their loading direction perpendicular to the build direction. For mechanical testing and microstructural characterization, the methodologies employed were consistent with those described in the previous chapter.

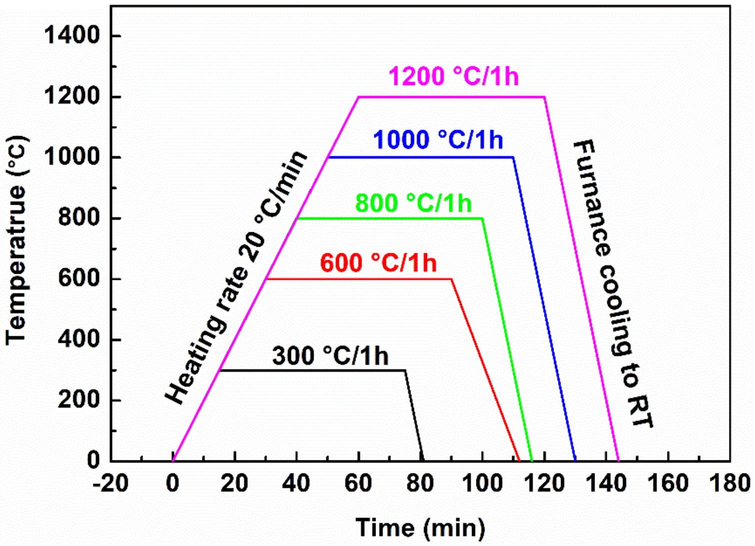

Figure 5-1 Annealing for as-deposited LDED-SS316L blocks.

5.3 Results

5.3.1 Microstructure

Figure 5-2 illustrates the changes in the solidification cellular microstructure of LDED as the annealing temperature varies. These structures, obserable in SEM images, arise from micro-segregation, with Cr and Mo identified at cell boundaries using TEM-EDS, as shown in Figure 5-3. Such enrichment in AM-SS316L is common [91, 93, 118] and typically forms under conditions that promote constitutional undercooling [119, 120]. The LDED cells, averaging 1.6 μm, are coarser than the sub-1 μm cells found in LPBF counterparts [19, 91], likely due to the slower cooling rate in LDED. These cells remain stable up to 600 °C but begin to decompose at 800 °C. Above 1000 °C, they vanish, as seen in Figure 5-2e and f, suggesting homogenization occurs above this temperature. Additionally, Mn and Si-rich oxides, ranging from 15-150 nm, were observed in Figure 5-3. As the annealing temperature increases, these particles grow in size but decrease in number, and at 1200 °C, they shift from spherical to prismatic shapes, likely transitioning from Rhodonite to Spinel [121]. The current findings are in agreement with earlier research [84, 93, 121].

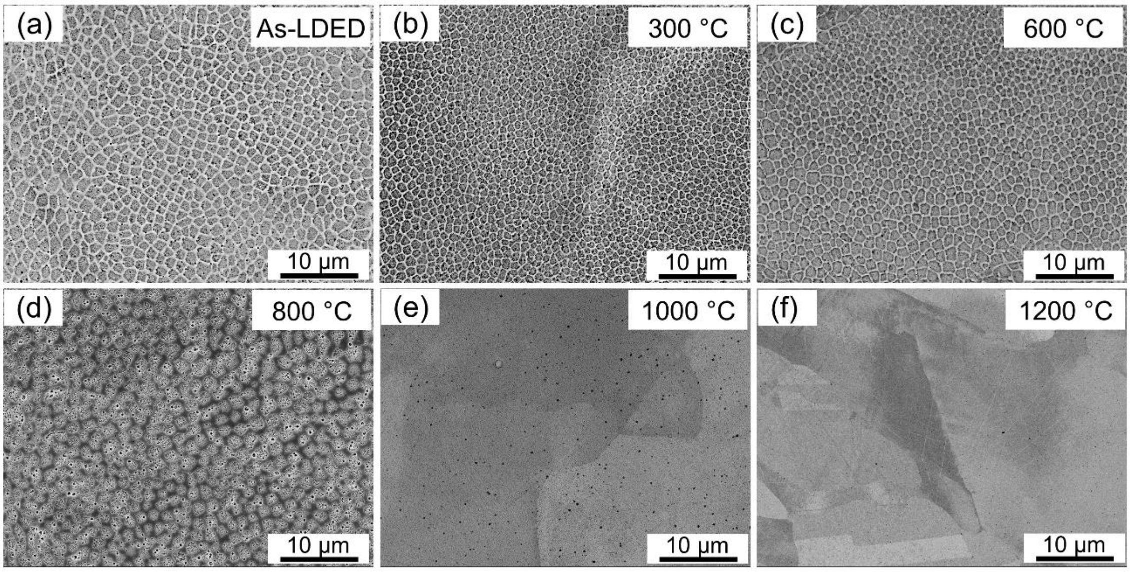

Figure 5-2 SEM micrographs of (a) as-LDED material and as-LDED specimens heat treated at (b) 300 °C, (c) 600 °C, (d) 800 °C, (e) 1000 °C and (f) 1200 °C.

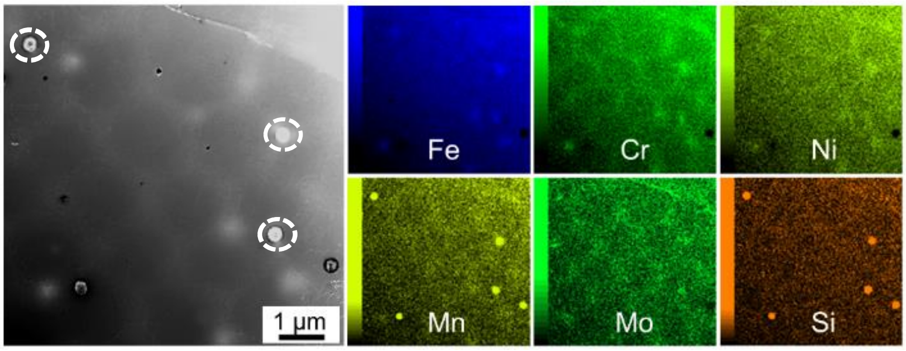

Figure 5-3 High-angle annular dark-field scanning TEM image and EDS elemental maps showing elemental segregation and presence of the oxide particles at cell boundaries in the sample annealed at 800 °C.

Figure 5-4 presents bright-field STEM images illustrating the dislocation structures in the as-deposited samples and those annealed up to 800 °C. It can be seen that, the LDED process results in nearly uniformly distributed dislocations, interspersed with sparse regions containing fine dislocation cells. These dislocation cell walls (DCWs) are highlighted with dashed lines in Figure 5-4(a), averaging around 400 nm in diameter. A closer examination, as shown in Figure 5-4(b), highlights areas with denser dislocations in contrast to dislocation-free zones adjacent to grain boundaries. In these areas, the tangled dislocations occasionally form quasi-dislocation cells, which differ from the dislocation cells commonly seen in LPBF materials, characterized by dense, tangled dislocation cell walls and clear cell interiors [91, 92]. Additionally, the nano-scale spherical oxides, as mentioned earlier, are observed across various annealing stages, indicated by the white dashed circles in Figure 5-4.

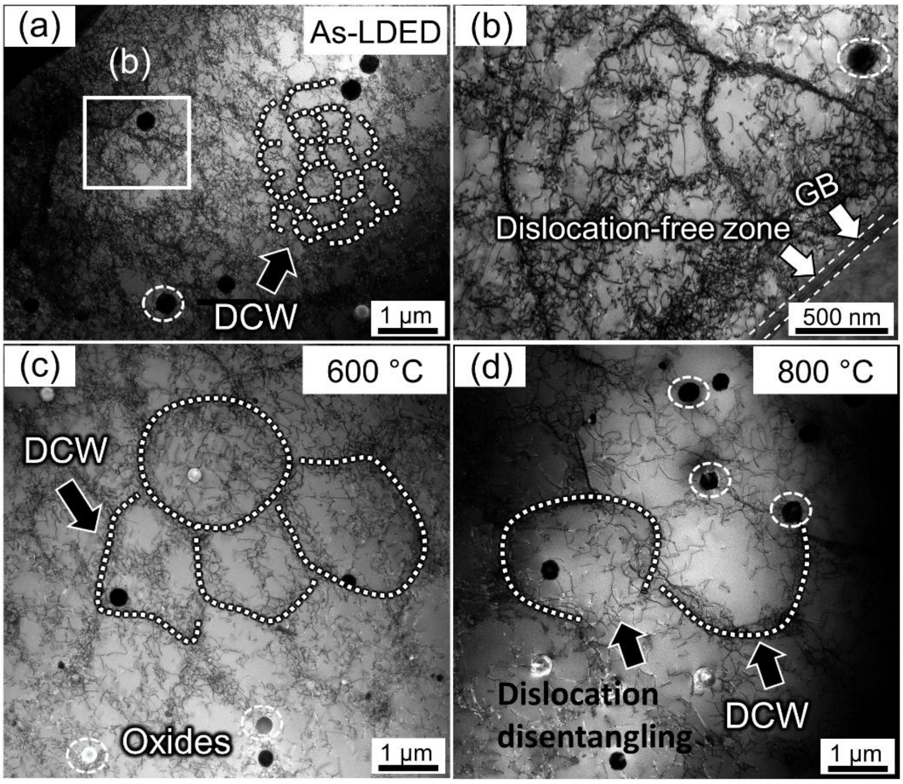

Figure 5-4 Bright-field STEM images showing dislocation structure of LDED-SS316L samples at as-deposited condition (a-b) and upon the annealing at the temperatures of 600 °C and (d) 800 °C.

During the LDED process, a non-equilibrium dislocation structure forms, which is inherently unstable. Post-heat treatments can stabilize this structure by enabling recovery, homogenization, and recrystallization processes [122]. When the annealing temperature is increased to 600 °C, there is a marked reduction in dislocation density, particularly within the cell interiors, as depicted in Figure 5-4(c). This reduction leads to the formation of distinct dislocation cells, the average size of which matches the cellular structures observed in SEM. At temperatures above1000 °C, these cells disappear, as illustrated in Figure 5-4(d).

EBSD analysis in Figure 5-5 reveals grain orientation and morphological changes upon post-heat treatment. The as-deposited LDED sample has a mixed microstructure of large columnar and smaller equiaxed grains, consistent with prior reports [123, 124], which remains stable up to 1000 °C. At 1200 °C, while grain growth is evident, the overall grain morphology remains unchanged, indicating minimal recrystallization activity. This observation differs from findings reported for LPBF processes in [93]. Deng et al. [122] suggest that the thermal stability of dislocation structures in AM SS316L correlates with its ability to recrystallize. Contrary to LPBF, LDED shows recovery below 600 °C and almost no recrystallization even at 1200 °C.

Furthermore, no distinct textural patterns are evident across the annealing spectrum, and a consistent austenite phase is observed, aligning with findings in references [93, 125].

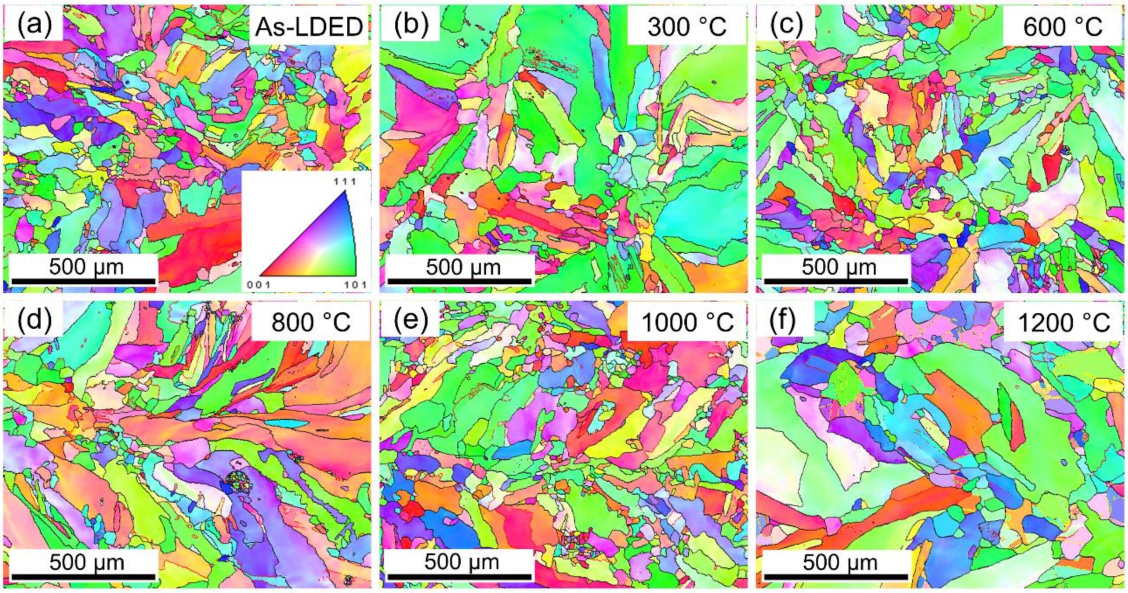

Figure 5-5 IPF grain orientation maps for (a) as-LDED sample and specimens heat treated at (b) 300 °C, (c) 600 °C, (d) 800 °C, (e) 1000 °C, and (f) 1200 °C.

5.3.2 Tensile properties at ambient and elevated temperature

Tensile tests at room and elevated temperatures were conducted across all conditions. Figure 5-6(a) and (b) display the engineering stress-strain curves at RT and 650 °C, while Figure 5-6(c) charts the tensile properties (OYS, UTS, and UE at RT and 650 °C) as a function of annealing temperature. Average values, along with standard deviations for OYS, UTS, and UE, are provided in Table 5-1. Up to 300 °C, the OYS remains consistent. However, a minor drop in OYS and UTS, along with enhanced ductility, is noticed at 600 °C, likely due to a reduced dislocation density from recovery processes. The OYS and UTS averages for as-deposited LDED, and samples annealed at 300 °C and 600 °C, considerably exceed the values for wrought SS316L, approximating 300 and 600 MPa respectively [126, 127]. A noticeable decline in OYS begins at 800 °C, corresponding with the decomposition of dislocation cells. Above this temperature, while OYS continues to decrease, UE rises, showing a typical strength-ductility compromise. UTS shows a mild reduction as the annealing temperature increases. The tensile properties at elevated temperature, as influenced by the annealing temperature, exhibit a trend similar to the properties observed at room temperature with respect to annealing temperature. Figure 5-6(d) compares these findings with literature on LPBF SS316L [93, 125, 128–130].

The trend of OYS with annealing temperature mirrors prior reports on SS316L. A detailed analysis of these observations is provided in the discussion section.

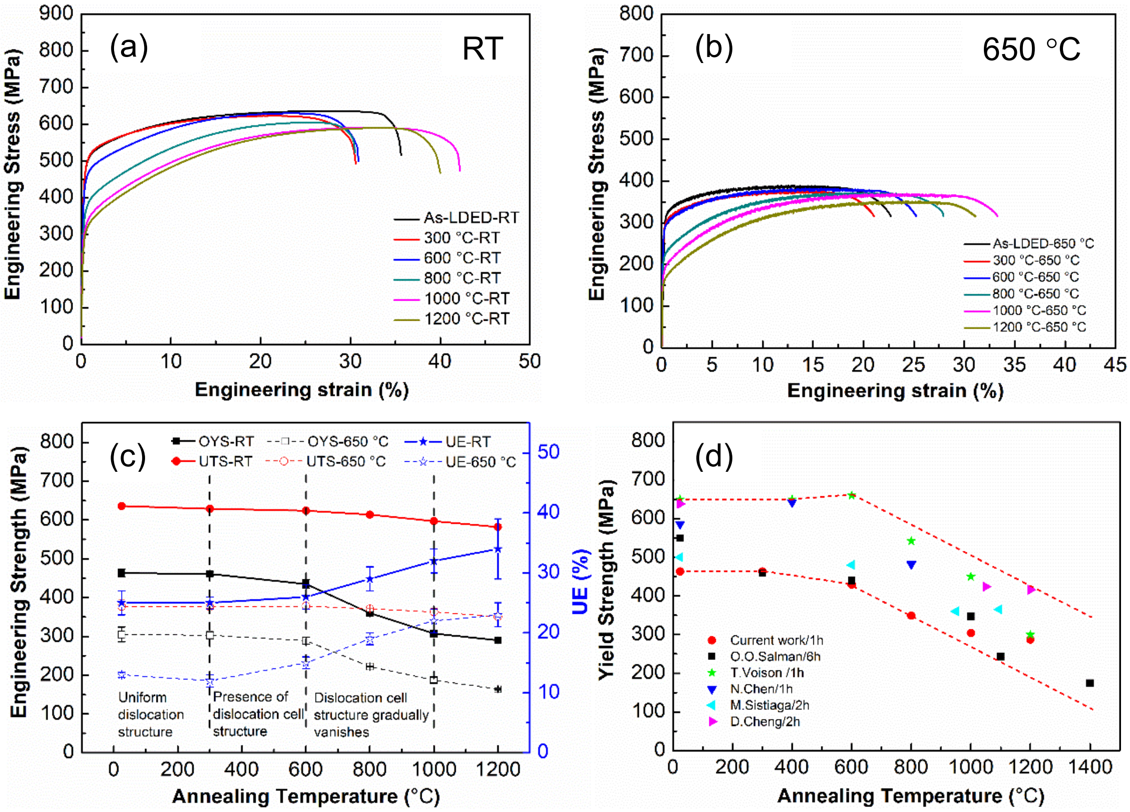

Figure 5-6 Tensile properties of LDED specimens. (a) Engineering tensile stress-strain curves at room temperature. (b) Engineering tensile stress-strain curves at 650 °C. (c) Evolution of room and elevated temperature OYS, UTS, and UE with increasing annealing temperature, and (d) Comparison of yield strength as a function of annealing temperature between the LDED SS316L and studies reported in the literature for LPBF SS316L.

Table 5-1 Summary of the average values and standard deviations for OYS, UTS and UE of as-LDED and annealed specimens tested for various annealing conditions.

Condition	**OYS/MPa**		**UTS/MPa**		**UE/%**	
	RT	**650 °C**	**RT**	**650 °C**	**RT**	**650 °C**
As-DED	463 ± 22	305 ± 19	629 ± 16	377 ± 17	25 ± 2	13 ± 1
300 °C	463 ± 11	303 ± 9	622 ± 6	376 ± 4	24 ± 2	12 ± 1
600 °C	429 ± 2	289 ± 9	605 ± 3	378 ± 7	23 ± 0.2	15 ± 1
800 °C	349 ± 5	222 ± 1	605 ± 1	371 ± 2	25 ± 2	19 ± 1

Table 5-2 (continued): Summary of the average values and standard deviations for OYS, UTS and UE of as-LDED and annealed specimens tested for various annealing conditions.

1000 °C	304 ± 5	187 ± 7	597 ± 6	363 ± 10	32 ± 2	22 ± 2
1200 °C	287 ± 7	164 ± 2	585 ± 7	351 ± 1	31 ± 2	23 ± 2

5.3.3 Creep Properties

Figure 5-7a displays the representative creep strain-rupture time curves for as-deposited and annealed specimens under testing conditions of 650 °C and 225 MPa. A detailed examination of the primary and secondary creep stages is provided in Figure 5-7b. As can be seen that, as-deposited LDED samples exhibit a concise primary creep phase, paired with minimal strain upon entering the secondary creep phase. As the annealing temperature increases, the duration of the primary stage and the strain at the end of the primary stage also increase compared to the as-deposited state. Such a limited primary creep phase is typical for AM-materials, often attributed to their high initial dislocation density [86, 88]. This heightened dislocation concentration constrains the material's potential for further hardening. With increasing annealing temperatures, which facilitate the reduction of LDED-induced dislocations, both the duration of the primary stage and the starting strain at the minimum creep rate extend.

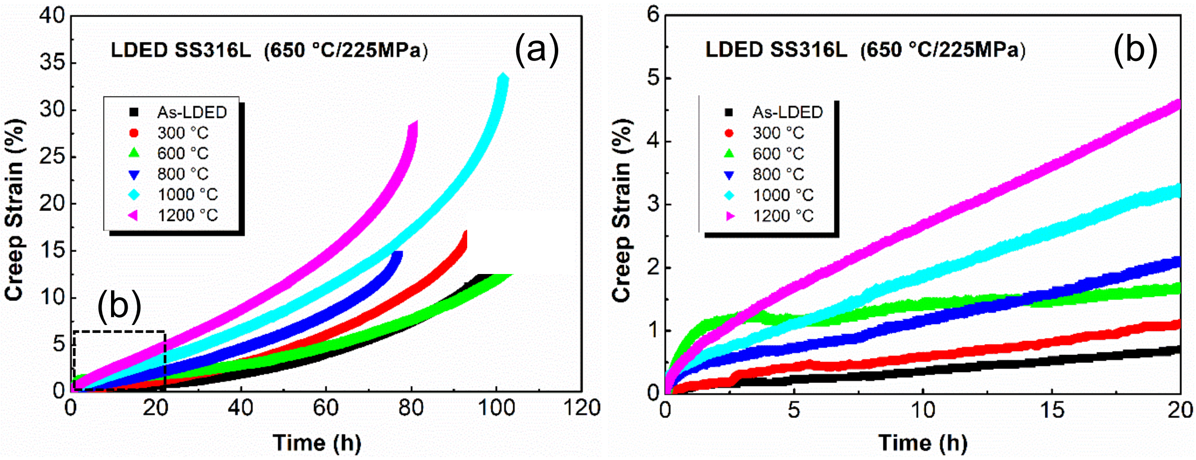

Figure 5-7 (a) Creep strain-time curves and (b) Detail in primary and secondary stage for all LDED SS316L samples tested at 650 °C and 225 MPa.

Figure 5-8 graphically presents the creep properties: t_r, $\dot{\varepsilon}_s$ and ε_f in relation to the annealing temperature. Table 5-3 lists the average values and standard deviation for these creep properties. Interestingly, the evolution of creep properties with annealing temperature is more complex than that of tensile properties. Up to an annealing temperature of 600 °C, there is negligible variation in creep metrics, with values remaining consistent within experimental margins. At 800 °C, $\dot{\varepsilon}_s$ notably escalates, approximately tripling the rate observed in as-deposited samples. However, ε_f remains relatively unchanged, leading to a significant reduction in t_r. Following annealing at 1000 °C, an increased $\dot{\varepsilon}_s$ is accompanied by a sharp increase in ε_f, resulting in a slight increase in t_r compared to the samples annealed at 800 °C. Finally, the 1200 °C heat treatment leads to a further rise in $\dot{\varepsilon}_s$, but both t_r and ε_f decrease.

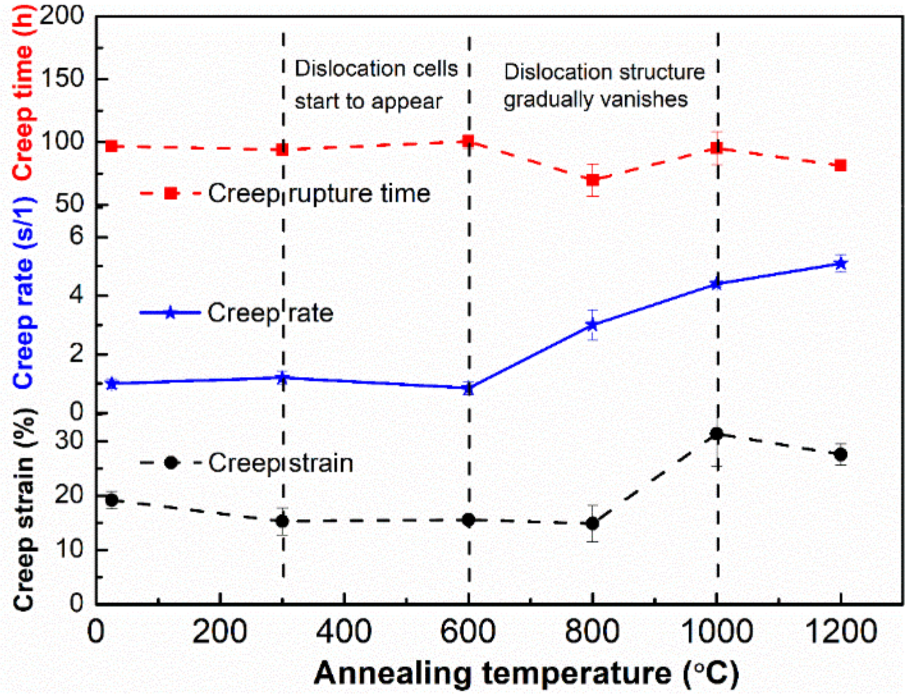

Figure 5-8 Creep rupture time, steady creep rate $*10^{-7}$ s^{-1} and creep strain as a function of annealing temperature of LDED SS316L samples tested at 650 °C and 225 MPa.

Table 5-3 Summary of creep properties: t_r, $\dot{\varepsilon}_s$, and ε_f for all of the tested cases.

	As-LDED	**300 °C**	**600 °C**	**800 °C**	**1000 °C**	**1200 °C**
t_r /h	97 ± 3	94 ± 1	100 ± 5	70 ± 13	95 ± 13	81 ± 3
$\dot{\varepsilon}_s$ $*10^{-7}$ / s^{-1}	1.0 ± 0.2	1.2 ± 0.2	0.9 ± 0.1	3.0 ± 0.5	4.4 ± 0.1	5.1 ± 0.3
ε_f /%	19 ± 2	15 ± 2	16 ± 1	15 ± 3	31 ± 6	28 ± 2

5.4 Discussion

The formation of a uniform dislocation structure in the current LDED material is explained through comparison with LPBF material. Unlike LPBF, where dislocations form well-defined cells, LDED produces evenly distributed dislocations. This distribution is influenced by the dislocation density and solidification microstructure, particularly primary dendrite arms [131]. High dislocation density is essential for the fine dislocation cells seen in LPBF, similar to those created under various mechanical stresses [132–134]. Factors like thermal gradients, cooling rates, and the number of thermal cycles, all governed by additive manufacturing parameters, affect dislocation density by influencing residual stresses, strains, and solidification dendrite structures.

The LDED process typically exhibits lower thermal gradients and cooling rates compared to LPBF, due to factors such as a larger beam size in LDED (800 μm) versus LPBF (around 100 μm [131]), higher deposition rates, and greater layer thickness (250 μm in LDED against approximately 30 μm in LPBF [93]). These differences result in LDED producing a more uniform dislocation structure with reduced dislocation density compared to LPBF. Additionally, the fewer heating/cooling cycles in LDED, owing to its thicker layers, further reduce dislocation density and limit distortion. In LDED, the larger dendrite spacing is a consequence of the reduced cooling rate and thermal gradient, with the size of solidification cells being approximately 1.6 μm, notably larger than the 0.5 μm in LPBF. This results in a distinctive alignment of dislocations; unlike LPBF, where dislocation cell sizes often correspond to dendrite dimensions at solidification boundaries, LDED shows predominantly uniform dislocations, not aligning with dendrite micro-segregation.

Annealing at 600 °C transforms the homogenous dislocation distribution of LDED into dislocation cells. This transformation is primarily influenced by chemical micro-segregation within the sample, which significantly affects the formation of the dislocation cell structure and its thermal stability. Notably, the size of the dislocation cell tends to match that of the solidification cellular structure. Above 600 °C, the dislocation density within both the cell interior and cell walls diminishes. This reduction correlates with the ongoing diffusion of trapped elements, leading to the disintegration of the dislocation cells formed at 600 °C. This phenomenon highlights the role of micro-segregation in maintaining the stability of the dislocation cell structure in LDED samples.

The tensile properties of LDED SS316L contrast notably with those of LPBF SS316L. This disparity in OYS primarily arises from variances in dislocation density and cell size. Notably, the strength of AM SS316L is inversely related to the diameter of dislocation cell [19]. This difference in OYS persists through annealing temperatures. Regardless of the build technique, both LDED and LPBF SS316L display thermal instability above 600 °C, characterized by a decline in OYS due to the dissolution of elemental micro-segregation and the lose of dislocation cells. Furthermore, while LPBF material maintains higher dislocation density at 600 °C, its strengthening effect diminishes as elemental micro-segregation diffuses above this temperature.

The creep behavior of LDED SS316L is also significantly influenced by annealing temperature, remaining stability up to 600 °C and increasing in $\dot{\varepsilon}_s$ above 800 °C. Dislocation structure, critical to tensile strength, similarly affects creep performance, with increased creep rates and reduced dislocation density above 600 °C. The significant rise in $\dot{\varepsilon}_s$ above 600 °C is attributed to decreasing dislocation density and loss of dislocation cell structure. Furthermore, the relationship between annealing temperature and t_r is complex. While t_r decreases at 800 °C, it unexpectedly improves at 1000 °C, contradicting existing literature trends [84, 116]. This improvement at 1000 °C, a temperature without chemical micro-segregation, is likely due to increased tertiary creep strain. Comparisons between LDED and LPBF SS316L reveal that LDED specimens have markedly longer t_r, especially under specific orientations and conditions, up to four times longer than those found in LPBF [79, 86, 88]. Additionally, LPBF specimens reach minimum creep rates at lower strains compared to LDED. The finer dislocation cell structure in LPBF, contributing to shorter creep stages, contrasts with the lower dislocation density in LDED, which enhances plastic deformation and improves creep performance. For a detailed discussion on this topic, readers are referred to the published work [89].

5.5 Summary

The chapter provides significant insights into the thermal stability of dislocation structures and their impacts on high temperature mechanical performance. Initial observations of the as-deposited material disclosed unique microstructures marked by elemental micro-segregation (mainly Mo and Cr) and uniformly distributed dislocations. Upon annealing at 600 °C, uniform dislocations evolved into coarser cell-like structures, which had slight implications for yield strength and ductility. Within the temperature range of 600-800 °C, a reduction in dislocation density was associated with a decrease in yield strength and an increase in creep rate. Above 1000 °C, the dissolution of dislocation structures and micro-segregations led to a further decrease in yield strength and an accelerated creep rate, although the onset of a more homogeneous microstructure contributed to a balanced creep rupture. The mechanical behavior and stability of dislocation structures were found to be highly dependent on chemical micro-segregation, especially below 600 °C.

6 Effect of heat treatment on IN718 fabricated by LDED

6.1 Introduction

This chapter explores how heat treatments affect the high-temperature mechanical properties of IN718 fabricated through LDED. It examines a range of heat treatments designed to optimize the microstructure and enhance creep performance. The primary objective is to understand the intricate relationship between microstructural modifications and the resulting creep behaviors in IN771, with a goal to identify the optimal heat treatment for LDED IN718.

6.2 Materials and methods

InssTek MX-600 was also used to fabricate IN718 blocks. A set of LDED process parameters for IN718 (average laser power of 373 W; scanning speed of 14 mm/s; hatch distance of 0.5 mm, laser beam diameter of 0.8 mm, layer thickness of 0.25 mm, powder feed rate of 2.8 g/min), provided by the manufacturer, was utilized to fabricate cubes with the identical dimensions of 35× 35 × 35 mm^3 (X, Y, Z), respectively. Commercially available gas-atomized IN718 alloy powder from AP&C, with a particle size distribution of 50 to 150 µm was used. The chemical composition of the IN718 powder is shown in Table 6-1. The benchmark material, a wrought alloy in the form of a rolled square bar (⌀ 70 *130 mm^2), was purchased from Rolled Alloy, Inc. The benchmark material (composition in Table 6-1) was annealed according to the AMS 5663 standard [135].

Table 6-1 Nominal chemical composition (in wt. %) of the as-deposited IN718 powder and commercial wrought alloy.

Material	Ni	Cr	Nb	Mo	Ti	Al	C	Fe
IN718	53.32	19.00	5.21	3.14	0.88	0.62	0.04	Bal.
Wrought	52.25	19.00	5.13	3.05	0.90	0.50	0.04	Bal.

Table 6-2 summarizes various heat treatments applied to the as-deposited samples to tailor the grain structure and dissolve undesired secondary phases, such as the Laves phase and δ phase, thus promoting the precipitation of strengthening precipitates. Standard heat treatments, designed for conventional cast and wrought nickel alloy according to the AMS 5383 [136] and AMS 5663 standard were also selected for a comparative analysis of the creep behavior of LDED sample with their conventional counterparts.

Table 6-2 Heat treatment schedules applied to experimental materials.

Condition	Designation	1st step: Homogenization	2nd step: Solution Anneal	3nd step: Aging
As-deposited	AD	--	--	--
Double aging	DA	--	-	720 °C/8h/FC 50 °C/h + 620 °C/8h/AC
Standard heat treatment	SA	--	980 °C/1h/WC	
Standard heat treatment	HSA	1080 °C/1h/WC	980 °C/1h/WC	
Homogenization heat treatment at 1080 °C	HA-1080 °C	1080 °C/1 h/water cooling	-	
Homogenization heat treatment at 1180 °C	HA-1180 °C	1180 °C/1 h/water cooling	-	
Hot isostatic pressing and double aging treatment	HIP-DA	1180 °C/100 MPa/4 h	-	

For mechanical testing and microstructural characterization, the methodologies employed were consistent with those described in the previous chapter.

6.3 Results

Given the variety of conditions explored, this section will emphasize representative results. These selected findings will clearly demonstrate the influence of heat treatment on the microstructure and high-temperature mechanical properties of LDED-IN718. More details, results and discussion can be found in the published work [46, 75].

6.3.1 Microstructure

The microstructural features of LDED-manufactured IN718, at as-depoisted state and in comparison to its wrought counterpart, are presented in Figure 6-1. EBSD IPF maps distinctly illustrate variations in grain characteristics between the two conditions. The LDED sample displays coarse, anisotropic columnar grains, a result of epitaxial growth not strictly aligned with the build direction, as shown in Figure 6-1(a) and (b). Factors like location-specific thermal profiles or heterogeneous nucleation in remelted zones likely contribute to this grain irregularity [59]. SEM micrographs in Figure 6-1(d-e) further highlight elemental segregation within the interdendritic regions of the LDED-created columnar grain structure, leading to the emergence of irregular Laves phase precipitates. This precipitate with similar morphology and composition in LDED material has been observed and confirmed in previous work [48, 137–139]. The wrought sample, on the other hand, displays a uniform fine-grained structure stabilized by δ particles, which also appear at grain boundaries, as shown in Figure 6-1(c) and (f). TEM analyses at higher magnifications in Figure 6-1(g-h) reveal a pronounced dislocation density within the LDED sample matrix, attributed to thermal stresses from varying deposition rates [65]. These dislocations tend to cluster more around sub-grain boundaries, possibly due to pinning by segregated precipitates. In contrast, the wrought material shows negligible dislocation evidence shown in Figure 6-1(i).

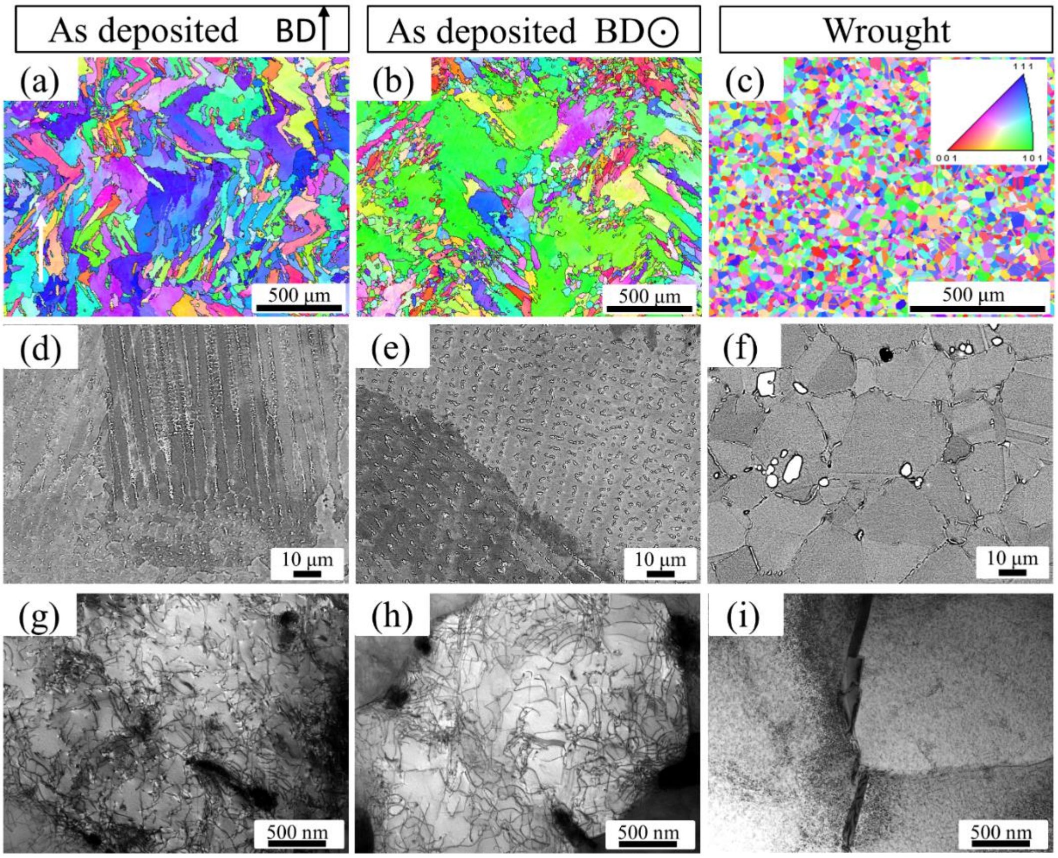

Figure 6-1 Microstructural comparison between LDED as-deposited and wrought samples. The representations include EBSD IPF maps (a-c), SEM BSE images (d-f), and TEM-Bright Field (BF) images (g-i). From left to right: as-deposited sample aligned with the building direction, as-deposited sample perpendicular to the building direction, and the wrought sample.

Figure 6-2 presents the microstructure of the LDED processed material under various heat-treated conditions. These conditions bring about notable transformations such as grain coarsening, the shift from columnar to equiaxed grains, dissolution of the Laves precipitates, emergence of γ′/γ″ strengthening phases, and modifications to the dislocation subgrain structure. EBSD analysis in Figure 6-2(a-c) highlights substantial grain growth and recrystallization in the HSA sample, while DA and SA samples show minimal alterations. The HSA sample exhibits more pronounced, recrystallized grains, in contrast to the irregular columnar grains retained from the LDED process in the DA and SA samples. Table 6-3 provides qualitative data on grain and precipitate sizes across different heat-treated and wrought samples. HSA samples consistently present larger grains across both orientations compared to other samples. Notably, EBSD <110> pole figures (Figure 6-2a-c insets) suggest texture strength diminishes as heat treatment temperature rises. DA and SA samples display a pronounced <110> // scanning direction texture, which transitions to a more isotropic pattern in HSA samples.

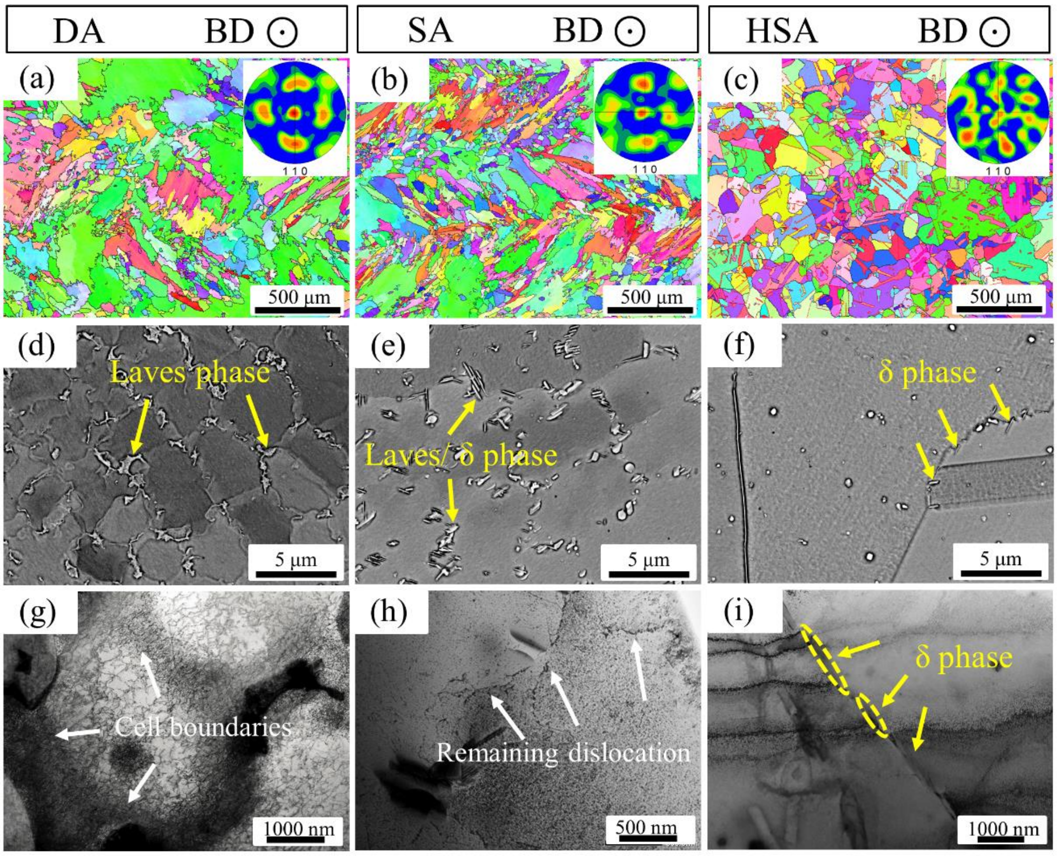

Figure 6-2 Microstructural analysis of heat-treated LDED IN718 samples. Columns represent different samples: DA (first), SA (second), and HSA (third). Rows showcase: (a-c) EBSD IPF images with <110> PF insets, (d-f) SEM-BSE images, and (g-i) TEM-BF depictions. All micrographs are oriented parallel to the build direction.

Table 6-3 Statistics of the average grain diameter and the average length of γ″ for different heat treated samples and wrought sample.

	As-deposited	**DA**	**SA**	**HSA**	**Wrought**
Dxy /μm	276 ± 249	245 ± 194	271 ± 143	601 ±351	-
Dyz /μm	192 ± 131	277 ± 276	273 ± 127	463 ± 266	30 ± 11
Lγ″ / nm	-	23 ± 6	22 ± 9	16 ± 5	18 ± 5

Figure 6-2(d-f) outline phase evolution for all heat-treated LDED samples. Irregular Laves particles appear interdendritically in the DA state (see Figure 6-2d). In the SA sample, while many Laves phases dissolve, some remnants persist, enveloped by δ phase and acicular carbide (see Figure 6-2e). However, in the HSA sample (see Figure 6-2f), Laves phases are completely dissolved, revealing only the needle-like, Nb-rich δ phase and Nb and Ti-rich carbides. These carbides, formed during solidification, remain stable across the evaluated temperature spectrum. The established phase transition sequence is Liquid (L) → L + γ → L + γ + NbC → L + γ + NbC + Laves → L + γ + NbC + Laves + δ [140, 141].

The microstructure of LDED processed material, including its cellular substructures shaped by dislocations, is depicted through SEM (Figure 6-2d-f) and TEM (Figure 6-2g-i) techniques. Contrary to the dense dislocations seen in LPBF-manufactured materials in prior studies [66, 142], the current coarse columnar structure exhibits fewer dislocations at the cellular subgrain boundaries. The DA sample (Figure 6-2d and g) highlights cell subgrains intertwined with dislocations, which remain stable at lower heat treatment temperatures. Although post-solution annealing at 980 °C for 1 h in the SA sample (Figure 6-2e and h) reduces dislocation density within cell interiors, individual dislocations, marked by white arrows, continue to mark the thinner cell walls. Notably, dislocations appear to promote precipitate formation, given the alignment of both. However, at elevated temperatures of 1080 °C, dislocation cell subgrains vanish, with the matrix appearing pristine and free from LDED-induced dislocation cellular structures, as evidenced in Figure 6-2(i).

TEM dark field images in Figure 6-3 display the strengthening γ′ and γ″ precipitates in the heat-treated LDED-IN718 samples and the wrought state. The as-deposited state lacks detectable γ′/γ″ precipitates, likely due to rapid AM process cooling, aligning with prior studies [11]. All heat-treated and wrought states exhibit dispersed, thin, ellipsoidal γ″ precipitates with minimal spherical γ′ particles, aligning with previous studies [143, 144]. A representative selected area electron diffraction (SAED) pattern from {100} matrix planes, depicted in Figure 6-3(e), shows strong matrix γ reflections with weaker superlattice γ′ and γ″ phase reflections. The diffraction pattern reveals three γ″ variants, with the γ-matrix and γ″ phase orientation detailed as {100}γ″//{100}γ; <100>γ″ //<100>γ [145]. Table 6-3 lists the average γ″ particle lengths, with HSA samples having the shortest and DA the longest. Notably, the HSA sample displays evenly distributed γ′ and γ″ precipitates without dislocations, while SA samples show precipitates predominantly near dislocations, as indicated in Figure 6-3(b). Coupled with prior findings, dislocations seem to accelerate intragranular precipitation in SA material, as seen in previous studies [66].

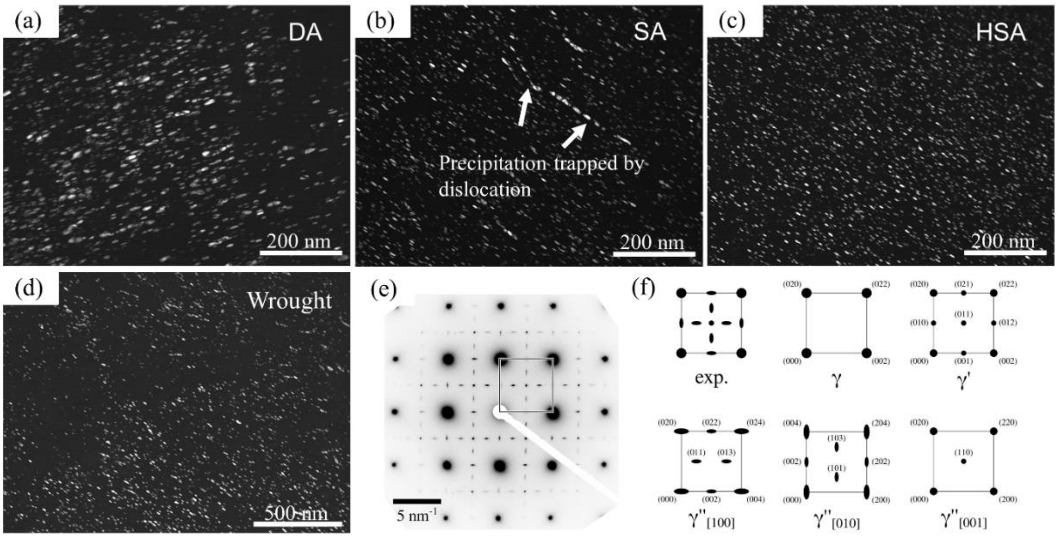

Figure 6-3 TEM-DF micrographs highlighting γ″ precipitates in the [010] zone axis for (a) DA, (b) SA, (c) HSA, and (d) Wrought samples. (e) Representative SAED pattern oriented in the <100> matrix zone and (f) Annotated guide to the SAED pattern.

6.3.2 Tensile properties at ambient and elevated temperature

Tensile properties of ZYX- and YXZ-oriented specimens, at both room and elevated temperatures, are presented in Figure 6-4 and compared to those of wrought specimens. Graphs depicting the values of OYS, UTS, UE obtained from tensile tests at both RT and 650 °C are shown in Figure 6-5. The details of the tensile properties are provided in Table 6-4. As detailed in Figure 6-5, both heat treatment and sample orientation significantly influence these tensile properties at RT and 650 °C. All heat-treated samples exhibit a pronounced increase in OYS and UTS but a decrease in UE compared to the as-deposited samples. Within the same loading direction, the tensile strength of heat-treated samples follows the sequence: DA > Wrought > SA > HSA. Additionally, the data displays the anisotropic nature of tensile properties across all heat-treated samples. YXZ-oriented specimens consistently demonstrate a higher OYS than their ZYX-oriented counterparts. However, this difference diminishes with increased heat treatment temperature, leading to almost isotropic tensile properties for HSA specimens.

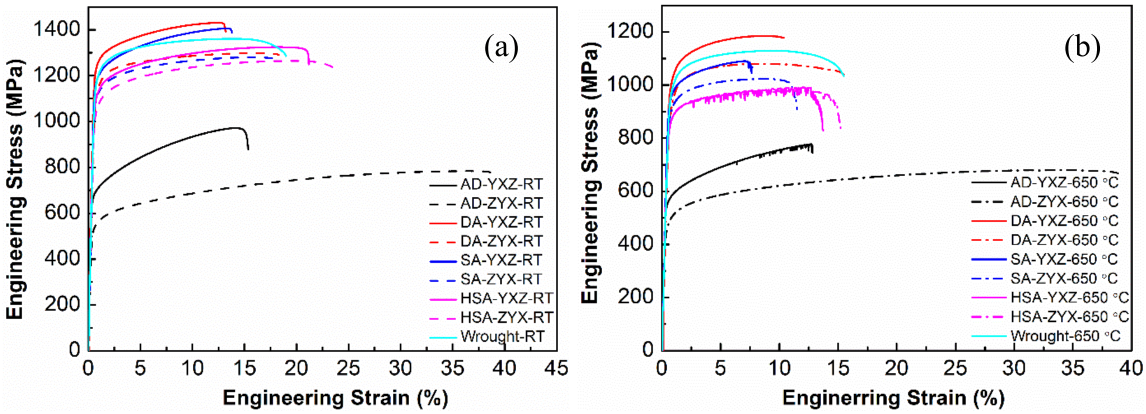

Figure 6-4 Engineering stress-strain curves of all investigated LDED heat-treated specimen and wrought specimen at (a) RT and (b) 650 °C.

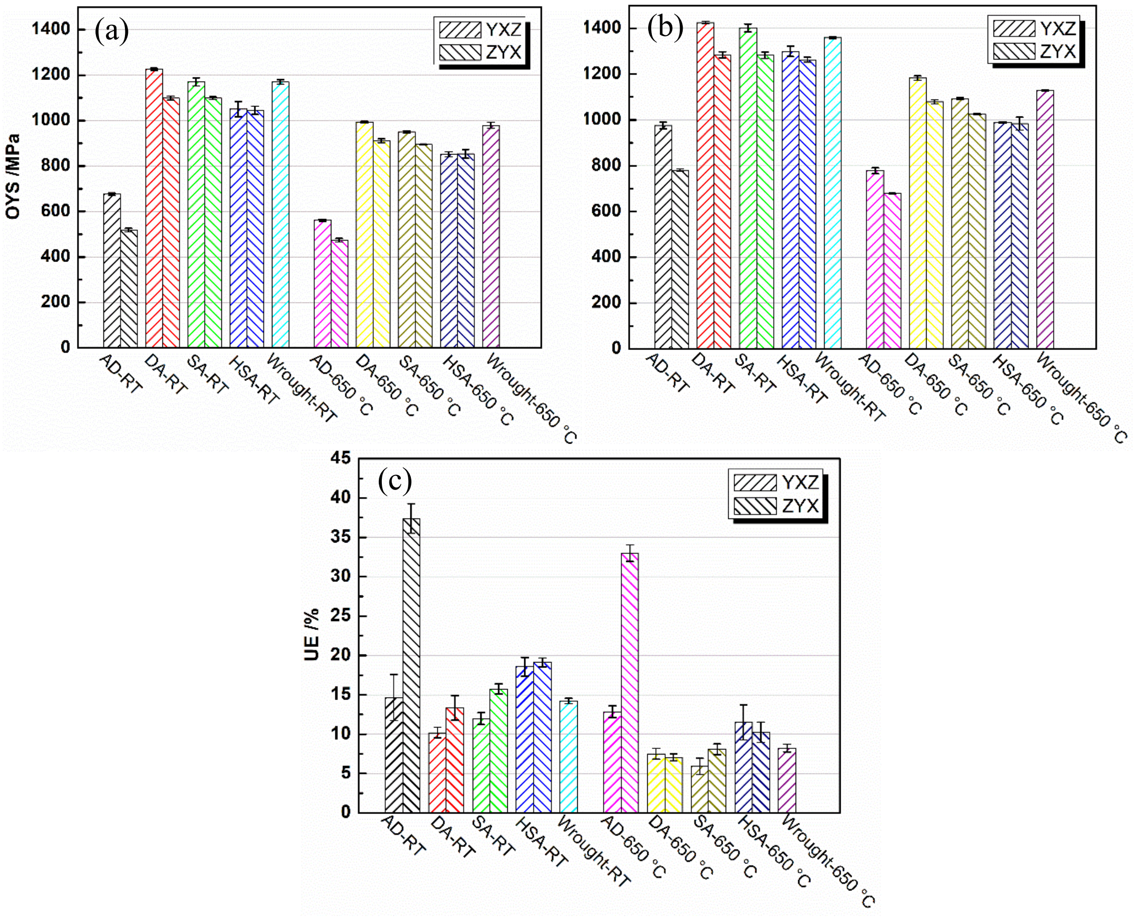

Figure 6-5 Summary graphs of tensile properties at both RT and 650 °C. (a) OYS, (b) UTS and (c) UE.

Table 6-4 Summary of tensile properties of LDED-IN718 specimens processed at different conditions and compared with literature data.

Condition	**Test temperature °C**	**OYS MPa**	**UTS MPa**	**UE %**	**EL %**	**Ref.**
Wrought	RT	1170 ± 10	1359 ± 4	14 ± 1	25 ± 2	Current work
	650	979 ± 13	1129 ± 4	8 ± 1	14 ± 1	
AD-YXZ	RT	677 ± 5	975 ± 15	15 ± 3	16 ± 3	
	650	562 ± 5	778 ± 13	13 ± 1	13 ± 2	
AD-ZYX	RT	518 ± 8	780 ± 5	37 ± 2	40 ± 2	
	650	474 ± 8	679 ± 2	33 ± 1	38 ± 1	
DA-YXZ	RT	1225 ± 5	1425 ± 5	10 ± 1	11 ± 1	
	650	992 ± 4	1182 ± 10	7 ± 1	9 ± 1	
DA-ZYX	RT	1099 ± 9	1284 ± 13	13 ± 2	15 ± 2	
	650	911 ± 9	1079 ± 9	7 ± 1	13 ± 2	
SA-YXZ	RT	1170 ± 18	1401 ± 17	12 ± 1	13 ± 1	
	650	950 ± 4	1093 ± 5	6 ± 1	7 ± 1	
SA-ZYX	RT	1099 ± 6	1282 ± 10	16 ± 1	18 ± 1	
	650	895 ± 2	1024 ± 3	8 ± 1	11 ± 1	
HSA-YXZ	RT	1050 ± 33	1299 ± 22	19 ± 1	22 ± 2	
	650	851 ± 11	989 ± 3	12 ± 2	14 ± 3	
HSA-ZYX	RT	1045 ± 18	1263 ± 10	19 ± 1	25 ± 2	
	650	854 ± 19	983 ± 28	10 ± 1	13 ± 2	
AD-YXZ	RT	632 ± 13	972 ± 13	21 ± 1	24 ± 1	[30]
AD-ZYX	RT	517 ± 7	829 ± 41	22 ± 7	23 ± 8	
AD-Z	RT	590	845		11	[146]

6.3.3 Creep properties

Creep properties, specifically t_r, $\dot{\varepsilon}_s$, and ε_f, for the aforementioned specimens are outlined in Figure 6-6, with a summarized overview in Table 6-5. It can be seen that, the DA sample achieves the longest t_r and ε_f, along with the lowest $\dot{\varepsilon}_s$. In contrast, the HSA sample records the shortest t_r and ε_f, accompanied by the highest $\dot{\varepsilon}_s$. The benchmark wrought sample's creep values lie between those of the DA YXZ-oriented and the HSA YXZ-oriented samples, closely mirroring the SA YXZ-oriented sample, although its ε_f exceeds that of the SA specimen. A discernible anisotropy in creep properties is also evident across all heat-treated samples. YXZ-oriented specimens generally exhibit superior creep properties compared to ZYX-oriented ones. However, as the heat treatment temperature increases, this disparity diminishes, resulting in nearly isotropic creep properties for the HSA samples.

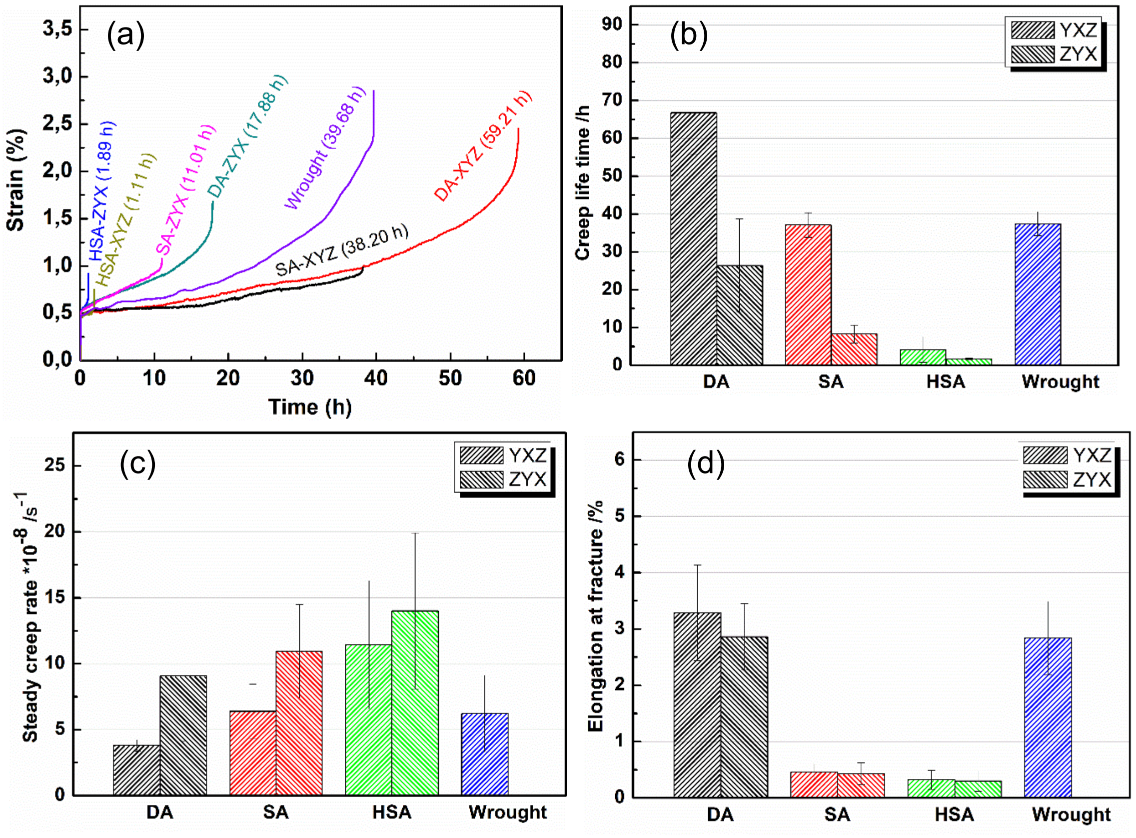

Figure 6-6 Creep properties of LDED-specimens compared to conventional wrought specimens: (a) Creep life time-strain curves at 650 °C/750 MPa, and summary graphs of (b) t_r (c) $\dot{\varepsilon}_s$ and (d) ε_f for all of the tested cases.

Table 6-5 Summary table of creep properties: t_r, $\dot{\varepsilon}_s$, and ε_f for all of the investigated states.

Condition	**DA**		**SA**		**HSA**		**Wrought**
	YXZ	**ZYX**	**YXZ**	**ZYX**	**YXZ**	**ZYX**	
t_r /h	66.8 ± 10.9	26.4 ± 12.3	37.1 ± 3.2	8.3 ± 2.4	4.2 ± 5.4	1.7 ± 0.2	37.5 ± 3.1
$\dot{\varepsilon}_s$ *10^{-8} / s^{-1}	3.8 ± 0.4	9.1 ± 5.0	6.4 ± 2.1	11.0 ± 3.5	11.4 ± 4.9	14.0 ± 5.9	6.2 ± 2.9
ε_f /%	3.3 ± 1.9	2.9 ± 2.6	0.5 ± 0.1	0.4 ± 0.2	0.3 ± 0.2	0.3 ± 0.2	2.8 ± 0.7

EBSD and KAM maps, as shown in Figure 6-7, illustrate crack propagation behaviors in heat-treated and wrought specimens. DA samples, as observed in Figure 6-7(b), feature irregular columnar grains, which enhance creep resistance due to increased plastic deformation. In contrast, SA specimens show reduced deformation, indicating weaker creep resistance. The HSA condition transitions into larger equiaxed grains with more regular boundaries, potentially accelerating crack propagation. Additionally, cracks in HSA specimen are predominately observed at the interfaces between different grain regions, a finding corroborated by prior research [77]. The wrought specimen, characterized by regular grain boundaries, possesses shorter, finer grains that could hinder crack growth. Notably, damage sites, highlighted by increased misorientation and presented as red points, are primarily located in specific regions of the DA and SA specimens, and mainly within grain boundaries in the HSA and wrought specimens. These sites, aligning with prior microstructural findings, appear to coincide with the presence of Laves and δ phases, which may initiate cracks and reduce creep resistance.

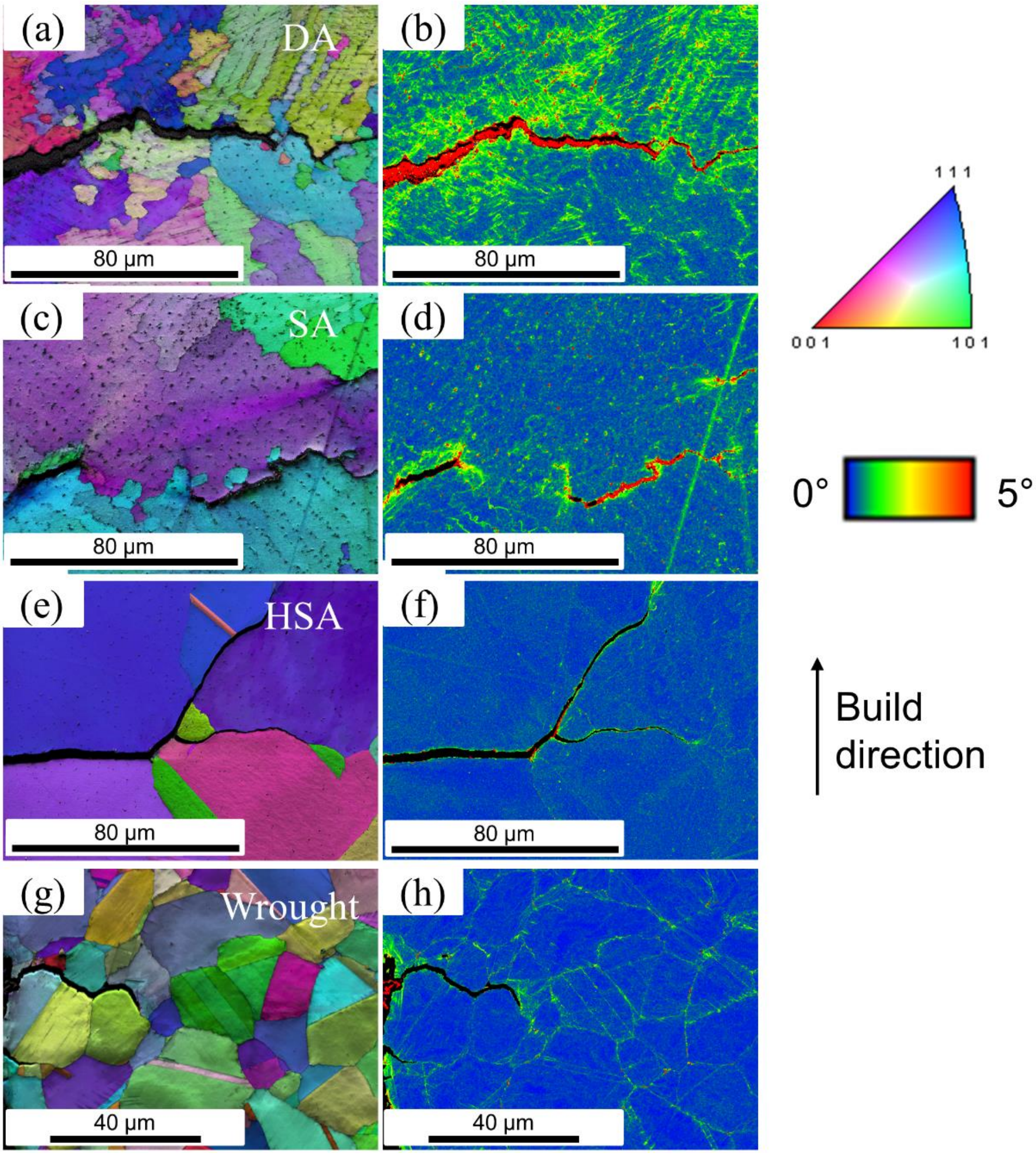

Figure 6-7 EBSD IPF maps of cross section of ZYX-oriented post-creep samples (a) DA, (c) SA, (e) HSA, (g) Wrought; The corresponding KAM maps, (b) DA, (d) SA, (f) HSA and (h) Wrought, respectively.

6.4 Discussion

The creep performance in this chapter is closely linked to the microstructural changes in heat-treated LDED IN718 materials versus their wrought counterparts. The present findings align with prior studies [147, 148], suggesting creep performance at 650 °C/750 MPa is governed by the dislocation power law mechanism. Factors affecting this creep mechanism are explored below.

The primary strength of the material is attributed to the γ′/ γ″ precipitates, particularly γ″, due to their role in obstructing dislocation motion. The effectiveness of γ″ precipitate largely depends on their size, volume fraction, and the availability of the γ″ forming element (Nb). The dissolution of the Laves phase and the subsequent precipitation of the δ phase affects the availability of Nb. As indicated by previous studies, increasing the temperature during heat treatment can enhance the availability of Nb for γ″ precipitation. However, the experimental creep strength does not show a linear correlation with the amount of available Nb, suggesting other variables influence the creep performance.

A critical factor in deteriming creep strength is the size of the γ″ precipitates. Previous research [149] shows that γ″ does not undergo coarsening during short-term exposure to current temperatures. Therefore, the γ″ sizes measured via TEM before creep testing can provide insights into their impact on creep performance. Chaturvedi and Han [148] identified an optimal γ″ size of around 23 nm. In this study, the measured sizes were as follows: DA: 23 ± 6 nm, SA: 22 ± 9 nm, Wrought: 18 ± 5 nm, HSA: 16 ± 5 nm. The superior creep strengths of the DA and SA sample can be attributed to their larger γ″ sizes. However, these size differences are relatively small, suggesting that other critical factors affecting creep strength require further investigation.

Laves and δ phases, especially at grain boundaries, have been identified as initiating cracks that negatively impact creep performance, consistent with other research [60, 74, 150, 151]. The size, number, and distribution of these phases are crucial in shaping creep deformation [151]. Despite having more Laves phase, SA specimens show a creep lifetime comparable to wrought specimens, suggesting that factors other than Laves phase volume influence creep strength. This is further evidenced by the exceptional creep ductility in DA condition, despite its high Laves phase content.

Grain size also plays a significant role in creep strength. Larger grains typically enhance enhance creep resistance due to fewer grain boundaries. However, Figure 6-8 indicates that increased grain size may actually undermine creep performance. HSA specimens with larger grains show reduced creep life and creep rates, while wrought specimens with smaller grains exhibit better creep lifetimes. Studies on wrought 718 alloy [148] and observations by Xu et al. [74] on forged specimens with small grains versus LPBF specimens with larger grains support this trend. However, the large-grained DA-XYZ and SA-XYZ specimens still match or surpass the creep life of wrought specimens, implying that additional strengthening mechanisms in DA and SA conditions may mitigate the negative impact of large grain size on creep performance.

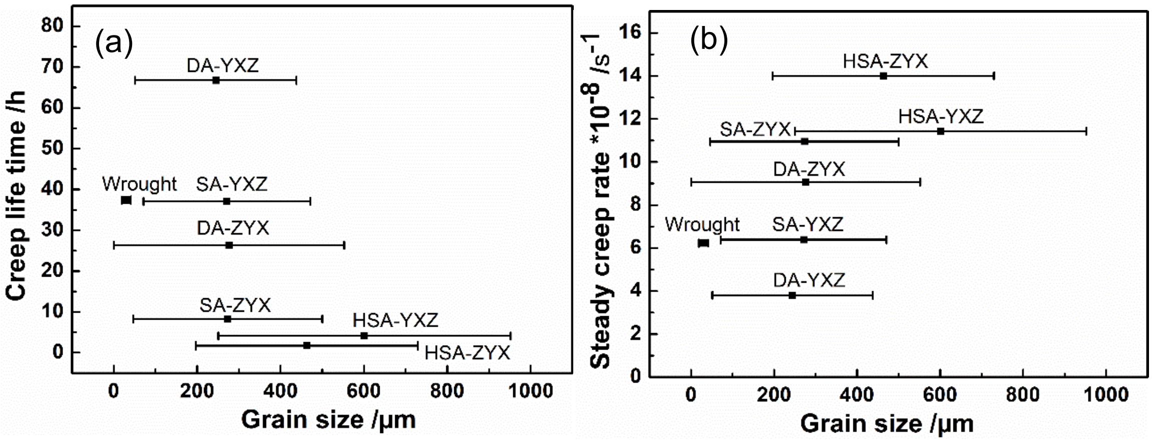

Figure 6-8 Relationship between the grain size and (a) the creep life time and (b) the steady creep rate for all considered states.

DA samples show improved creep life and ductility due to their retained dislocation substructures from the as-deposited state, which impedes dislocation movement, enhancing strength and ductility [93, 142, 152, 153]. While high strength can accelerate creep void formation, the LDED process, compared to other LPBF techniques, produces a lower dislocation density, facilitating stress relaxation. The production of irregular columnar grains and complex grain boundaries during LDED process also helps deflect crack growth in DA samples. For SA samples, even with reduced dislocation density, some dislocation structure and grain features support creep strength. Conversely, HSA samples exhibit inferior creep performance due to the recrystallized grains and the lack of a dislocation substructure.

Anisotropy in creep behavior related to sample orientation is evident in this study, aligning with prior research that show anisotropic grain structure significantly impacts the mechanical properties of AM-materials [18, 154, 155]. High-temperature heat treatment mitigates this anisotropy by modifying the microstructure, reducing differences in creep properties between YXZ and ZYX specimens. Unlike other studies favoring Z-oriented specimens for creep resistance [62, 67, 76], this study reveals superior performance in YX-specimens, likely due to differences in grain structure and orientation. While grain size is similar in both orientations, the improved creep performance of YXZ specimens may result from their more randomized grain orientation and strong texture, as well as the influence of dislocations from the LDED process.

6.5 Summary

The influence of heat treatment on the high-temperature mechanical properties of the Inconel 718 alloy fabricated using LDED method were thoroughly examined, with a benchmark comparison to the conventional wrought alloy. Key findings reveal that DA-treated specimens excelled in performance, demonstrating the longest creep life, the slowest steady-state creep rate, and the highest elongation at fracture. This enhanced behavior is attributed to the dislocations substructure and the unique irregular columnar grains formed during the LDED process, along with a complex grain boundary network. In contrast, HSA specimens exhibited less favorable creep properties, likely due to the formation of a coarser and recrystallized grain structure. SA specimens achieved a creep life comparable to that of wrought alloys, while retaining some structural characteristics induced by LDED, though with a reduced creep ductility, potentially owing to the obstructive presence of Laves and δ phase. When subjected to identical heat treatments, the specimens exhibited variations in creep resistance depending on sample orientation. Specimens oriented in the XY plane demonstrated superior creep resistance compared to those oriented in the Z plane. This disparity can be attributed to the orientation of columnar grains and the crystallographic texture in each sample. However, it is important to note that this anisotropy becomes significantly less pronounced as the temperature of the heat treatment increases.

This chapter has identified optimal heat treatment conditions crucial for enhancing the high-temperature mechanical properties of LDED IN718. This discovery, especially the effectiveness of a double aging process, complements the previously established optimal heat treatment for LDED SS316L. Together, these optimized treatments for both materials pave the way for establishing a robust protocol for the heat treatment of FGMs IN718/SS316L.

7 High temperature mechanical behavior of LDED-FGM SS316L/IN718

7.1 Introduction

After an in-depth investigation of IN718 and SS316L, encompassing the determination of optimal process and heat treatment parameters, this chapter shifts focus to the high-temperature mechanical behavior of the final FGMs IN718/SS316L produced via LDED. The emphasis is on evaluating their mechanical performance at elevated temperatures, particularly after heat treatment. This essential assessment is designed to verify their durability under thermal stress, a critical factor for their use in high-performance environments.

7.2 Materials and methods

The same SS316L and IN718 powders used in previous chapters were utilized to fabricate the dissimilar and functionally graded material SS316L/IN718. These powders were fed from separate feeders into the nozzle and delivered onto the substrate using argon as the carrier. In the deposition process, SS316L powder was inititally deposited to form approximately half of the total height of the final block, followed by the deposition of IN718 powder atop the SS316L layers, as schematically shown in Figure 7-1(a). With gradients change from SS316L to IN718 along the build direction, the laser power was optimized ranging from 500 W to 373 W while maintaining other process parameters constant (scanning speed of 849 mm/min, hatch distance of 0.5 mm, laser beam diameter of 0.8 mm, layer thickness of 0.25 mm, and powder feed rate about 2.8 g/min). After deposition process, the LDED SS316L/IN718 gradient blocks were divided into two groups. One was at the as-deposited condition (abbreviated as AD); and the other one was subjected to a two stage aging treatment, 720 °C/8 h/furnace cooling + 620 °C/8 h/air cooling (abbreviated as HT). This heat treatment was based on the previous studies examining the effects of heat treatments on individual LDED-SS316L and LDED-IN718 materials [46, 75, 89].

To investigate the sample orientation effect on tensile and creep properties, the ZYX-oriented and YZX-oriented sample cut from the individual materials and FGM region were tested respectively, as illustrated in Figure 7-1(b). For mechanical testing and microstructural characterization, the methodologies employed were consistent with those described in the previous chapters.

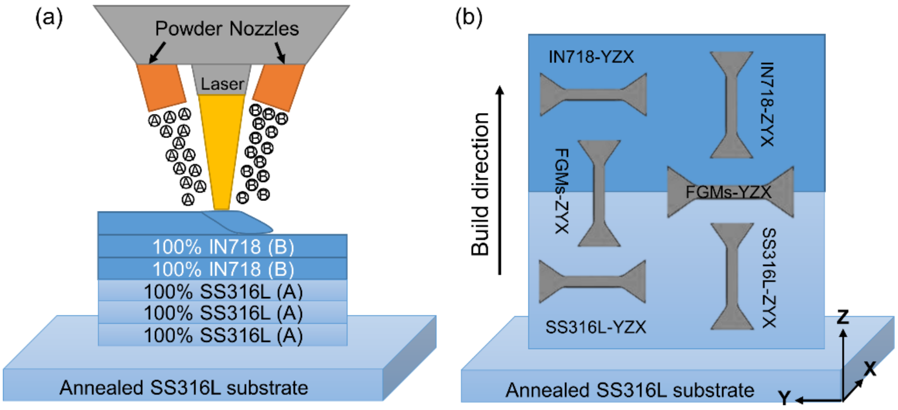

Figure 7-1 (a) Schematic depicting deposition process of FGMs SS316L/IN718 via LDED and (b) Orientation and geometry of samples for mechanical testing.

7.3 Results

7.3.1 Microstructure

Figure 7-2 shows the chemical compositions along the deposited direction before (a) and after heat treatment (b). Fe and Ni, the primary elements of SS316L and IN718, indicate the controlled gradation of compositions. The addition of IN718 leads to a decrease in Fe and an increase in Ni, a trend consistent in both AD and HT conditions. The targeted deposition strategy for the FGMs results in a narrow gradation region in the AD condition, with a transition of about 0.5 mm (spanning two layers of 0.25 mm each) separating the SS316L-rich and IN718-rich areas, as shown in Figure 7-2(a). After heat treatment, this transition region extends, doubling in size compared to the AD condition, as evidenced in Figure 7-2(b). The HT condition demonstrates a more gradual gradient, suggesting that heat treatment facilitates elemental redistribution and smoothes the gradient structure, particularly in the IN718-rich region. This effect is evident in the elemental distribution at the IN718 and SS316L interface, where the introduction of IN718 modifies the composition near the interface, allowing elements from the IN718 region to diffuse towards the SS316L boundary, a phenomenon also observable in the AD condition.

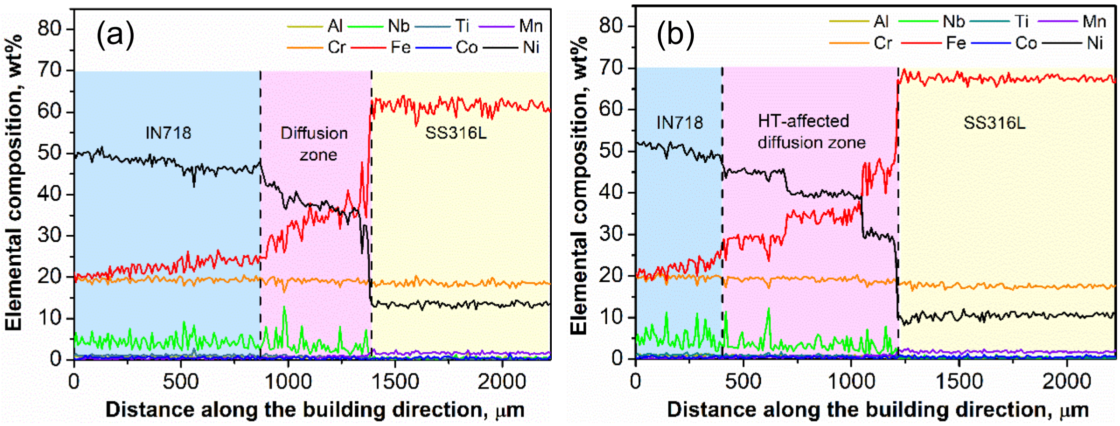

Figure 7-2 EDS profiles for FGMs gradient sample in (a) AD (a) and (b) HT conditions.

EBSD analysis presented in Figure 7-3 offers a crystallographic view of the HT-affected interface. The microstructure of the FGMs sample features an austenitic matrix with a consistent FCC lattice throughout the gradient. Before HT, despite the noticeable Fe shift at the SS316L and IN718 interface (see Figure 7-3a), the coarse grains from the SS316L region continue to grow, preserving their crystallographic orientation (see Figure 7-3b). As grains in the IN718 region grow, the pattern shifts from coarse grains in SS316L to finer ones in IN718. The grain orientation then adjusts to the direction of maximum heat flow. EBSD findings show grain sizes of 280 ± 145 μm in the SS316L region and 149 ± 100 μm in the IN718 region.

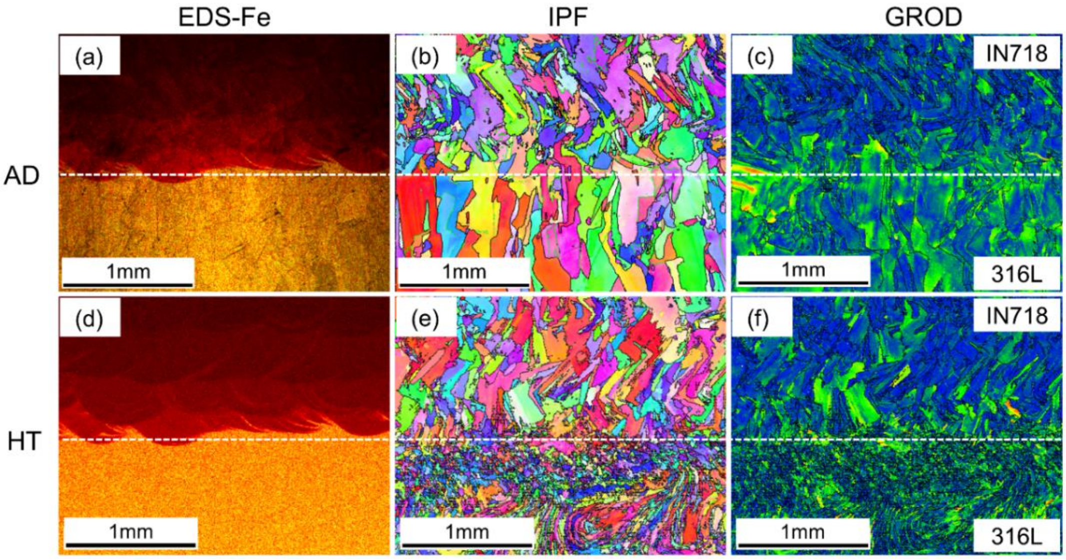

Figure 7-3 EBSD analysis for gradient sample in the (a-c) AD and the (d-f) HT condition. The first column depicts EDS-Fe profile across the interface (a) (d), the second column is IPF, (b) (e) and last column displays grain reference orientation deviation (GROD) map (c) (f).

After HT, the EDS-Fe profile highlights a distinct interface effect in the vicinity of IN718, as shown in Figure 7-3(d). EBSD-IPF analysis after HT shows transformations in the SS316L region near the interface, as depicted in Figure 7-3(e). The coarse dendritic grains present before HT are refined into equiaxed grains, while the IN718 region maintains its grain size and shape. EBSD measurements record grain sizes of 51 ± 29 μm in SS316L and 143 ± 89 μm in IN718, consistent with pre-HT values. Using grain reference orientation deviation (GROD) maps, which track orientation changes during the plastic deformation of crystalline materials, the heat treatment-induced recrystallization near the SS316L interface is identified. A comparison of GROD maps, before (Figure 7-3c) and after HT (Figure 7-3f), indicates that the recrystallization is driven by higher energy levels in grains near the SS316L interface, likely due to increased plastic deformation during the LDED process [18].

Figure 7-4 displays the microstructure of the FGMs sample after heat treatment. Prior studies have already examined the microstructure of this sample in its as-deposited state [30, 38], noting its almost full density and absence of cracks under the deposition parameters. The heat treatment largely perserves the unique microstructural features inherent to the LDED process compared to the AD state.

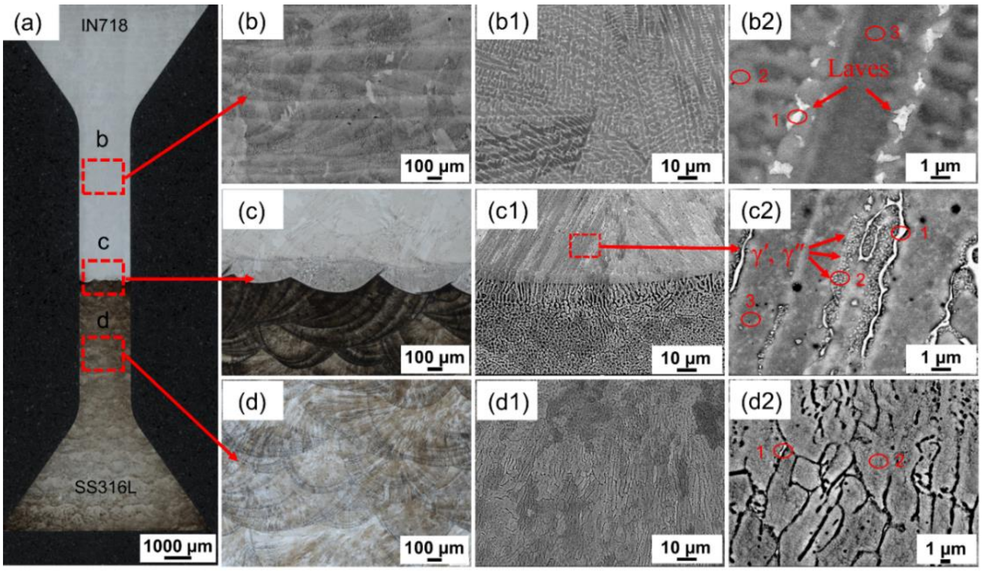

Figure 7-4 Microstructure of heat-treated LDED gradient sample: (a) optical micrographs of overview of etched graded sample for mechanical testing, (b-b2) microstructure of IN718 region at different magnifications, (c-c2) interface between IN718 and SS316L at different magnifications, and (d-d2) SS316L region at different magnifications, respectively.

For example, Figure 7-4(a-d) highlight the presence of overlapping melt pools within a distinct grain structure, a feature aligning with findings from other LDED studies [107, 156, 157]. Additionally, an equiaxed to columnar transition, is evident near the interface where SS316L shifts to IN718, as shown in Figure 7-4(c1). This transition, commonly occurring at the boundary between two different materials during solidification [34, 43], relates to the changes in the temperature gradient G and the liquid-solid interface velocity [158, 159]. It tends to induce stress concentration at interfaces and increases defect susceptibility due to varied solidification rates from the interplay of two materials under intense laser exposure [40, 41].

Comparing the microstructures before and after heat treatment, the most notable change is the presence of γ'/γ'' precipitates near the Laves phase in the IN718 zone adjacent to the interface, as illustrated in Figure 7-4(c2). In the AD state, significant secondary phases (Laves phase) were found along grain boundaries and in interdendritic areas of the IN718-rich region, similar to what is shown in Figure 7-4 (b1-2). In contrast, delta phases were observed along SS316L grain boundaries, coexisting with the austenite matrix in Figure 7.4(d2). The AD condition lacked the strengthening γ'/γ'' precipitates, along with earlier reports [46, 75]. However, the double aging heat treatment leads to the dissolution of Laves phases and the formation of primary strengthening γ'/γ'' phases near the Laves phase region. This is likely due to the Nb-rich Laves phase, which is essential for the formation of γ'/γ'' phases, thereby facilitating precipitation in this area. EDS point analysis has confirmed the phases in the heat-treated sample, with elemental compositions detailed in Table 7-1.

Table 7-1 Representative elements composition of phases and matrix in the HT-FGMs sample by SEM-EDS analysis from different regions (wt. %).

Region	**Spot**	**Al**	**Nb**	**Mo**	**Ti**	**Cr**	**Fe**	**Ni**	**Si**	**Mn**
IN718 (b2)	1	0.9	13.25	3.28	1.51	18.51	16.29	45.94	0.32	
	2	1.01	7.71	2.64	1.28	19.53	18.00	49.83		
	3	1.08	2.61	2.18	0.89	21.56	21.19	50.50		
Interface (c2)	1	1.18	3.7	3.15		18.83	49.62	22.19	1.32	
	2	0.68	2.09	2.62	0.55	19.40	49.9	22.75	0.88	1.14
	3	0.45	0.54	1.73	0.35	19.07	55.25	22.17	0.44	
SS316L (d2)	1			2.82		20.83	66.4	7.45	1.24	1.26
	2			1.65		18.26	67.25	10.55	0.91	1.39

7.3.2 Tensile properties at ambient and elevated temperature

Figure 7-5 displays representative engineering stress-strain curves for all of the specimens before (a) and after heat treatment (b), respectively. In the AD condition as shown in Figure

7-5(a), FGMs with the YZX orientation exhibit tensile strength that falls between those of individual SS316L and IN718 specimens with identical orientation. In contrast, FGMs in the ZYX orientation show tensile properties similar to those of the individual SS316L-ZYX specimen, not displaying the intermediate tensile strength observed in YZX-oriented FGMs. Additionally, the AD condition reveals anisotropic tensile properties in both the individual materials and their combinations. This anisotropy is characterized by increased strength but reduced ductility in directions perpendicular to the building direction, compared to those parallel to it. As shown in Figure 7-5(b), heat treatment significantly enhances the strength of both IN718 and YZX-oriented FGMs, distinguishing these specimens in terms of strength from their ZYX counterparts. This improvement highlights the influence of heat treatment on mechanical properties, particularly by amplifying the differences due to interface orientation.

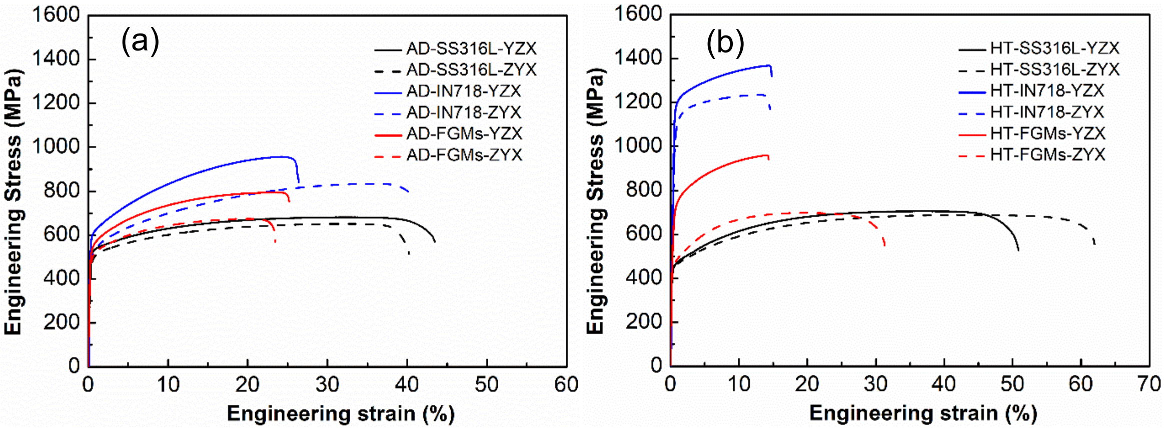

Figure 7-5 Engineering stress-strain curves for all the gradient LDED samples and individual materials at different orientations and conditions. (a) AD and (b) HT.

A straightforward observation of fractures in Figure 7-6 shows the relationship between the fracture mode, interface orientation and heat treatment. Compared to heat treatment, interface orientation predominately influences fracture behavior. FGMs-YZX specimens typically experience crack initiation in one material region (likely the IN718 area) and propagate through the other material, resulting in fractures perpendicular to the loading direction. In contrast, FGMs-ZYX specimens primarily exhibit fracture initiating and propagating within the SS316L region, with the majority of stain localized to this area, and minimal strain observed in the IN718 region. Crack propagation paths remain perpendicular to the loading direction in both orientations. Further analysis using DIC will explore the distinct effects of interface orientation and heat treatment on fracture modes in the discussion part.

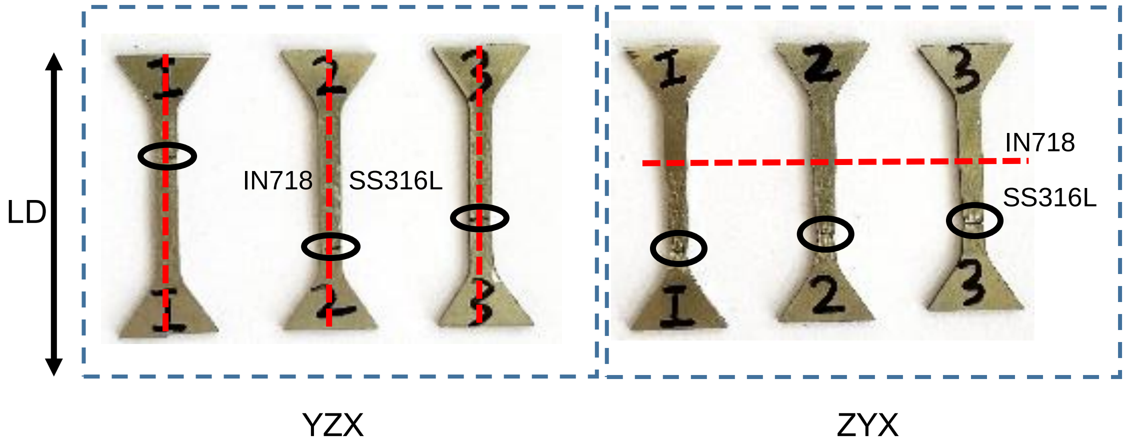

Figure 7-6 Relationship between fracture mode and interface orientation for FGMs through LDED after HT. The red dashed lines represent the interface between the individual SS316L and IN718 materials. The black circles marked on the fractured tensile sample display the fracture locations for each tested condition. LD presents the loading direction.

Figure 7-7 and Table 7-2 presents a detailed overview of the tensile properties: OYS, UTS, UE, and EL. Before HT, the FGMs-YZX specimens have a UTS of approximately 793 ± 3 MPa, situated between the UTS of SS316L (681 ± 0.3 MPa) and IN718 (952 ± 5 MPa) from the same graded block. In contrast, the FGMs-ZYX specimens demonstrate UTS values closer to SS316L specimens, averaging 668 ± 16 MPa, compared to 647 ± 4 MPa for SS316L. Post-HT, the tensile strength of IN718 notably improves due to the emergence of a strengthening phase. For instance, OYS values for IN718 increase from 591 MPa to 1171 MPa in the YZX orientation and from 488 MPa to 1049 MPa in the ZYX orientation. Conversely, the OYS value of SS316L diminishes after heat treatment, while its UTS increases across both orientations. This change is linked to various metallurgical factors, such as reduction in dislocation density, diffusion of segregated elements at cell boundaries, and disappearance of dislocation cell structure when the heat treatment temperature of LDED SS316L exceeds 600 °C [85].

As a result, FGMs-YZX specimens, which merge the strengths of both SS316L and IN718, exhibit enhanced tensile strength after HT. These specimens exhibit OYS and UTS values of 671 ± 38 MPa and 973 ± 27 MPa, respectively, representing a 26% increase in OYS and a 23% rise in UTS compared to their AD state. In contrast, the heat-treated FGMs-ZYX specimens display a drop in OYS and a minor increase in UTS, mirroring the pattern observed in the tensile properties of heat-treated SS316Lsamples. This suggests that only FGM specimens with an interface perpendicular to the loading direction effectively exploit the benefits of the gradient material when combining SS316L and IN718 with a sharp interface. However, FGM specimens with an interface parallel to the loading direction tend to reflect the tensile properties of the comparatively weaker SS316L material.

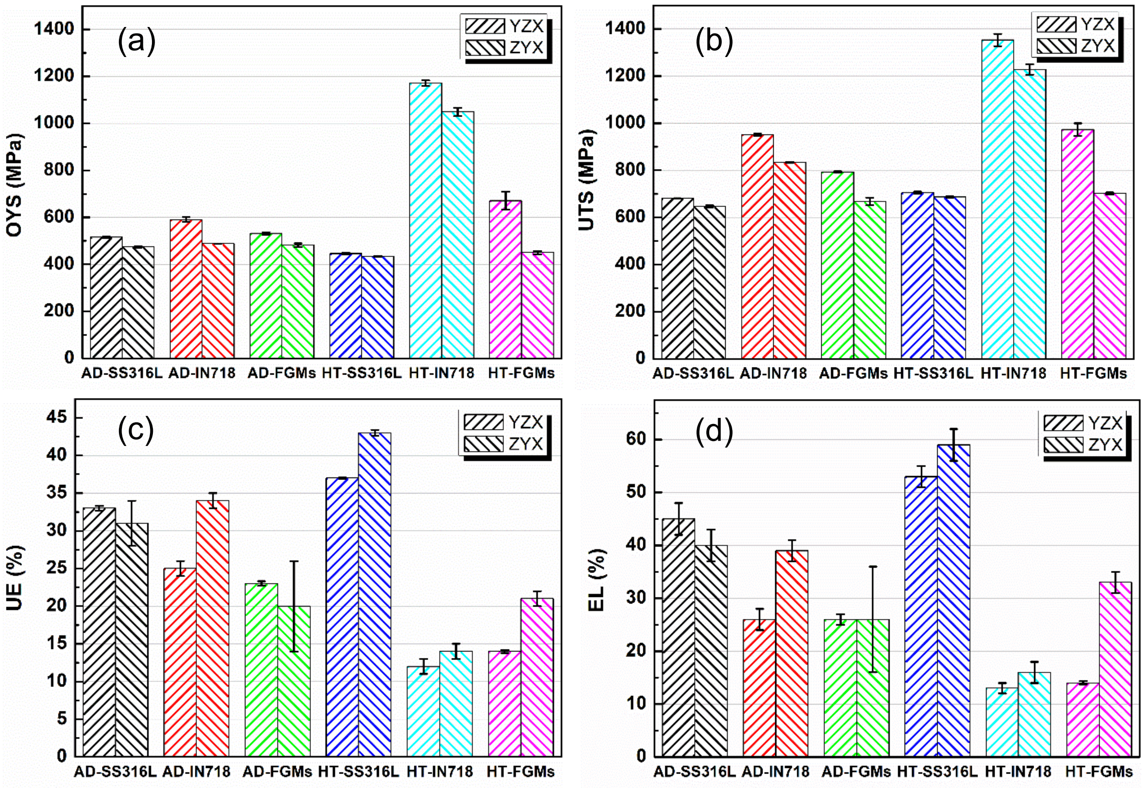

Figure 7-7 Summary of tensile properties at room temperature: (a) OYS, (b) UTS, (c) UE and (d) EL.

Table 7-2 Summary of tensile properties of gradient LDED specimens processed at different conditions.

Specimen	**Condition**	**Test temperature °C**	**OYS MPa**	**UTS MPa**	**UE %**	**EL %**
AD-SS316L-YZX	AD	RT	516 ± 4	681 ± 0.3	33 ± 0.3	45 ± 3
AD-SS316L-ZYX	AD	RT	475 ± 3	647 ± 4	31 ± 2	41 ± 2
AD-IN718-YZX	AD	RT	591 ± 10	952 ± 5	25 ± 1	27 ± 1
AD-IN718-ZYX	AD	RT	488 ± 0.3	833 ± 2	34 ± 1	39 ± 1
AD-FGMs-YZX	AD	RT	532 ± 5	793 ± 3	23 ± 1	26 ± 1
AD-FGMs-ZYX	AD	RT	482 ± 8	668 ± 16	20 ± 6	26 ± 10
HT-SS316L-YZX	HT	RT	446 ± 4	705 ± 4	37 ± 1	53 ± 2

Table 7-3 (continued): Summary of tensile properties of gradient LDED specimens processed at different conditions

HT-SS316L-ZYX	HT	RT	435 ± 2	687 ± 2	43 ± 1	59 ± 3
HT-IN718-YZX	HT	RT	1171 ± 12	1353 ± 26	12 ± 1	13 ± 1
HT-IN718-ZYX	HT	RT	1049 ± 18	1228 ± 22	14 ± 1	16 ± 2
HT-FGMs-YZX	HT	RT	671 ± 38	973 ± 27	14 ± 1	14 ± 1
HT-FGMs-ZYX	HT	RT	450 ± 7	702 ± 4	21 ± 1	33 ± 2
AD-SS316L-YZX	AD	650	329 ± 5	415 ± 3	13 ± 1	27 ± 1
AD-SS316L-ZYX	AD	650	315 ± 5	396 ± 1	16 ± 1	31 ± 2
AD-FGMs-YZX	AD	650	385 ± 9	560 ± 8	17 ± 1	20 ± 1
AD-FGMs-ZYX	AD	650	320 ± 2	363 ± 1	6 ± 1	23 ± 1
HT-SS316-YZX	HT	650	251 ± 6	397 ± 4	20 ± 1	33 ± 1
HT-SS316L-ZYX	HT	650	250 ± 1	386 ± 1	22 ± 1	41 ± 1
HT-FGMs-YZX	HT	650	544 ± 2	730 ± 6	9 ± 1	12 ± 2
HT-FGMs-ZYX	HT	650	276 ± 7	395 ± 3	11 ± 4	20 ± 3

7.3.3 Creep properties

Figure 7-8(a) presents the tensile engineering stress-strain curves obtained at 650 °C. Consistent with prior research [89], creep tests were conducted at the same temperature of 650 °C and a stress of 225 MPa, which is below the yield strength of all gradient specimen before and after HT. Figure 7-8(b) displays the creep strain-time graphs for the gradient LDED samples evaluated under the same conditions. Notably, similar to tensile outcomes at ambient temperature, only the gradient YZX specimen, with its interface orientation aligned with the loading direction, demonstrates a significant improvement in elevated temperature OYS, UTS, and t_r following heat treatment. On the contrary, the ZYX gradient specimen, with its interface orientation perpendicular to the loading direction, demonstrates a reduction in elevated temperature OYS but an increase in UTS after heat treatment. This results in a pronounced anisotropy in the elevated temperature tensile properties post-heat treatment among FGM specimens with varying orientations.

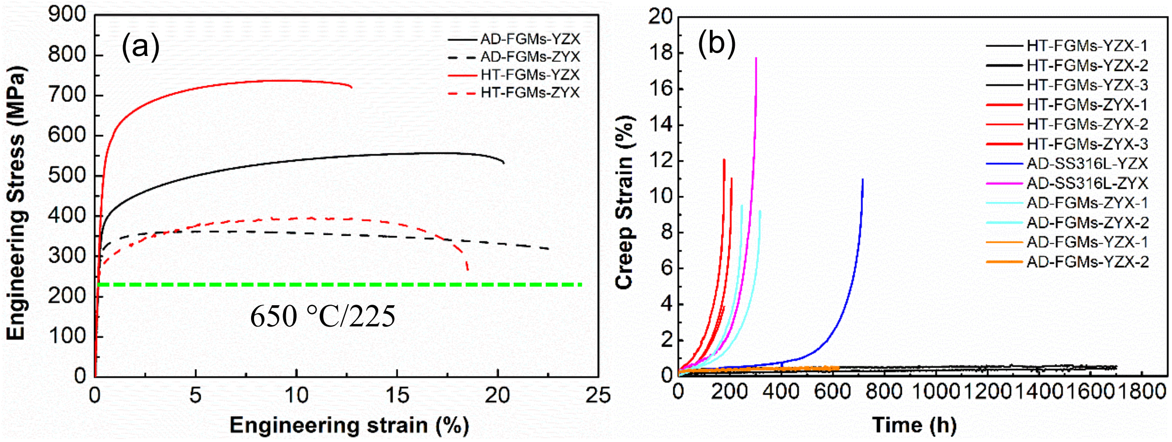

Figure 7-8 (a) Elevated temperature tensile stress-strain curves and (b) Creep strain-time curves for all LDED samples tested at 650 °C and 225 MPa.

This enhanced anisotropy is also evident in the creep behavior, as depicted in Figure 7-8(b). Specifically, the heat-treated FGMs ZYX specimen exhibits an average creep rupture lifespan of 187 hours, mirroring the performance of the standalone SS316L produced via LDED as reported in the previous study [90]. In comparison, the heat-treated FGMs YZX sample achieves an impressive creep lifespan exceeding 1700 hours. More details of creep results can be found in Table 7-4.

Table 7-4 Summary results of creep properties: t_r, $\dot{\varepsilon}_s$, and ε_f for all of the tested cases.

	AD-FGMs-YZX	AD-FGMs-ZYX	HT-FGMs-YZX	HT-FGMs-ZYX
t_r /h	> 623	188 ± 166	> 1701	187 ± 16
$\dot{\varepsilon}_s$ x p10^{-7} / s^{-1}	1.1 ± 1	12 ± 11	0.4 ± 0.1	34.8 ± 11.8
ε_f /%	> 1	6 ± 6	> 1	9 ± 24

7.4 Discussions

In this section, a crack-free functionally graded component was successfully fabricated through the LDED process by depositing IN718 atop SS316L materials. This achievement involved varying the laser power in accordance with the compositional regions. A sharp interface between the two materials was established following the FGMs classification. In the AD condition, there is a confined transition region between IN718 and SS316L. Notably, variations in elemental diffusion rates are observed between the IN718-rich region and SS316L-rich regions near this interface, as underscored in my prior work [160]. IN718 possesses higher concentrations of elements such as Ni, Nb, Cr, and Ti compared to SS316L, leading to a tendency for these elements to equilibrate their concentrations, potentially diffusing towards SS316L. After heat treatment, the microstructure reveals intriguing characteristics. A more pronounced, gradual change in the chemical composition is discernible in the IN718-rich region near the interface, contrasting with the AD condition. This suggests that heat treatment can induce a graduated composition, even with sharp deposition interfaces.

The presence of γ'/γ'' phase precipitations indicates that such gradual compositions are likely influenced by phase transformations during the aging process. Ji et al. [51] extensively explored the influence of aging precipitation on the microstructure and hardness of FGMs SS316L/IN718. Their work highlighted the increased hardness near IN718, which is facilitated by the dissolution of the Laves phase and the subsequent precipitation of primary γ'/γ'' phases. It is noteworthy that despite this elemental redistribution at the interface, the grain structure remains consistent pre and post heat-treatment.

Conversely, within the SS316L domain, while the elemental compositions remain relatively stable, there is a significant shift in grain structure near the interface. Given that the peak heat treatment temperature of 720 °C exceeds the recrystallization threshold of SS316L (700-750 °C), both recrystallization and grain refinement are observed. Additionally, GROD maps reveal substantial deformation and energy absorption in SS316L grains, likely a result of the increased thermal cycles and energy input in this region. Such elevated energy acts as a driving force for grain refinement during heat treatment, potentially enhancing strength, reducing anisotropy, and improving crack resistance [161–163]. Thereby, the employed heat treatment fulfills a dual purpose: it not only effectively balances the elemental distribution, particularly through the precipitation of γ'/γ'' phases in the IN718-rich region, but also refines the grain structure in the SS316L zone. This grain refinement is further aided by the high energy accumulated from the repetitive thermal cycles inherent to the LDED process.

The mechanical behavior of FGMs at various temperatures and sample orientations relative to the interface was examined. Tensile properties at room temperature, assessed using the DIC technique, reflected the mechanical evolution observed at higher temperatures. Figure 7-9 illustrates the local strain distribution of FGMs before and after heat treatment. For each condition, spatial variations in local major strain are shown at selected stages during the tensile test. These stages are highlighted in the typical tensile curve inset, shown in Figure 7-9(a), corresponding to critical deformation stages: 1 near the yield point, 2 within uniform elongation, 3 approaching the ultimate tensile strength, and 4 immediately before fracture. Local strain maps just before fracture (point 4) are depicted for both ZYX-oriented sample and the initiation of a crack (4) for YZX-oriented sample is also depicted here. A dash black line in ZYX-oriented sample presents the section along the specimen body from which the local strain data is extracted. In the YZX-oriented sample, local strain was examined from both IN718 (dash black line) and SS316L (solid black line) region.

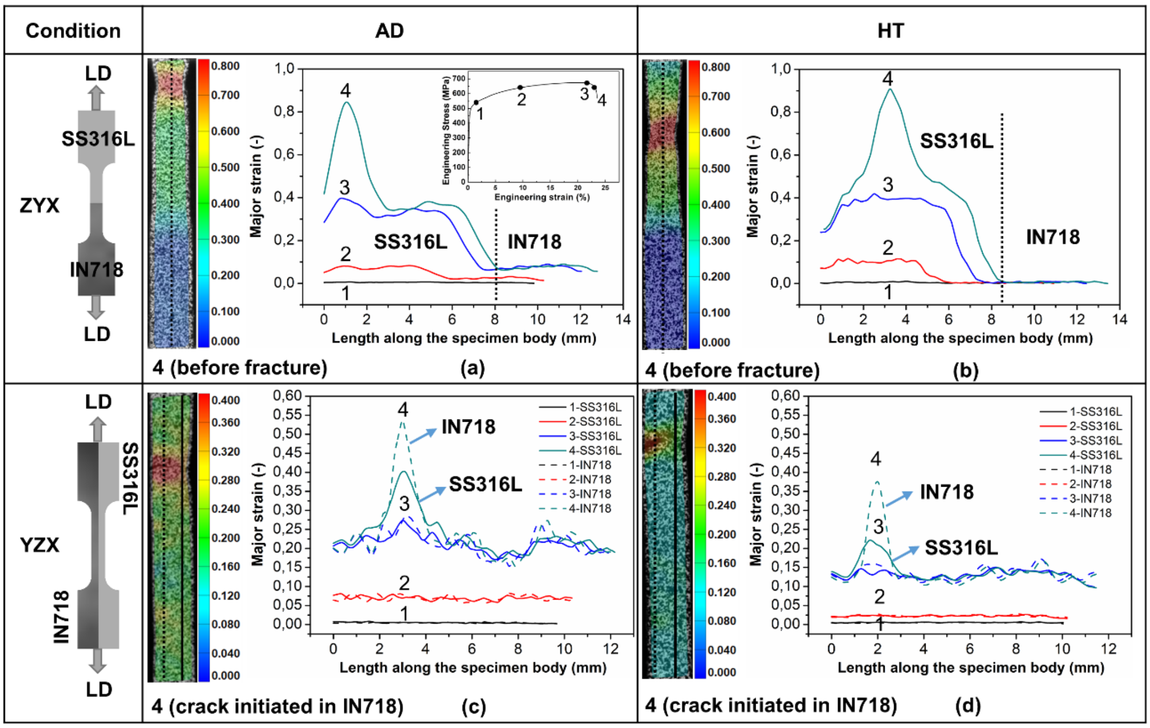

Figure 7-9 Evolution of local strain distribution of FGMs specimens before (a) (c) and after heat treatment (b) (d).

For the ZYX-oriented specimen in the AD condition, significant strain is primarily observed in the SS316L region with minor strain in IN718, as illustrated in Figure 7-9(a). The strain in SS316L intensifies before breaking as evident in the AD-ZYX strain map. In contrast, post-heat treatment, the strength of the IN718 region rises, limiting plastic deformation to the SS316L region only, as seen in Figure 7-9(b). This heat treatment enhances the ductility of SS316L and reduces its yield strength, leading to increased strain in the heat-treated ZYX specimen compared to the AD condition. Figure 7-9(b) shows an uneven strain distribution during tension in the AD state (curve 2), which becomes more uniform post-treatment, likely due to elemental diffusion.

For the YZX-oriented specimen, both materials deform uniformly until the ultimate tensile strength is achieved, as illustrated in Figure 7-9(c). At this stage, IN718 experiences higher strain than SS316L, leading to crack initiation in IN718. The strength of the gradient material primarily relies on the harder IN718, while its ductility benefits from the softer materials. After heat treatment, IN718 becomes harder and SS316L softer, resulting in increased strength but reduced strain, a comparison between Figure 7-9(d) and (c). In the HT-YZX sample, cracks start in IN718 and propagate through SS316L. The distinct grain structures between these materials help slow down the crack progression, enhancing crack resistance. Additionally, the HT condition demonstrates a more balanced deformation across both materials before cracking occurs.

Deformation variations across different sample orientations contribute to anisotropy, which is further influenced by microstructural changes from heat treatment. This anisotropy is quantified by comparing the yield strength ratios of ZYX and YZX orientations before and after treatment, as detailed in Table 7-5. Heat treatment tends to homogenize the composition of both IN718 and SS316L and results in finer grains. However, it also amplifies mechanical property differences between orientations due to their distinct responses to heat treatment. Specially, the heat treatment, while beneficial for the precipitation process in IN718, may adversely affect SS316L. Consequently, post-heat treatment, IN718 becomes stronger, and SS316L weaker, thereby, intensifying the anisotropy: ZYX orientation is influenced more by the softer SS316L, while YZX orientation reflects the characteristics of the harder IN718.

Table 7-5 Effect of heat treatment on the anisotropy of graded LDED-FGMs SS316-IN718 sample assessed in terms of ratio of yield strength before and after HT.

Region	**Anisotropy/%**		
	AD	**HT**	**Increase by**
IN718	83%	90%	8%
FGMs	91%	67%	-26%
SS316L	92%	98%	6%

7.5 Summary

This chapter presents a comprehensive analysis of the mechanical properties at room and high temperature of gradient samples that combine SS316L and IN718 using LDED. The study investigates the impact of interface orientation and heat treatment on microstructure and mechanical behavior, elucidating fracture behavior through DIC analysis.

It was discovered that heat treatment promotes elemental diffusion, resulting in smoother compositional transitions, particularly in the IN718-rich region near the interface. This finding highlights the potential to achieve gradual compositional shifts, even with sharply defined deposition interfaces, thereby simplifying the optimization of parameters. Near the interface, the SS316L region undergoes recrystallization and grain refinement after heat treatment, whereas the IN718 region remains mostly unchanged.

The influence of heat treatment on mechanical properties significantly depends on the interface orientation relative to the loading direction. Gradient samples oriented in the YZX direction exhibit the strengths of both materials. After heat treatment, these samples demonstrate enhanced mechanical properties, with an OYS of 671 MPa, UTS of 973 MPa, and 14% elongation at room temperature. Additionally, these samples show exceptional creep resistance, enduring over 1700 hours. In contrast, ZYX-oriented gradient samples primarily reflect the properties of the less robust SS316L, leading to a stress concentration effect, with an OYS of 450 MPa and a creep lifespan of roughly 180 hours following heat treatment. The differential enhancement of strength between the materials amplifies the observed anisotropy.

DIC analysis uncovers strain concentration in the SS316L region for ZYX-oriented samples under both AD and HT conditions. Interestingly, fractures consistently occur within the SS316L region, not at the interface. In YZX-oriented samples, deformation remains uniform until the ultimate tensile strength is reached, followed by strain peaks in the IN718 area. This initiates crack formation, which propagates through the SS316L area, leading to ultimate failure. This pattern of fracture remains consistent both before and after heat treatment.

8 Integrative summary of research findings

The ambition of this dissertation was to advance the understanding of high-temperature mechanical properties and to pioneer the development of high-quality FGMs composed of SS316L and IN718 using LDED. This journey was guided by a series of specific objectives, each addressing critical aspects of the fabrication process, post-processing heat treatment, material characterization, and mechanical performance evaluation. This chapter synthesizes the methodological progression and key findings from each investigative phase, demonstrating their collective contribution towards realizing the dissertation's primary goal.

The exploration began with an in-depth analysis of how LDED process parameters, notably laser beam size and power, affect the microstructure and mechanical performance of SS316L and IN718 fabricated by LDED (**Chapter 4**). In this part, two printing modules, SDM800 and SDM1600, each with its set of optimal parameters including laser power, hatch distance, layer thickness and powder feed rate, were selected to assess the impact these variables have on mechanical outcomes. The study highlighted the significance of increasing both the laser beam size and laser power as a strategy to improve the build rate during the additive manufacturing process. This approach has garnered industrial interest due to its potential to improve productivity, reduce costs, and enhance operational efficiency. The findings indicated that employing a laser beam size twice as large, along with optimized process parameters, could increase the build rate by 78%. This enhancement led to a notable reduction in powder consumption per print by 58%, effectively increasing powder usage efficiency by 132%.

Additionally, reducing the laser beam diameter while increasing laser power was found to decrease porosity, thereby improving the materials' high-temperature mechanical properties. Porosity levels were reduced to as low as 0.01% in SDM800 and to 0.2% in SDM1600. Nonetheless, porosity remained below 1% for all specimens, indicating that the LDED process produced nearly fully dense parts under the studied parameters. An increase in the laser beam size from 800 to 1600 μm led to slower cooling rates, resulting in larger grains and a more uniform microstructure. These microstructural changes contributed to slightly lower but more uniform tensile and creep properties. Despite variations in tensile properties, specimens produced under both conditions demonstrated superior tensile properties and creep resistance compared to those manufactured through conventional processes. This investigation not only identified the optimal parameters (SDM800) for each material but also established a foundational knowledge for their integration into FGMs.

Further investigation delved into the impact of heat treatment on the mechanical behavior of SS316L and IN718 (**Chapters 5 and 6**). Post-processing heat treatment is of great importance for FGMs composed of SS316L and IN718, particularly for IN718 due to the requirement to fully realize its mechanical strength. However, the optimal temperature of heat treatment for AM-IN718 often surpass those suitable for AM-SS316L material, potentially leading to thermal instability and adverse impacts on mechanical properties of AM-SS316L. Therefore, identifying the optimal heat treatment protocols for both LDED-SS316L and LDED-IN718 is essential. This process involves a detailed examination of effects of heat treatment on their microstructure and high-temperature mechanical performance, aiming to establish an optimal heat treatment strategy that accommodates the unique requirements of each material within FGMs.

Chapter 5 analyzed the creep behavior of LDED-SS316L under a range of annealing temperatures from 300 °C to 1200 °C. The findings indicated that 600 °C serves as a critical threshold for thermal stability in LDED SS316L, aligning with outcomes observed in LPBF-SS316L. Above 600 °C, there was a noticeable reduction in creep life and an increase in creep rate, attributed to the gradual loss of the dislocation structure formed during LDED.

Chapter 6 examined the microstructure and creep property responses of LDED-IN718 to various heat treatments, including homogenization, solution, and aging processes. This study demonstrated that creep behavior is highly temperature-dependent, with higher homogenization temperatures facilitating the dissolution of the Laves phase. Solution treatments at approximately 980 °C were crucial for delta phase formation, while the subsequent double aging process led to the emergence of strengthening precipitates. Moreover, employing high-temperature heat treatments effectively mitigated the anisotropic creep properties. Through the application of multiple heat treatment steps, the influence of microstructural features—such as grain size, precipitate phases, dislocations, and texture—on creep behavior was elucidated. The findings emphasized the importance of the aging process in enhancing the mechanical properties of LDED-IN718. Although additional solution and homogenization at elevated temperatures are beneficial for removing unwanted phases and encouraging the precipitation of strengthening phases γ'/γ'', an increase in heat treatment temperature was found to adversely affect creep properties. Microstructural analysis further revealed the significant role of dislocation structures, beyond the strengthening phases γ'/γ'', in mechanical performance of LDED-IN718.

Within the experimental scope and process parameters studied, a double aging treatment peaking at 720 °C is identified as the optimal protocol for LDED-IN718, while annealing below 600 °C is determined best for LDED-SS316L. These findings are crucial for developing post-processing treatments that align the mechanical properties of these materials, thus enhancing the performance of FGMs. Consequently, this narrows down the heat treatment range for their combination. Furthermore, the determination of an optimal heat treatment regime—double aging at 720 °C for 8 hours followed by cooling at 50 °C per hour, plus annealing at 620 °C for 8 hours and air cooling—was established for the finalized FGMs after assessing the hardness of SS316L/IN718 specimens across various thermal treatments.

Transitioning to the integration of individual materials, **Chapter 7** concludes the research by examining the high-temperature mechanical behavior of LDED FGMs SS316L/IN718. A distinct interface was engineered by layering IN718 powder over SS316L, offering technological advantages by simplifying process parameter optimization during printing and post-heat treatments. This approach elucidates the enhancement of high-temperature mechanical properties post-heat treatment, displaying a crack-free interface and improved elemental diffusion. The study also explored the orientation of the interface in relation to the loading direction, identifying its significant impact on mechanical performance. FGM specimens with interfaces aligned with the load direction mirrored the properties of SS316L, the weaker material. Conversely, specimens with interfaces perpendicular to the build direction displayed markedly better mechanical properties, situating them between those of pure IN718 and SS316L. Fracture analysis further emphasized the importance of interface orientation, with cracks initiating and propagating in material-specific regions depending on the orientation.

This study provides crucial insights into the development and optimization of dissimilar and FGMs comprising SS316L and IN718, tailored for enhanced mechanical performance. These findings lay the groundwork for significant advancements in critical sectors such as aerospace and automotive. Future research should focus on refining deposition techniques and post-heat treatment processes to broaden the applicability of FGMs, ensuring that their mechanical properties meet the specific needs of various industries. These efforts are anticipated to broaden the use of FGMs across engineering fields where durability and high performance are essential.

9 Conclusion

This dissertation investigates the field of FGMs SS316L/IN718, focusing on their potential in high-temperature applications. Through a systematic and comprehensive approach, significant strides have been made in understanding the mechanical behavior of these materials under thermal and extreme conditions. The research was conducted in two interconnected phases: first, assessing the high-temperature properties of the individual materials and then applying this knowledge to fabricate and analyze robust FGM components.

9.1 Overview of research achivements

(1) **Effect of process parameters on mechanical behavior of SS316L and IN718**: The exploration revealed that adjusting process parameters such as laser beam size and laser power can tailor the microstructure, thereby influencing mechanical performance. A smaller laser beam diameter combined with higher laser power results in LDED materials exhibiting minimal porosity and enhanced high-temperature mechanical performance. Furthermore, the sample orientation with respect to the deposition direction significantly influences mechanical behavior, with different orientations leading to varied outcomes. In contrast, using a larger laser beam with lower laser power tends to promote a uniform microstructure, with diminishes the impact of sample orientation on mechanical properties.

(2) **Effect of heat treatment on mechanical behavior of SS316L and IN718**: SS316L and IN718 exhibited different responses to heat treatments. The high-temperature mechanical behavior of SS316L was predominantly influenced by dislocation structures and elemental micro-segregations. Heat treatments above 600 °C promoted the diffusion of elemental micro-segregations at cell boundaries and dissolved the cell substructure, resulting in a notable decrease in high-temperature resistance. Conversely, IN718 showed improvements in creep resistance, attributed to columnar grain structures and precipitates. Particularly, LDED IN718, which underwent a straightforward double aging process, displayed superior high-temperature mechanical properties. These insights are crucial when considering post-process treatments to optimize the mechanical properties of the combined IN718 and SS316L using LDED.

(3) **High-temperature mechanical behavior of LDED FGMs SS316L/IN718**: Creating a crack-free interface between SS316L and IN718 was achievable using LDED. Heat treatment facilitated improved elemental diffusion, enabling smoother compositional

transitions even at sharp deposition interfaces. This simplified parameter optimization compared to the deposition of smooth interfaces. However, the orientation of interface relative to the loading direction significantly influenced the mechanical performance and fracture mechanism. A gradient sample, with its interface aligned to the loading direction, leveraged the strengths of both materials, exhibiting exceptional creep resistance and enduring over 1700 hours. In contrast, samples with interfaces perpendicular to the loading direction showed performance similar to that of the weaker material. Therefore, it is crucial to ensure optimal interface orientation to fully exploit the combined strengths of both materials. Notably, irrespective of the sample orientations or their heat-treated states, fractures consistently occurred within the SS316L region, not at the interface.

9.2 Contribution to the Field of Science

(1) The research significantly deepens the understanding of the high-temperature mechanical properties of IN718 and SS316L materials when fabricated through LDED.

(2) This study systematically evaluates and reveals how various process parameters influence the microstructure of IN718 and SS316L. This provides valuable insights into how material behavior can be tailored for specific high-temperature applications.

(3) The dissertation contributes to the scientific knowledge by examining the impact of heat treatment on the microstructural integrity and mechanical performance. This includes both individual materials (IN718 and SS316L) and their composite forms as FGMs.

(4) The findings from this research lay a solid foundation for the design and optimization of FGMs, specifically for high-temperature applications, thereby contributing to the advancement of material engineering practices.

9.3 Contribution to Practice

(1) In practice, the research outcomes provide a roadmap for tailoring process parameters to achieve specific mechanical properties in LDED-manufactured materials. These findings can directly affect manufacturing practices, especially for industries that require materials with precise high-temperature performance.

(2) The practical implications of understanding heat treatment responses are invaluable for material scientists and engineers working to produce high-quality components. The research offers guidelines for applying heat treatments to different materials, ensuring

that the resulting mechanical properties meet the rigorous demands of high-temperature applications.

(3) For industry practitioners, the insights into the behavior of FGMs at elevated temperatures provide a strong foundation for making informed decisions about component design and orientation. This can lead to more efficient and effective use of materials and reduce the need for extensive post-processing.

9.4 Recommendations for Further Research

(1) Future research could explore the long-term stability of these mechanical properties under operational high-temperature conditions, further solidifying the practical applications of this research.

(2) While the study has identified optimal conditions for individual materials, a comprehensive exploration of FGM fabrication under these conditions is crucial. This includes delving into process and post-processing optimizations that might further enhance component quality.

(3) Future work will also consider other promising FGMs, assessing their viability in high-temperature applications and their potential for quality component construction.

In conclusion, this dissertation represents a significant advancement in the understanding and application of FGMs SS316L/IN718, particularly in high-temperature environments. The findings lay the groundwork for future innovations in material science and manufacturing, paving the way for the development of materials that are not only more efficient but also tailored to withstand the rigors of high-performance industries. This research, therefore, stands as a testament to the power of meticulous investigation and innovation in overcoming material challenges, heralding a new era in the field of advanced manufacturing and material science.

10 Závěr

Tato disertační práce zkoumala oblast FGM SS316L/IN718 se zaměřením na jejich potenciál pro vysokoteplotní aplikace. Díky systematickému a komplexnímu přístupu bylo dosaženo významného pokroku v pochopení chování těchto materiálů za extrémních podmínek. Výzkum byl rozdělen do dvou odlišných, avšak vzájemně propojených fází: pochopení vysokoteplotních vlastností jednotlivých materiálů a následná aplikace těchto znalostí při výrobě a analýze robustní FGM součásti.

10.1 Shrnutí výsledků výzkumu

(1) Vliv procesních parametrů na mechanické chování jednotlivých materiálů SS316L a IN718: V rámci experimentálního programu bylo odhaleno, že úpravou depozičních parametrů, jako jsou velikost laserového paprsku a výkon laseru, lze modifikovat vlastnosti mikrostruktury, a tím ovlivnit mechanické vlastnosti. Menší průměr laserového svazku doplněný vyšším výkonem laseru vytváří materiály s minimální pórovitostí a lepšími mechanickými vlastnostmi při vysokých teplotách. Kromě toho hraje významnou roli orientace vzorku vzhledem ke směru depozice. Byl prokázán významný vliv orientace zkušebních těles na výsledné mechanické vlastnosti. Naopak větší laserový paprsek vyvážený nižším výkonem laseru podporuje rovnoměrnou mikrostrukturu a snižuje anizotropii materiálu.

(2) Vliv tepelného zpracování na mechanické chování jednotlivých vzorků IN718 a SS316L: Jak IN718, tak SS316L vykazovaly rozdílné reakce na tepelné zpracování. U IN718 bylo pozorováno zlepšení odolnosti proti tečení na základě struktury zrn a precipitátů; IN718, který prošel přímým procesem dvojího stárnutí, vykazoval zlepšené mechanické vlastnosti při vysokých teplotách. Naproti tomu vysokoteplotní mechanické chování SS316L bylo převážně ovlivněno dislokačními strukturami a mikrosegregací prvků. Teploty tepelného zpracování vyšší než 600 °C podporují mikro segregaci prvků na hranicích buněk a rozpouštějí buněčnou substrukturu, což vede k výraznému snížení odolnosti vůči vysokým teplotám. Tyto poznatky mají zásadní význam při úvahách o následném zpracování pro dosažení požadovaných mechanických vlastností kombinovaných materiálů IN718 a SS316L pomocí LDED.

(3) Chování LDED FGM SS316L/IN718 při vysokých teplotách: Technologie LDED umožnila vytvoření rozhraní mezi SS316L a IN718 bez trhlin. Tepelné zpracování podpořilo difúzi prvků, čímž bylo dosaženo hladších přechodů chemického složení i pro ostrá rozhraní, takže optimalizace parametrů byla jednodušší než u depozice hladkých rozhraní. Nicméně

orientace rozhraní vzhledem ke směru zatížení drasticky ovlivnila mechanické výsledky a lomové mechanismy. Vzorek s gradientem, jehož rozhraní je orientováno ke směru zatížení, využívá pevnosti obou materiálů a vykazuje výjimečnou odolnost proti tečení: vydrží více než 1700 hodin. Naproti tomu vzorky s rozhraním kolmým ke směru zatížení se chovají podobně jako slabší materiál. Pro plné využití pevností obou materiálů je zásadní zajistit vhodnou orientaci. Bez ohledu na orientaci vzorků nebo stavy tepelného zpracování docházelo k lomům důsledně v oblasti SS316L, nikoliv na rozhraní.

10.2 Přínos pro vědní obor

(1) Výzkum významně prohlubuje znalosti o vysokoteplotních mechanických vlastnostech materiálů IN718 a SS316L vyrobených pomocí LDED.

(2) Tato studie systematicky vyhodnocuje a odhaluje, jak různé procesní parametry ovlivňují mikrostrukturu IN718 a SS316L. To poskytuje cenné poznatky o tom, jak lze chování materiálu přizpůsobit pro konkrétní vysokoteplotní aplikace.

(3) Disertační práce přispívá k vědeckému diskurzu tím, že zkoumá vliv tepelného zpracování na mikrostrukturní integritu a mechanické vlastnosti. To zahrnuje jak jednotlivé materiály (IN718 a SS316L), tak jejich kompozitní formy jako FGM.

(4) Výsledky tohoto výzkumu poskytují solidní vědecký základ pro navrhování a optimalizaci FGM, konkrétně pro vysokoteplotní aplikace, čímž přispívají k rozvoji postupů materiálového inženýrství.

10.3 Přínos pro praxi

(1) V praxi poskytují výsledky výzkumu plán pro přizpůsobení procesních parametrů k dosažení specifických mechanických vlastností materiálů vyráběných pomocí LDED. Tyto výsledky mohou přímo ovlivnit výrobní postupy, zejména pro průmyslová odvětví, která vyžadují materiály s přesnými vysokoteplotními vlastnostmi.

(2) Praktické důsledky pochopení reakcí při tepelném zpracování jsou neocenitelné pro materiálové vědce a inženýry, kteří pracují na výrobě vysoce kvalitních součástí. Výzkum nabízí pokyny pro aplikaci tepelného zpracování na různé materiály, které zajistí, že výsledné mechanické vlastnosti budou splňovat přísné požadavky vysokoteplotních aplikací.

(3) Pro odborníky z průmyslu poskytují poznatky o chování materiálů FGM při zvýšených teplotách pevný základ pro informované rozhodování o konstrukci a orientaci součástí. To může vést k účinnějšímu a efektivnějšímu využití materiálů a snížit potřebu rozsáhlého následného zpracování.

10.4 Doporučení pro další výzkum

(1) Budoucí výzkum by mohl být zaměřen na zkoumání dlouhodobé stability mechanických vlastností v provozních podmínkách vysokých teplot, což by dále upevnilo praktické aplikace tohoto výzkumu.

(2) Ačkoli studie identifikovala optimální podmínky pro jednotlivé materiály, zásadní je komplexní průzkum výroby FGM za těchto podmínek. To zahrnuje prozkoumání technik následného zpracování, které by mohly dále zvýšit kvalitu součástek.

(3) Tato práce také položila základy pro další výzkum a posouzení životaschopnosti FGM při vysokoteplotních aplikacích a jejich potenciálu pro konstrukci kvalitních součástí. Závěrem lze říci, že tato disertační práce představuje významný pokrok v chápání a použití FGM SS316L/IN718, zejména v prostředí vysokých teplot. Získané poznatky vytvářejí základ pro budoucí inovace v oblasti materiálové vědy a výroby a připravují půdu pro vývoj materiálů, které jsou nejen účinnější, ale také uzpůsobené tak, aby odolávaly náročným podmínkám vysoce výkonných průmyslových odvětví. Tento výzkum je tedy důkazem síly pečlivého zkoumání a inovací při překonávání materiálových výzev a předznamenává novou éru v oblasti pokročilé výroby a materiálové vědy.

11 References

[1] Mahamood RM, Akinlabi ET, Shukla M, Pityana SL (2012) Functionally Graded Material: An overview. In: Proceedings of the World Congress on Engineering 2012 Vol III (WCE 2012). London, UK, pp 4–6

[2] Loh GH, Pei E, Harrison D, Monzón MD (2018) An overview of functionally graded additive manufacturing. Addit Manuf 23:34–44. https://doi.org/10.1016/j.addma.2018.06.023

[3] Reichardt A, Shapiro AA, Otis R, et al (2021) Advances in additive manufacturing of metal-based functionally graded materials. Int Mater Rev 66:1–29. https://doi.org/10.1080/09506608.2019.1709354

[4] Jha DK, Kant T, Singh RK (2013) A critical review of recent research on functionally graded plates. Compos Struct 96:833–849. https://doi.org/10.1016/j.compstruct.2012.09.001

[5] Kumar R, Kumar M, Chohan JS (2021) The role of additive manufacturing for biomedical applications: A critical review. J Manuf Process 64:828–850. https://doi.org/https://doi.org/10.1016/j.jmapro.2021.02.022

[6] Gupta A, Talha M (2015) Recent development in modeling and analysis of functionally graded materials and structures. Prog Aerosp Sci 79:1–14. https://doi.org/10.1016/j.paerosci.2015.07.001

[7] Watanabe Y, Sato R, Kim IS, et al (2005) Functionally graded material fabricated by a centrifugal method from ZK60A magnesium alloy. Mater Trans 46:944–949. https://doi.org/10.2320/matertrans.46.944

[8] Saleh B, Jiang J, Fathi R, et al (2020) 30 Years of functionally graded materials: An overview of manufacturing methods, Applications and Future Challenges. Compos Part B Eng 201:108376. https://doi.org/10.1016/j.compositesb.2020.108376

[9] El-Galy IM, Saleh BI, Ahmed MH (2019) Functionally graded materials classifications and development trends from industrial point of view. SN Appl Sci 1:1–23. https://doi.org/10.1007/s42452-019-1413-4

[10] Ansari M, Jabari E, Toyserkani E (2021) Opportunities and challenges in additive

manufacturing of functionally graded metallic materials via powder-fed laser directed energy deposition: A review. J Mater Process Technol 294:117117. https://doi.org/10.1016/j.jmatprotec.2021.117117

[11] DebRoy T, Wei HL, Zuback JS, et al (2018) Additive manufacturing of metallic components – Process, structure and properties. Prog Mater Sci 92:112–224. https://doi.org/10.1016/j.pmatsci.2017.10.001

[12] Frazier WE (2014) Metal additive manufacturing: A review. J Mater Eng Perform 23:1917–1928. https://doi.org/10.1007/s11665-014-0958-z

[13] Thompson SM, Bian L, Shamsaei N, Yadollahi A (2015) An overview of Direct Laser Deposition for additive manufacturing; Part I: Transport phenomena, modeling and diagnostics. Addit Manuf 8:36–62. https://doi.org/10.1016/j.addma.2015.07.001

[14] Shamsaei N, Yadollahi A, Bian L, Thompson SM (2015) An overview of Direct Laser Deposition for additive manufacturing; Part II: Mechanical behavior, process parameter optimization and control. Addit Manuf 8:12–35. https://doi.org/10.1016/j.addma.2015.07.002

[15] Carroll BE, Palmer TA, Beese AM (2015) Anisotropic tensile behavior of Ti-6Al-4V components fabricated with directed energy deposition additive manufacturing. Acta Mater 87:309–320. https://doi.org/10.1016/j.actamat.2014.12.054

[16] Wang Z, Palmer TA, Beese AM (2016) Effect of processing parameters on microstructure and tensile properties of austenitic stainless steel 304L made by directed energy deposition additive manufacturing. Acta Mater 110:226–235. https://doi.org/10.1016/j.actamat.2016.03.019

[17] Panwisawas C, Tang YT, Reed RC (2020) Metal 3D printing as a disruptive technology for superalloys. Nat Commun 11:1–4. https://doi.org/10.1038/s41467-020-16188-7

[18] Murray SP, Pusch KM, Polonsky AT, et al (2020) A defect-resistant Co–Ni superalloy for 3D printing. Nat Commun 11:1–11. https://doi.org/10.1038/s41467-020-18775-0

[19] Wang YM, Voisin T, McKeown JT, et al (2018) Additively manufactured hierarchical stainless steels with high strength and ductility. Nat Mater 17:63–70. https://doi.org/10.1038/NMAT5021

[20] Mertens A, Reginster S, Contrepois Q, et al (2014) Microstructures and mechanical properties of stainless steel AISI 316L processed by selective laser melting. Mater Sci Forum 783–786:898–903. https://doi.org/10.4028/www.scientific.net/msf.783-786.898

[21] Helmer HE, Körner C, Singer RF (2014) Additive manufacturing of nickel-based superalloy Inconel 718 by selective electron beam melting: Processing window and microstructure. J Mater Res 29:1987–1996. https://doi.org/10.1557/jmr.2014.192

[22] Xu J, Gruber H, Deng D, et al (2019) Short-term creep behavior of an additive manufactured non-weldable Nickel-base superalloy evaluated by slow strain rate testing. Acta Mater 179:142–157. https://doi.org/10.1016/j.actamat.2019.08.034

[23] Strößner J, Terock M, Glatzel U (2015) Mechanical and Microstructural Investigation of Nickel-Based Superalloy IN718 Manufactured by Selective Laser Melting (SLM). Adv Eng Mater 17:1099–1105. https://doi.org/10.1002/adem.201500158

[24] Zhang D, Qiu D, Gibson MA, et al (2019) Additive manufacturing of ultrafine-grained high-strength titanium alloys. Nature 576:91–95. https://doi.org/10.1038/s41586-019-1783-1

[25] Lim JS, Oh WJ, Lee CM, Kim DH (2021) Selection of effective manufacturing conditions for directed energy deposition process using machine learning methods. Sci Rep 11:1–13. https://doi.org/10.1038/s41598-021-03622-z

[26] Ahn DG (2021) Directed Energy Deposition (DED) Process: State of the Art. Int J Precis Eng Manuf Technol 8:703–742. https://doi.org/10.1007/s40684-020-00302-7

[27] Singh A, Kapil S, Das M (2020) A comprehensive review of the methods and mechanisms for powder feedstock handling in directed energy deposition. Addit Manuf 35:101388. https://doi.org/https://doi.org/10.1016/j.addma.2020.101388

[28] Zhang Z, Liu Z, Wu D (2021) Prediction of melt pool temperature in directed energy deposition using machine learning. Addit Manuf 37:101692. https://doi.org/https://doi.org/10.1016/j.addma.2020.101692

[29] Shah K, Haq I ul, Khan A, et al (2014) Parametric study of development of Inconel-steel functionally graded materials by laser direct metal deposition. Mater Des 54:531–538. https://doi.org/10.1016/j.matdes.2013.08.079

[30] Melzer D, Džugan J, Koukolíková M, et al (2021) Structural integrity and mechanical properties of the functionally graded material based on 316L/IN718 processed by DED technology. Mater Sci Eng A 811:141038. https://doi.org/10.1016/j.msea.2021.141038

[31] Liang X, Wu D, Li Q, Jiang L (2010) Laser rapid manufacturing of stainless steel 316L/Inconel718 functionally graded materials: Microstructure evolution and mechanical properties. Int J Opt 2010:1–6. https://doi.org/10.1155/2010/802385

[32] Džugan J, Melzer D, Koukolíková M, et al (2020) Characterization of Functionally Graded Materials Based on Inconel 718 and Stainless Steel 316L Manufactured by DED Process. Struct Integr Addit Manuf Mater Parts 247–256. https://doi.org/10.1520/stp163120190138

[33] Li K, Zhan J, Zhang M, et al (2022) A Functionally Graded Material Design from Stainless Steel to Ni-Based Superalloy by Laser Metal Deposition Coupled with Thermodynamic Prediction. Mater Des 217:110612. https://doi.org/10.2139/ssrn.4016130

[34] Li Z, Kuai Z, Liu B, et al (2023) Selective laser melting of 316L–CuCrZr bimetallic structure via IN718 transition layer. J Mater Res Technol 25:3819–3834. https://doi.org/10.1016/j.jmrt.2023.06.196

[35] Meng W, Zhang W, Zhang W, et al (2019) Additive fabrication of 316L/Inconel625/Ti6Al4V functionally graded materials by laser synchronous preheating. Int J Adv Manuf Technol 104:2525–2538. https://doi.org/10.1007/s00170-019-04061-x

[36] Mei X, Wang X, Peng Y, et al (2019) Interfacial characterization and mechanical properties of 316L stainless steel/inconel 718 manufactured by selective laser melting. Mater Sci Eng A 758:185–191. https://doi.org/10.1016/j.msea.2019.05.011

[37] Dzugan J, Melzer D, Koukolíková M, et al (2020) Characterization of Functionally Graded Materials Based on Inconel 718 and Stainless Steel 316L Manufactured by DED Process. Struct Int Add Manuf Mater Parts 247–256. https://doi.org/10.1520/STP163120190138

[38] Koukolíková M, Simson T, Rzepa S, et al (2022) The influence of laser power on the interfaces of functionally graded materials fabricated by powder-based directed energy

deposition. J Mater Sci 57:13695–13723. https://doi.org/10.1007/s10853-022-07453-9

[39] Halmešová K, Trojanová Z, Koukolíková M, et al (2022) Effect of laser power on thermal properties of multimaterial structure Inconel 718 and stainless steel 316L processed by directed energy deposition. J Alloys Compd 927:167082. https://doi.org/10.1016/j.jallcom.2022.167082

[40] Yang SW, Yoon J, Lee H, Shim DS (2022) Defect of functionally graded material of inconel 718 and STS 316L fabricated by directed energy deposition and its effect on mechanical properties. J Mater Res Technol 17:478–497. https://doi.org/10.1016/j.jmrt.2022.01.029

[41] Kim SH, Lee H, Yeon SM, et al (2021) Selective compositional range exclusion via directed energy deposition to produce a defect-free Inconel 718/SS 316L functionally graded material. Addit Manuf 47:102288. https://doi.org/10.1016/j.addma.2021.102288

[42] Chen B, Su Y, Xie Z, et al (2020) Development and characterization of 316L/Inconel625 functionally graded material fabricated by laser direct metal deposition. Opt Laser Technol 123:105916. https://doi.org/10.1016/j.optlastec.2019.105916

[43] Hinojos A, Mireles J, Reichardt A, et al (2016) Joining of Inconel 718 and 316 Stainless Steel using electron beam melting additive manufacturing technology. Mater Des 94:17–27. https://doi.org/10.1016/j.matdes.2016.01.041

[44] Su Y, Chen B, Tan C, et al (2020) Influence of composition gradient variation on the microstructure and mechanical properties of 316 L/Inconel718 functionally graded material fabricated by laser additive manufacturing. J Mater Process Technol 283:116702. https://doi.org/10.1016/j.jmatprotec.2020.116702

[45] Ghanavati R, Naffakh-Moosavy H, Moradi M (2021) Additive manufacturing of thin-walled SS316L-IN718 functionally graded materials by direct laser metal deposition. J Mater Res Technol 15:2673–2685. https://doi.org/10.1016/j.jmrt.2021.09.061

[46] Li Y, Dlouhý J, Vavřík J, et al (2022) Investigation of short-term creep properties of a coarse-grained Inconel 718 fabricated by directed energy deposition compared to traditional Inconel 718. Mater Sci Eng A 844:143143. https://doi.org/10.1016/j.msea.2022.143143

[47] Li Y, Dlouhý J, Koukolíková M, et al (2022) Effect of deposit thickness on microstructure and mechanical properties at ambient and elevated temperatures for Inconel 718 superalloy fabricated by directed energy deposition. J Alloys Compd 908:164723. https://doi.org/10.1016/j.jallcom.2022.164723

[48] Chlebus E, Gruber K, Kuźnicka B, et al (2015) Effect of heat treatment on the microstructure and mechanical properties of Inconel 718 processed by selective laser melting. Mater Sci Eng A 639:647–655. https://doi.org/10.1016/j.msea.2015.05.035

[49] Deng D, Peng RL, Brodin H, Moverare J (2018) Microstructure and mechanical properties of Inconel 718 produced by selective laser melting: Sample orientation dependence and effects of post heat treatments. Mater Sci Eng A 713:294–306. https://doi.org/10.1016/j.msea.2017.12.043

[50] Popovich VA, Borisov E V., Popovich AA, et al (2017) Impact of heat treatment on mechanical behaviour of Inconel 718 processed with tailored microstructure by selective laser melting. Mater Des 131:12–22. https://doi.org/10.1016/j.matdes.2017.05.065

[51] Ji C, Li K, Zhan J, et al (2023) The effects and utility of homogenization and thermodynamic modeling on microstructure and mechanical properties of SS316/IN718 functionally graded materials fabricated by laser-based directed energy deposition. J Mater Process Technol 319:118084. https://doi.org/10.1016/j.jmatprotec.2023.118084

[52] Lu J, Li W (2023) Improvement of tensile properties of laser directed energy deposited IN718/316L functionally graded material via different heat treatments. Mater Sci Eng A 866:144694. https://doi.org/10.1016/j.msea.2023.144694

[53] Wen Y, Gao J, Narayan RL, et al (2023) Microstructure-property correlations in as-built and heat-treated compositionally graded stainless steel 316L-Inconel 718 alloy fabricated by laser powder bed fusion. Mater Sci Eng A 862:144515. https://doi.org/10.1016/j.msea.2022.144515

[54] Xu G, Wu R, Luo K, Lu J (2022) Effects of heat treatment on hot corrosion behavior of directed energy deposited In718/316L functionally graded material. Corros Sci 197:110068. https://doi.org/10.1016/j.corsci.2021.110068

[55] Melzer D, Koukolíková M, Rzepa S, et al (2023) Influence of interface orientation and surface quality on structural and mechanical properties of SS316L/IN718 block

produced using directed energy deposition. Surfaces and Interfaces 103139. https://doi.org/10.1016/j.surfin.2023.103139

[56] Melzer D, Džugan J, Koukolíková M, et al (2022) Fracture characterisation of vertically build functionally graded 316L stainless steel with Inconel 718 deposited by directed energy deposition process. Virtual Phys Prototyp 1–20. https://doi.org/10.1080/17452759.2022.2073793

[57] R.W. Evans BW (1985) Creep of metals and alloys. The Institute of Metals, London

[58] Rickenbacher L, Etter T, Hövel S, Wegener K (2013) High temperature material properties of IN738LC processed by selective laser melting (SLM) technology. Rapid Prototyp J 19:282–290. https://doi.org/10.1108/13552541311323281

[59] Kuo YL, Nagahari T, Kakehi K (2018) The effect of post-processes on the microstructure and creep properties of Alloy718 built up by selective laser melting. Materials (Basel) 11:996. https://doi.org/10.3390/ma11060996

[60] Wang LY, Zhou ZJ, Li CP, et al (2019) Comparative investigation of small punch creep resistance of Inconel 718 fabricated by selective laser melting. Mater Sci Eng A 745:31–38. https://doi.org/10.1016/j.msea.2018.12.083

[61] Xu Z, Hyde CJ, Tuck C, Clare AT (2018) Creep behaviour of inconel 718 processed by laser powder bed fusion. J Mater Process Technol 256:13–24. https://doi.org/10.1016/j.jmatprotec.2018.01.040

[62] Jeffs S, Lancaster R, Davies S (2017) Effect of build orientation and post processing of a direct laser deposited nickel superalloy as determined by the small punch creep test. Key Eng Mater 734 KEM:128–136. https://doi.org/10.4028/www.scientific.net/KEM.734.128

[63] Danard Y, Lilensten L, Brozek C, et al (2018) Creep and Thermomechanical Fatigue of Functionally Graded Inconel 718 Produced by Additive Manufacturing. In: TMS 2018 147th Annual Meeting & Exhibition. p 961

[64] Davies SJ, Jeffs SP, Coleman MP, Lancaster RJ (2018) Effects of heat treatment on microstructure and creep properties of a laser powder bed fused nickel superalloy. Mater Des 159:39–46. https://doi.org/10.1016/j.matdes.2018.08.039

[65] Kuo YL, Horikawa S, Kakehi K (2017) Effects of build direction and heat treatment on creep properties of Ni-base superalloy built up by additive manufacturing. Scr Mater 129:74–78. https://doi.org/10.1016/j.scriptamat.2016.10.035

[66] Pröbstle M, Neumeier S, Hopfenmüller J, et al (2016) Superior creep strength of a nickel-based superalloy produced by selective laser melting. Mater Sci Eng A 674:299–307. https://doi.org/10.1016/j.msea.2016.07.061

[67] Kunze K, Etter T, Grässlin J, Shklover V (2015) Texture, anisotropy in microstructure and mechanical properties of IN738LC alloy processed by selective laser melting (SLM). Mater Sci Eng A 620:213–222. https://doi.org/10.1016/j.msea.2014.10.003

[68] Xu Z, Murray JW, Hyde CJ, Clare AT (2018) Effect of post processing on the creep performance of laser powder bed fused Inconel 718. Addit Manuf 24:486–497. https://doi.org/10.1016/j.addma.2018.10.027

[69] Wang H, Dhiman A, Ostergaard HE, et al (2019) Nanoindentation based properties of Inconel 718 at elevated temperatures: A comparison of conventional versus additively manufactured samples. Int J Plast 120:380–394. https://doi.org/10.1016/j.ijplas.2019.04.018

[70] McLouth TD, Witkin DB, Bean GE, et al (2020) Variations in ambient and elevated temperature mechanical behavior of IN718 manufactured by selective laser melting via process parameter control. Mater Sci Eng A 780:139184. https://doi.org/10.1016/j.msea.2020.139184

[71] Sanchez S, Hyde CJ, Ashcroft IA, et al (2021) Multi-laser scan strategies for enhancing creep performance in LPBF. Addit Manuf 41:101948. https://doi.org/10.1016/j.addma.2021.101948

[72] Wang LY, Wang YC, Zhou ZJ, et al (2020) Small punch creep performance of heterogeneous microstructure dominated Inconel 718 fabricated by selective laser melting. Mater Des 195:109042. https://doi.org/10.1016/j.matdes.2020.109042

[73] Sanchez S, Gaspard G, Hyde CJ, et al (2021) The creep behaviour of nickel alloy 718 manufactured by laser powder bed fusion. Mater Des 204:109647. https://doi.org/10.1016/j.matdes.2021.109647

[74] Xu Z, Cao L, Zhu Q, et al (2020) Creep property of Inconel 718 superalloy produced by selective laser melting compared to forging. Mater Sci Eng A 794:139947. https://doi.org/10.1016/j.msea.2020.139947

[75] Li Y, Podaný P, Koukolíková M, et al (2023) Effect of Heat Treatment on Creep Deformation and Fracture Properties for a Coarse-Grained Inconel 718 Manufactured by Directed Energy Deposition. Materials (Basel) 16:1–12. https://doi.org/10.3390/ma16041377

[76] Hilal H, Lancaster R, Jeffs S, et al (2019) The influence of process parameters and build orientation on the creep behaviour of a laser powder bed fused ni-based superalloy for aerospace applications. Materials (Basel) 12:1390. https://doi.org/10.3390/ma12091390

[77] Sun SH, Koizumi Y, Kurosu S, et al (2015) Phase and grain size inhomogeneity and their influences on creep behavior of Co-Cr-Mo alloy additive manufactured by electron beam melting. Acta Mater 86:305–318. https://doi.org/10.1016/j.actamat.2014.11.012

[78] Strondl A, Palm M, Gnauk J, Frommeyer G (2011) Microstructure and mechanical properties of nickel based superalloy IN718 produced by rapid prototyping with electron beam melting (EBM). Mater Sci Technol 27:876–883. https://doi.org/10.1179/026708309X12468927349451

[79] Yoon KB, Dao VH, Yu JM (2020) Effects of build direction on tensile and creep properties of 316L stainless steel produced by selective laser melting. Fatigue Fract Eng Mater Struct 43:2623–2636. https://doi.org/10.1111/ffe.13322

[80] Yu JM, Dao VH, Yoon KB (2020) Effects of scanning speed on creep behaviour of 316L stainless steel produced using selective laser melting. Fatigue Fract Eng Mater Struct 43:2312–2325. https://doi.org/10.1111/ffe.13298

[81] Bae JH, Yu JM, Dao VH, et al (2021) Effects of processing parameters on creep behavior of 316L stainless steel produced using selective laser melting. J Mech Sci Technol 35:3803–3812. https://doi.org/10.1007/s12206-021-2103-x

[82] Hermanová Š, Kuboň Z, Čížek P, et al (2022) Study of Material Properties and Creep Behavior of a Large Block of AISI 316L Steel Produced by SLM Technology. Metals (Basel) 12:. https://doi.org/10.3390/met12081283

[83] Dao VH, Yu JM, Yoon KB (2020) Anisotropic creep behavior of stainless steel produced by selective laser melting. Mater Sci Eng A 796:140040. https://doi.org/10.1016/j.msea.2020.140040

[84] Li M, Zhang X, Chen WY, Byun TS (2021) Creep behavior of 316 L stainless steel manufactured by laser powder bed fusion. J Nucl Mater 548:152847. https://doi.org/10.1016/j.jnucmat.2021.152847

[85] Li M, Chen W-Y, Zhang X (2022) Effect of heat treatment on creep behavior of 316 L stainless steel manufactured by laser powder bed fusion. J Nucl Mater 559:153469. https://doi.org/https://doi.org/10.1016/j.jnucmat.2021.153469

[86] Ávila Calderón LA, Rehmer B, Schriever S, et al (2022) Creep and creep damage behavior of stainless steel 316L manufactured by laser powder bed fusion. Mater Sci Eng A 830:142223. https://doi.org/10.1016/j.msea.2021.142223

[87] Yu JM, Dao VH, Yoon KB (2020) Investigation of creep behavior of 316L stainless steel produced by selective laser melting with various processing parameters. J Mech Sci Technol 34:3249–3259. https://doi.org/10.1007/s12206-020-0717-z

[88] Williams RJ, Al-Lami J, Hooper PA, et al (2021) Creep deformation and failure properties of 316 L stainless steel manufactured by laser powder bed fusion under multiaxial loading conditions. Addit Manuf 37:101706. https://doi.org/10.1016/j.addma.2020.101706

[89] Li Y, Krajňák T, Podaný P, et al (2023) Thermal stability of dislocation structure and its effect on creep property in austenitic 316L stainless steel manufactured by directed energy deposition. Mater Sci Eng A 873:144981. https://doi.org/10.1016/j.msea.2023.144981

[90] Li Y, Podaný P, Salvetr P, et al (2024) Building rate effect on microstructure and high temperature mechanical properties of Austenitic 316L stainless steel manufactured by laser directed energy deposition. Opt Laser Technol 172:110535. https://doi.org/https://doi.org/10.1016/j.optlastec.2023.110535

[91] Liu L, Ding Q, Zhong Y, et al (2018) Dislocation network in additive manufactured steel breaks strength–ductility trade-off. Mater Today 21:354–361. https://doi.org/10.1016/j.mattod.2017.11.004

[92] Shamsujjoha M, Agnew SR, Fitz-Gerald JM, et al (2018) High Strength and Ductility of Additively Manufactured 316L Stainless Steel Explained. Metall Mater Trans A Phys Metall Mater Sci 49:3011–3027. https://doi.org/10.1007/s11661-018-4607-2

[93] Voisin T, Forien J, Perron A, et al (2020) New insights on cellular structures strengthening mechanisms and thermal stability of an anstentic stainless steel fabricated by laser powder bed fusion. Acta Mater 203:116476. https://doi.org/10.1016/j.actamat.2020.11.018

[94] Prashanth KG, Eckert J (2017) Formation of metastable cellular microstructures in selective laser melted alloys. J Alloys Compd 707:27–34. https://doi.org/10.1016/j.jallcom.2016.12.209

[95] Kiran A, Hodek J, Vavřík J, et al (2020) Numerical simulation development and computational optimization for directed energy deposition additive manufacturing process. Materials (Basel) 13:. https://doi.org/10.3390/ma13112666

[96] Jia H, Sun H, Wang H, et al (2021) Scanning strategy in selective laser melting (SLM): a review. Int J Adv Manuf Technol 113:2413–2435. https://doi.org/10.1007/s00170-021-06810-3

[97] ASTM E8/E8M-21 (2021) Standard Test Methods for Tension Testing of Metallic Materials. ASTM Int West Consh: https://doi.org/https://www.astm.org/Standards/E8

[98] ASTM E21-20 (2020) Standard Test Methods for Elevated Temperature Tension Tests of Metallic Materials. ASTM Int West Consh: https://doi.org/https://www.astm.org/Standards/E21

[99] Zheng B, Haley JC, Yang N, et al (2019) On the evolution of microstructure and defect control in 316L SS components fabricated via directed energy deposition. Mater Sci Eng A 764:138243. https://doi.org/10.1016/j.msea.2019.138243

[100] Tan ZE, Pang JHL, Kaminski J, Pepin H (2019) Characterisation of porosity, density, and microstructure of directed energy deposited stainless steel AISI 316L. Addit Manuf 25:286–296. https://doi.org/10.1016/j.addma.2018.11.014

[101] Pacheco JT, Meura VH, Bloemer PRA, et al (2022) Laser directed energy deposition of AISI 316L stainless steel: The effect of build direction on mechanical properties in as-

built and heat-treated conditions. Adv Ind Manuf Eng 4:100079. https://doi.org/10.1016/j.aime.2022.100079

[102] Weng F, Gao S, Jiang J, et al (2019) A novel strategy to fabricate thin 316L stainless steel rods by continuous directed energy deposition in Z direction. Addit Manuf 27:474–481. https://doi.org/10.1016/j.addma.2019.03.024

[103] Aversa A, Marchese G, Bassini E (2021) Directed Energy Deposition of AISI 316L Stainless Steel Powder: Effect of Process Parameters. Metals (Basel) 11:932. https://doi.org/10.3390/met11060932

[104] Li SH, Zhao Y, Kumar P, Ramamurty U (2022) Effect of initial dislocation density on the plastic deformation response of 316L stainless steel manufactured by directed energy deposition. Mater Sci Eng A 851:143591. https://doi.org/10.1016/j.msea.2022.143591

[105] Feenstra DR, Cruz V, Gao X, et al (2020) Effect of build height on the properties of large format stainless steel 316L fabricated via directed energy deposition. Addit Manuf 34:101205. https://doi.org/10.1016/j.addma.2020.101205

[106] Zhang K, Wang S, Liu W, Shang X (2014) Characterization of stainless steel parts by Laser Metal Deposition Shaping. Mater Des 55:104–119. https://doi.org/10.1016/j.matdes.2013.09.006

[107] Kiran A, Koukolíková M, Vavřík J, et al (2021) Base plate preheating effect on microstructure of 316l stainless steel single track deposition by directed energy deposition. Materials (Basel) 14:5129. https://doi.org/10.3390/ma14185129

[108] Kumaran M, Senthilkumar V (2021) Experimental characterization of stainless steel 316L alloy fabricated with combined powder bed fusion and directed energy deposition. Weld World 65:1373–1388. https://doi.org/10.1007/s40194-021-01117-z

[109] Reitz W (2006) A Review of: “Welding Metallurgy and Weldability of Stainless Steel.” Mater. Manuf. Process. 21:219–219

[110] Aversa A, Saboori A, Librera E, et al (2020) The role of Directed Energy Deposition atmosphere mode on the microstructure and mechanical properties of 316L samples. Addit Manuf 34:101274. https://doi.org/10.1016/j.addma.2020.101274

[111] Saboori A, Aversa A, Bosio F, et al (2019) An investigation on the effect of powder

recycling on the microstructure and mechanical properties of AISI 316L produced by Directed Energy Deposition. Mater Sci Eng A 766:138360. https://doi.org/10.1016/j.msea.2019.138360

[112] Ma M, Wang Z, Zeng X (2017) A comparison on metallurgical behaviors of 316L stainless steel by selective laser melting and laser cladding deposition. Mater Sci Eng A 685:265–273. https://doi.org/10.1016/j.msea.2016.12.112

[113] Ziętala M, Durejko T, Polański M, et al (2016) The microstructure, mechanical properties and corrosion resistance of 316 L stainless steel fabricated using laser engineered net shaping. Mater Sci Eng A 677:1–10. https://doi.org/10.1016/j.msea.2016.09.028

[114] Yadollahi A, Shamsaei N, Thompson SM, Seely DW (2015) Effects of process time interval and heat treatment on the mechanical and microstructural properties of direct laser deposited 316L stainless steel. Mater Sci Eng A 644:171–183. https://doi.org/10.1016/j.msea.2015.07.056

[115] Tolosa I, Garciandía F, Zubiri F, et al (2010) Study of mechanical properties of AISI 316 stainless steel processed by “selective laser melting”, following different manufacturing strategies. Int J Adv Manuf Technol 51:639–647. https://doi.org/10.1007/s00170-010-2631-5

[116] Li M, Chen WY, Zhang X (2022) Effect of heat treatment on creep behavior of 316 L stainless steel manufactured by laser powder bed fusion. J Nucl Mater 559:153469. https://doi.org/10.1016/j.jnucmat.2021.153469

[117] Chae H, Huang EW, Woo W, et al (2021) Unravelling thermal history during additive manufacturing of martensitic stainless steel. J Alloys Compd 857:. https://doi.org/10.1016/j.jallcom.2020.157555

[118] Smith TR, Sugar JD, San Marchi C, Schoenung JM (2021) Microstructural development in DED stainless steels: applying welding models to elucidate the impact of processing and alloy composition. J Mater Sci 56:762–780. https://doi.org/10.1007/s10853-020-05232-y

[119] Mullins WW, Sekerka RF (1964) Stability of a planar interface during solidification of a dilute binary alloy. J Appl Phys 35:444–451. https://doi.org/10.1063/1.1713333

[120] Kou S (2003) Welding metallurgy. John Wiley & Sons, Hoboken, New Jersey, USA

[121] Yan F, Xiong W, Faierson E, Olson GB (2018) Characterization of nano-scale oxides in austenitic stainless steel processed by powder bed fusion. Scr Mater 155:104–108. https://doi.org/10.1016/j.scriptamat.2018.06.011

[122] Deng P, Yin H, Song M, et al (2020) On the Thermal Stability of Dislocation Cellular Structures in Additively Manufactured Austenitic Stainless Steels: Roles of Heavy Element Segregation and Stacking Fault Energy. Jom 72:4232–4243. https://doi.org/10.1007/s11837-020-04427-7

[123] Kiran A, Li Y, Hodek J, et al (2022) Heat Source Modeling and Residual Stress Analysis for Metal Directed Energy Deposition Additive Manufacturing. Materials (Basel) 15:2545. https://doi.org/10.3390/ma15072545

[124] Kiran A, Li Y, Koukolíková M, et al (2022) Elevated Temperature Baseplate Effect on Microstructure, Mechanical Properties, and Thermal Stress Evaluation by Numerical Simulation for Austenite Stainless Steel 316L Fabricated by Directed Energy Deposition. Materials (Basel) 15:4165. https://doi.org/10.3390/ma15124165

[125] Salman OO, Gammer C, Chaubey AK, et al (2019) Effect of heat treatment on microstructure and mechanical properties of 316L steel synthesized by selective laser melting. Mater Sci Eng A 748:205–212. https://doi.org/10.1016/j.msea.2019.01.110

[126] Segura IA, Murr LE, Terrazas CA, et al (2019) Grain boundary and microstructure engineering of Inconel 690 cladding on stainless-steel 316L using electron-beam powder bed fusion additive manufacturing. J Mater Sci Technol 35:351–367. https://doi.org/10.1016/j.jmst.2018.09.059

[127] Mower TM, Long MJ (2016) Mechanical behavior of additive manufactured, powder-bed laser-fused materials. Mater Sci Eng A 651:198–213. https://doi.org/10.1016/j.msea.2015.10.068

[128] Chen N, Ma G, Zhu W, et al (2019) Enhancement of an additive-manufactured austenitic stainless steel by post-manufacture heat-treatment. Mater Sci Eng A 759:65–69. https://doi.org/10.1016/j.msea.2019.04.111

[129] Kong D, Dong C, Ni X, et al (2019) Mechanical properties and corrosion behavior of

selective laser melted 316L stainless steel after different heat treatment processes. J Mater Sci Technol 35:1499–1507. https://doi.org/10.1016/j.jmst.2019.03.003

[130] Sistiaga MLM, Nardone S, Hautfenne C, van Humbeeck J (2016) Effect of heat treatment of 316L stainless steel produced by selective laser melting (SLM). In: Proceedings of the 27th Annual International Solid Freeform Fabrication Symposium-An Additive Manufacturing Conference- Solid freeform fabrication. pp 558–565

[131] Bertsch KM, Meric de Bellefon G, Kuehl B, Thoma DJ (2020) Origin of dislocation structures in an additively manufactured austenitic stainless steel 316L. Acta Mater 199:19–33. https://doi.org/10.1016/j.actamat.2020.07.063

[132] Hansen N, Mehl RF (2001) New discoveries in deformed metals. Metall Mater Trans A Phys Metall Mater Sci 32:2917–2935. https://doi.org/10.1007/s11661-001-0167-x

[133] Kuhlmann-Wilsdorf D, Van Der Merwe JH (1982) Theory of dislocation cell sizes in deformed metals. Mater Sci Eng 55:79–83. https://doi.org/10.1016/0025-5416(82)90086-6

[134] Kuhlmann-Wilsdorf D (1989) Theory of plastic deformation: - properties of low energy dislocation structures. Mater Sci Eng A 113:1–41. https://doi.org/10.1016/0921-5093(89)90290-6

[135] SAE International (2016) Nickel Alloy, Corrosion and Heat-Resistant, Bars, Forgings, and Rings 52.5Ni - 19Cr - 3.0Mo - 5.1Cb (Nb) - 0.90Ti - 0.50AI - 18Fe Consumable Electrode or Vacuum Induction Melted 1775 °F (968 °C) Solution Heat Treated, Precipitation-Hardenable

[136] SAE International (2018) Nickel Alloy, Corrosion and Heat-Resistant, Investment Castings 52.5Ni - 19Cr - 3.0Mo - 5.1Cb(Nb) - 0.90Ti - 0.60Al - 18Fe Vacuum Melted Homogenization and Solution Heat Treated. https://doi.org/https://www.sae.org/standards/content/ams5383/

[137] Raghavan S, Zhang B, Wang P, et al (2017) Effect of different heat treatments on the microstructure and mechanical properties in selective laser melted INCONEL 718 alloy. Mater Manuf Process 32:1588–1595. https://doi.org/10.1080/10426914.2016.1257805

[138] Zhang D, Niu W, Cao X, Liu Z (2015) Effect of standard heat treatment on the

microstructure and mechanical properties of selective laser melting manufactured Inconel 718 superalloy. Mater Sci Eng A 644:32–40. https://doi.org/10.1016/j.msea.2015.06.021

[139] Tucho WM, Cuvillier P, Sjolyst-Kverneland A, Hansen V (2017) Microstructure and hardness studies of Inconel 718 manufactured by selective laser melting before and after solution heat treatment. Mater Sci Eng A 689:220–232. https://doi.org/10.1016/j.msea.2017.02.062

[140] Knorovsky GA, Cieslak MJ, Headley TJ, et al (1989) INCONEL 718: A solidification diagram. Metall Trans A 20:2149–2158. https://doi.org/10.1007/BF02650300

[141] Yu X, Lin X, Liu F, et al (2020) Influence of post-heat-treatment on the microstructure and fracture toughness properties of Inconel 718 fabricated with laser directed energy deposition additive manufacturing. Mater Sci Eng A 798:140092. https://doi.org/10.1016/j.msea.2020.140092

[142] Gallmeyer TG, Moorthy S, Kappes BB, et al (2020) Knowledge of process-structure-property relationships to engineer better heat treatments for laser powder bed fusion additive manufactured Inconel 718. Addit Manuf 31:100977. https://doi.org/10.1016/j.addma.2019.100977

[143] Tucho WM, Hansen V (2019) Characterization of SLM-fabricated Inconel 718 after solid solution and precipitation hardening heat treatments. J Mater Sci 54:823–839. https://doi.org/10.1007/s10853-018-2851-x

[144] Dubiel B, Kruk A, Stepniowska E, et al (2009) TEM, HRTEM, electron holography and electron tomography studies of γ′ and γ″ nanoparticles in Inconel 718 superalloy. J. Microsc. 236:149–157

[145] Paulonis, D F; Oblak, J M; Duvall DS (1969) Precipitation in nickel-base alloy 718. Trans Amer Soc Met 62:611–622

[146] Zhao X, Chen J, Lin X, Huang W (2008) Study on microstructure and mechanical properties of laser rapid forming Inconel 718. Mater Sci Eng A 478:119–124. https://doi.org/https://doi.org/10.1016/j.msea.2007.05.079

[147] Han Y, Chaturvedi MC (1987) Steady state creep deformation of superalloy inconel 718.

Mater Sci Eng 89:25–33. https://doi.org/10.1016/0025-5416(87)90246-1

[148] Chaturvedi MC, Han Y (1989) Creep Deformation of Alloy 718. Miner Met Mater Soc 489–498. https://doi.org/10.7449/1989/superalloys_1989_489_498

[149] Brooks JW, Bridges PJ (2012) Metallurgical Stability of Inconel Alloy 718. 33–42. https://doi.org/10.7449/1988/superalloys_1988_33_42

[150] Cocks ACF (1985) The nucleation and growth of voids in a material containing a distribution of grain-boundary particles. Acta Metall 33:129–137. https://doi.org/10.1016/0001-6160(85)90226-3

[151] Chen, Weixing, Chaturvedi MC (1997) Depedndence of creep fracture of inconel 718 on grain boundary precipitates. Acta Mater 45:2735–2746. https://doi.org/10.1016/S1359-6454(96)00399-0

[152] Liu L, Ding Q, Zhong Y, et al (2018) Dislocation network in additive manufactured steel breaks strength–ductility trade-off. Mater Today 21:354–361. https://doi.org/10.1016/j.mattod.2017.11.004

[153] Yoo YSJ, Book TA, Sangid MD, Kacher J (2018) Identifying strain localization and dislocation processes in fatigued Inconel 718 manufactured from selective laser melting. Mater Sci Eng A 724:444–451. https://doi.org/10.1016/j.msea.2018.03.127

[154] Ni M, Chen C, Wang X, et al (2017) Anisotropic tensile behavior of in situ precipitation strengthened Inconel 718 fabricated by additive manufacturing. Mater Sci Eng A 701:. https://doi.org/10.1016/j.msea.2017.06.098

[155] Aydinöz ME, Brenne F, Schaper M, et al (2016) On the microstructural and mechanical properties of post-treated additively manufactured Inconel 718 superalloy under quasi-static and cyclic loading. Mater Sci Eng A 669:246–258. https://doi.org/10.1016/j.msea.2016.05.089

[156] Zheng B, Haley JC, Yang N, et al (2019) On the evolution of microstructure and defect control in 316L SS components fabricated via directed energy deposition. Mater Sci Eng A 764:138243. https://doi.org/10.1016/j.msea.2019.138243

[157] Ziętala M, Durejko T, Polański M, et al (2016) The microstructure, mechanical properties and corrosion resistance of 316L stainless steel fabricated using laser

engineered net shaping. Mater Sci Eng A 677:1–10. https://doi.org/https://doi.org/10.1016/j.msea.2016.09.028

[158] Gäumann M, Bezençon C, Canalis P, Kurz W (2001) Single-crystal laser deposition of superalloys: Processing-microstructure maps. Acta Mater 49:1051–1062. https://doi.org/10.1016/S1359-6454(00)00367-0

[159] Xiong L, Wang C, Wang Z, Jiang P (2020) The interaction between grains during columnar-to-equiaxed transition in laser welding: A phase-field study. Metals (Basel) 10:1–21. https://doi.org/10.3390/met10121647

[160] Rzepa S, Matous U, Daniel M, et al (2023) Mechanical behavior of 316L-IN718 interface produced by directed energy deposition investiagted using miniaturized specimens. In: Proceedings of the ASME 2023 Pressure Vessels & Piping Conference. pp 1–9

[161] Zhang J, Liu Y, Bayat M, et al (2021) Achieving high ductility in a selectively laser melted commercial pure-titanium via in-situ grain refinement. Scr Mater 191:155–160. https://doi.org/10.1016/j.scriptamat.2020.09.023

[162] Todaro CJ, Easton MA, Qiu D, et al (2020) Grain structure control during metal 3D printing by high-intensity ultrasound. Nat Commun 11:1–10. https://doi.org/10.1038/s41467-019-13874-z

[163] Zou X, Yan Z, Zou K, et al (2022) Grain refinement by dynamic recrystallization during laser direct energy deposition of 316L stainless steel under thermal cycles. J Manuf Process 76:646–655. https://doi.org/10.1016/j.jmapro.2022.01.057

12 List of publications and presentations

Publications

[1] **Y. Li**, J. Džugan, M. Brázda. High temperature fracture behaviour of 316L stainless steel-Inconel 718 functionally graded materials manufactured by directed energy deposition: role of interface orientation and heat treatment. ***Mater. Sci. Eng. A***. 2024. **(Q1, IF 6.4)**

[2] **Y. Li**, P. Podaný, J. Džugan, M. Brázda. Building rate effect on microstructure and high temperature mechanical properties of Austenitic 316L stainless steel manufactured by laser directed energy deposition. ***Opt. Laser Technol***. 2024, 172:110535. **(Q1, IF 5)**

[3] **Y. Li**, T. Krajňák, P. Podaný, J. Veselý, J. Džugan. Thermal stability of dislocation structure and its effect on creep property in Austenitic 316L stainless steel manufactured by directed energy deposition. ***Mater. Sci. Eng. A***. 2023, 873: 144981. **(Q1, IF 6.4)**

[4] M. Rott, **Y. Li**, J. Džugan. In-situ directed energy deposition of Al based low density steel for automotive applications. ***Sci. Rep.*** 2023, 13:21911. **(Co-first author, Q1, IF 4.6)**

[5] **Y. Li**, P. Podaný, M. Koukolíková, J. Džugan, T. Krajňák, J. Veselý, S. Raghavan, Effect of Heat Treatment on Creep Deformation and Fracture Properties for a Coarse-Grained Inconel 718 Manufactured by Directed Energy Deposition, ***Materials*** (Basel). 2023, 16:1–12. **(Q2, IF 3.4)**

[6] D. Melzer, M. Koukolíkova, S.Rzepa, **Y. Li**, J. Dzugan, M. Brazda. Influence of interface orientation and surface quality on structural and mechanical properties of SS316L/IN718 block produced using directed energy deposition. ***Surf. Interfaces***. 2023, 41: 103139. **(Q1, IF 6.2)**

[7] **Y. Li**, J. Dlouhý, J. Vavřík, J. Džugan, P. Konopík, T. Krajňák, J. Veselý, Investigation of short-term creep properties of a coarse-grained Inconel 718 fabricated by directed energy deposition compared to traditional Inconel 718, ***Mater. Sci. Eng. A***. 2022, 844:143143. **(Q1, IF 6.4)**

[8] **Y. Li**, J. Dlouhý, M. Koukolíková, A. Kirana, J. Vavřík, J. Džugan, Effect of deposit thickness on microstructure and mechanical properties at ambient and elevated temperatures for Inconel 718 superalloy fabricated by directed energy deposition, ***J. Alloys Compd***. 2022, 908:164723. **(Q1, IF 6.2)**

[9] A. Kiran, **Y. Li**, J. Hodek, M. Brázda, M. Urbánek, J. Džugan, Heat Source Modeling and Residual Stress Analysis for Metal Directed Energy Deposition Additive Manufacturing, ***Materials*** (Basel). 2022, 15:2545. **(Q2, IF 3.4)**

[10] A. Kiran, **Y. Li**, M. Koukolíková, M. Brázda, J. Hodek, M. Urbánek, J. Džugan, S. Raghavan, J. Odehnal, Elevated Temperature Baseplate Effect on Microstructure, Mechanical Properties, and Thermal Stress Evaluation by Numerical Simulation for Austenite Stainless Steel 316L Fabricated by Directed Energy Deposition, ***Materials*** (Basel). 2022, 15:4165. **(Q2, IF 3.4)**

[11] J. Džugan, E. Lucon, M. Koukolíková, **Y. Li**, S. Rzepa, M. S. Yasin, S. Shao, N. Shamsaei, M. Seifi, M. Lodeiro, F. Lefebvre, U.Mayer, J. Olbricht, M. Houska, V. Mentl and Z. You, Theor Appl Fract Mec, 2024. (Q1, IF 5.3, in revision)

Presentations at conferences

[1] FEMS EUROMAT 2023, the 17th European congress and exhibition on advanced materials and processes, September 03-07, 2023, in Frankfurt am Main, Germany. Presentation with the title of thermal stability of dislocation structure and its effect on creep property in Austenitic 316L stainless steel manufactured by directed energy deposition.

[2] COMAT 2022, the 7th international conference-modern trends in construction materials, September 06-08, 2022, in Pilsen, Czech Republic. Presentation with the title of deposition thickness-related creep behavior for IN718 fabricated by directed energy deposition.

13 List of figures

14 List of tables